博士論文

Nanostructure Formation on Crystalline Si Surface Using Ag-Assisted Solution Process and their Applications in Solar Cells

「Ag を用いた溶液プロセスによる結晶シリコン表面へのナノ構造形成と太陽電池への応用」

李　雨晴

281832273

名古屋大学工学研究科マテリアル理工学専攻材料工学分野

物質創成工学講座　宇佐美・黒川・伊藤研究室

令和 5 年 12 月

Abstract

In recent years, nano-sized silicon light confinement structures have attracted much attention for their application in crystalline silicon solar cells due to their excellent light absorption as well as small surface area and small etching margin. The mainstream means of fabricating Si nanotextures usually require the use of vacuum conditions, expensive equipment and complex operation, which are not conducive to cost reduction and large-scale industrial production. This dissertation aims to develop an original Ag-assisted wet etching method to fabricate nano-sized Si textures and to investigate the effect of Si nanotextures with different sizes and morphologies on the efficiency of c-Si solar cells.

Firstly， we propose an original method to fabricate nanometer-sized pyramids (nanopyramids) featuring an average size of ~500 nm or even smaller by using a simple one-step Ag-assisted solution process. The texture size can be controlled by the concentration of $AgNO_3$ in the alkaline etching solution where the generated Ag nanoparticles act as an etching mask as well as promoting the detachment of H_2 bubbles from the reacting Si surface. This process enables the formation of uniformly distributed Si nanopyramids with a lower reflectance below 10% and a smaller etching margin less than 1.7 μm compared with the conventional micropyramids. Si heterojunction solar cells employing Si nanopyramids outperform those with the conventional micropyramids owing to the reduced optical reflectance while preserving excellent surface passivation and carrier transport properties. These results demonstrate the advantages of our method and the high potential of Si nanopyramids for various applications such as thin crystalline Si solar cells and perovskite/Si tandem solar cells.

Next，Si nanopyramids are applied as the double-sided textures in the Si bottom cell to be compatible with the solution-processed perovskite top cell in perovskite/Si tandem solar cells. Herein, an Ag-assisted alkaline etching method is applied to fabricate nanoscale Si pyramid textures and the influence of varying pyramid size (400-900 nm)

on the interface morphology and the performance of perovskite/Si tandem cells is investigated. It is demonstrated that electrical shunting starts to increase, and the open-circuit voltage (V_{OC}) decreases as the texture size increases above 600 nm due to the non-uniform top-cell formation on a rough Si surface. However, when the texture size is reduced to 400-500 nm, all spin-coated perovskite top-cell component layers exhibit an even form over the nanopyramid Si, resulting in a high V_{OC} and an enhanced Si bottom cell current (~1.0 mA cm^{-2}) due to the suppressed reflectance at the top/bottom cell interface without using optical couplers. The both-sided nanopyramid Si texture offers opportunities to increase tandem cell efficiency while reducing its production cost compared with the commonly used single-sided textured Si.

Finally, the Si nanotip structures were fabricated by improving on the metal-assisted chemical etching(MACE) method. The main parameters during the fabricating process of Si nanowires are figured out, and Si nanowires with different lengths and diameters are successfully fabricated. The effect of microporous Si formation on the morphology of nanowires is discovered, and Si nanotips are fabricated on this basis. Si nanotips with different morphology are fabricated by combing high H_2O_2 concentration etching and polishing treatment. The etching mechanism was explained on the basis of detailed pilot studies, and the control of the size and distribution of the Si nanotips was realized. Further, a thin PEDOT: PSS layer was coated on to Si nanowire structures by spin coating. It is demonstrated that silicon nanotip textures are more favorable for conformal film formation of organic materials compared to conventional silicon nanowires.

Table of Contents

1 Introduction

1.1 Background

1.1.1 Decarbonized society and solar energy

In recent years, with the rapid population growth and remarkable economic development, energy supply is needed to keep pace with this increase in energy demand. However, thermal power generation, which has supported industrial development for a long time, has problems of greenhouse gas emissions and resource depletion, and the concerns over unstable situation in resource-producing countries. Today, when global environmental problems are being taken seriously, the development of a low-carbon economy and the move towards a low-carbon society have gradually become a consensus. It refers to a form of economic development that, under the guidance of the concept of sustainable development, reduces the consumption of high-carbon energy sources such as coal and oil, reduces greenhouse gas emissions, and achieves a win-win situation for economic and social development and ecological and environmental protection through a variety of means such as the development of new energy sources. The global electricity generation be source from 2022 to 2025 in Figure 1.1 reveals that renewables would increase their share of global electricity generation from 29% to 35%[1], and become the world`s largest electricity source within just three years. Clean energy like nuclear power is being used around the world as a replacement for fossil fuels, while the safety problems of nuclear energy have been widely debated, such as explosions caused by natural disasters or human error and radioactive material pollution. The strict government regulations on carbon emission and limited availability of fossil fuels create a strong need for cost-effective and efficient sources such as solar energy. Figure 1.2 shows the world's non-fossil energy supply by source analysis and forecast from 1990 to 2050.[2] This shows that the solar photovoltaic power generation market has great growth prospects, and the development of cheaper and more efficient solar cells has become an urgent task.

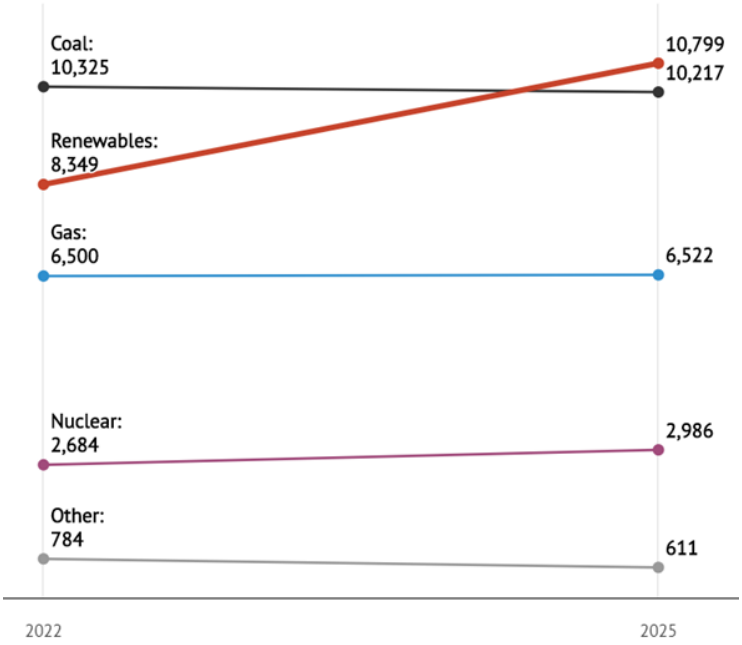

Figure 1.1. Global electricity generation by source,2022-2025,TWh.

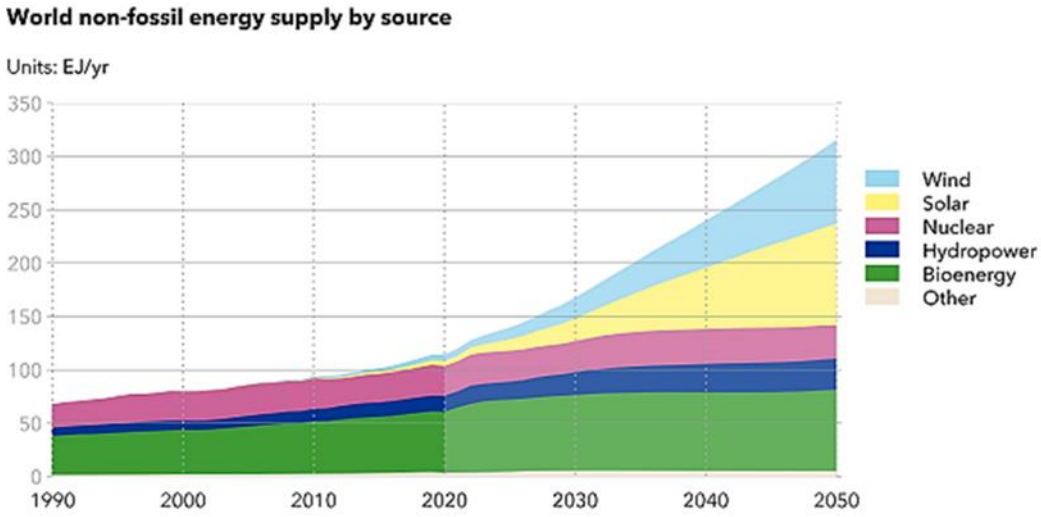

Figure 1.2. The world's non-fossil energy supply by source analysis and forecast from 1990 to 2050.

1.1.2 Crystalline Si solar cells with thin substrates

Currently, solar cells are mainly of the silicon (Si) due to the abundance of Si, long-term reliability, relatively high power conversion efficiency (PCE) and the continuous

reduction in the production cost , and crystalline Si photovoltaic (PV) technology accounts for about 95% of the worldwide PV market (Figure 1.3).[3] The rest 5% relies upon the thin film photovoltaic cells. Thus, Si-PV is expected to provide an economical and sustainable solution as a major renewable energy resource towards a decarbonized society.

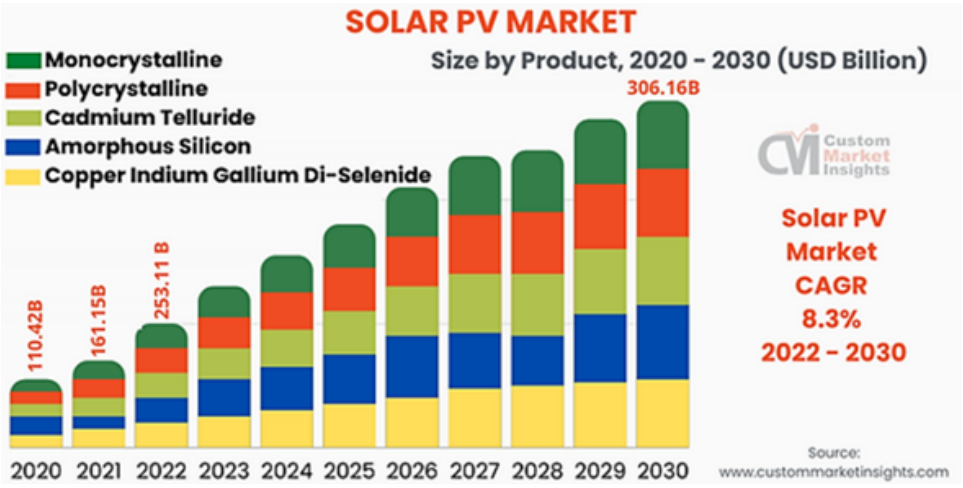

Figure 1.3. Global Solar PV (Photovoltaic) Market Size/Share Worth 306.16 Billion by 2030 at an 8.3% CAGR.

As shown in Figure 1.4, PV system capital cost from 1995 to 2020, the average cost of solar panels has dropped from $44,000 down to $15,200 over the past decade, which indicates that reducing the manufacturing cost of solar cells is market demand of great concern now. Since Si wafer contributes an average of 14% to total module production costs in the photovoltaic market, the development of thin crystalline silicon (c-Si) solar cell (<120 µm) is a promising way to significantly cut down the production cost of the cell modules.[4] Nowadays, there is a development trend of thin Si substrates as the term of cost reduction and its potential application in flexible devices. We can see from the trend for minimum as-cut n-type wafer thickness in mass production of solar cells in Figure 1.5 that year by year, the thickness of Si wafer for solar cell fabrication is decreasing until 120 µm.[5] At the moment, the solar cell with the conversion efficiency of 24.75% was successfully fabricated with Si substrate of only 98um think.[6] Besides,

Ultra-thin c-Si has attracted widespread attention due to its excellent mechanical flexibility. The added flexibility opens up new markets for solar cells, as they can be applied in a variety of mobile and flexible devices. One example is lightweight, high-efficiency (35%), flexible multi-junction solar cells when ultra-thin Si is used as the bottom cell and combined with wide bandgap semiconductor materials. Flexible multi-junction solar cells are ideal candidates for new applications in mobile vehicles and are expected to be widely used as clean energy.

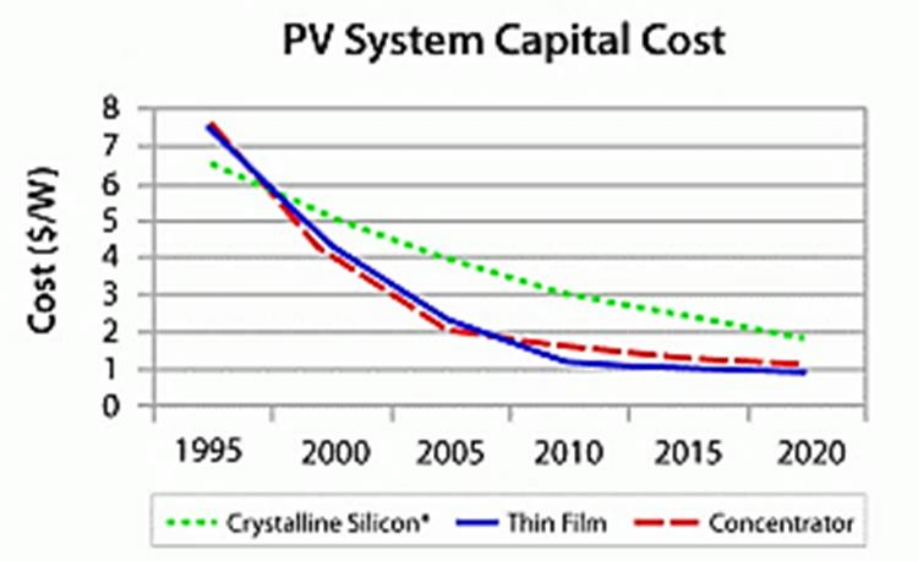

Figure 1.4 PV system capital cost from 1995 to 2020.

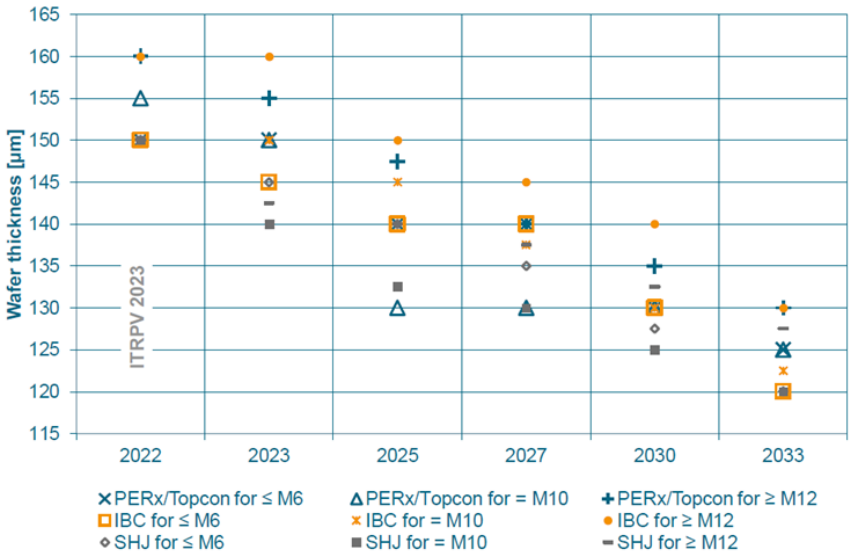

Figure 1.5. The trend for minimum as-cut n-type wafer thickness in mass production of solar cells.

1.1.3 Anti-reflection design in Si solar cells

We can see from the absorption coefficient diagram in Figure 1.6, that Si material is an indirect energy band material. In the visible light range, the light absorption coefficient of Si is much lower than that of other solar photoelectric materials. when preparing crystalline Si solar cells, the thickness of the Si wafer must be above 150-200 µm in order to effectively absorb solar energy, which is contrary to the need to reduce the thickness of the Si wafers. From the diagram of the relationship between Si substrate thickness and external quantum efficiency in Figure 1.7, when the wafer thickness is above 150nm the external quantum efficiency is the same regardless of the Si substrate thickness at wavelengths below 500 nm, while the external quantum efficiency decreases at wavelengths above 900 nm as the Si substrate thickness becomes thinner.[7] Therefore, it is necessary to introduce light confinement structures (LTSs) with small etching margins that do not reduce the light absorption rate even on thin Si substrates.

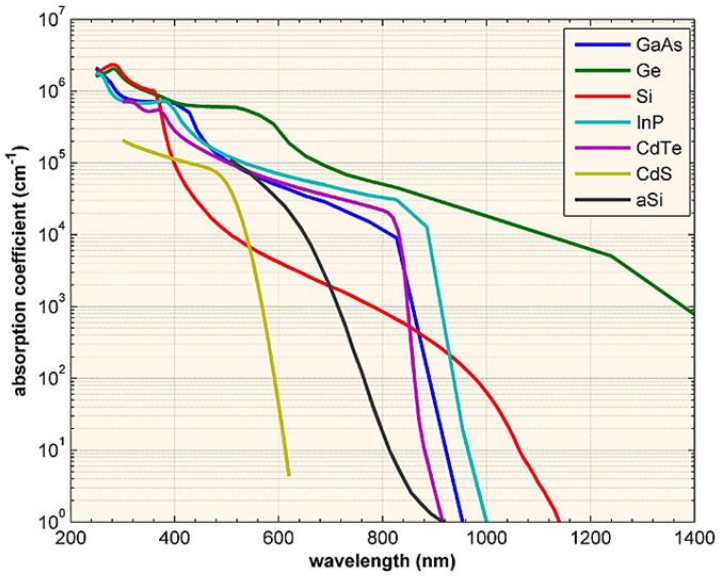

Figure 1.6. The absorption coefficient in a variety of semiconductor materials at 300K as a function of wavelength of light.

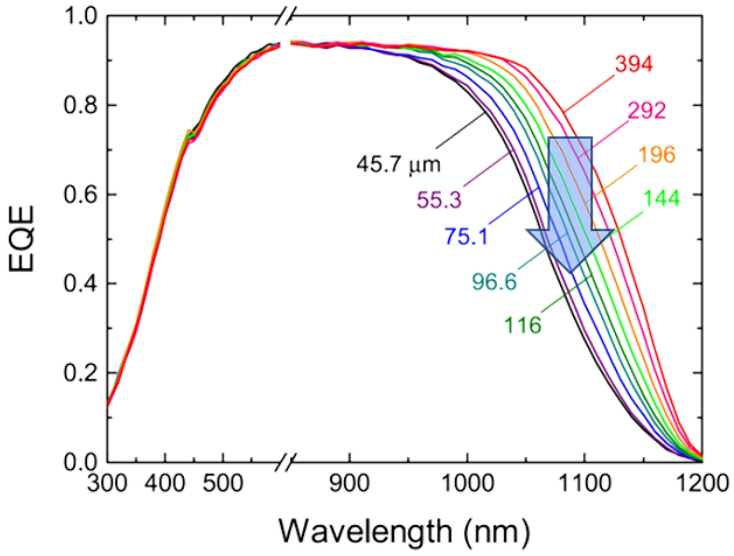

Figure 1.7. Relationship between Si substrate thickness and external quantum efficiency

As we know, the principle of c-Si solar cell power generation is mainly the photoelectric effect of semiconductors. When the Si substrate is subjected to light, the photogenerated holes in the N-type semiconductor in the PN junction move towards

the P-type region, while the photogenerated electrons in the P-type region move towards the N-type region, forming a current from the N-type region to the P-type region. Therefore, the amount of incident light absorption directly affects the number of photogenerated carriers in the solar cell. Therefore, it is important to design various anti-reflective structures for solar cells to reduce reflection and refraction and enhance the absorption of incident light. Figure 1.8 shows a schematic diagram of the basic structure of a Si heterojunction solar cell. The anti-reflection design for solar cell is mainly composed of three parts. Anti-reflection(AR) coatings with suitable thicknesses have been widely used to reduce reflectance and increase transmittance on top of solar cells. Different refractive indices of AR coatings lead to discordance between the different layers, resulting in a reduction of reflectance[8] (Figure 1.9).

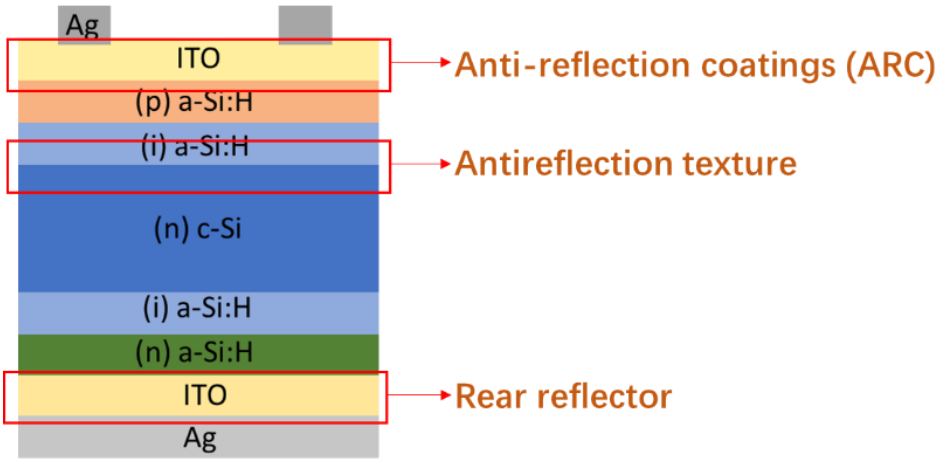

Figure 1.8. Schematic diagram of structure of Si heterojunction solar cell

Transparent conducting oxides (TCOs) like ITO, SiNx metamaterials, nanocomposite and sol-gel materials are used for AR coatings[9], they usually have unique combination of excellent electronic and optical properties, but suffering from narrow wavelength range for light absorption and high absorption in the UV region reducing the short-circuit current of the cell.[2] The second one is the light confinement structures on the front side of the Si substrate, to reduce reflection and increasing the optical range length of light is achieved by introducing micron-sized or nano-sized periodic structures on the Si

surface. There are various types of light confinement structures, such as pyramid/Inverted pyramid structures, nanowire structures, micropores and photonic nanostructures, depending on the size and shape of the irregularities. [10] Fabricated by wet/dry etching methods; The third is the rear reflection on the bottom of the cell. Rear reflectors can enhance the light path length of weakly absorbed near infrared light in Si solar cells by reflecting transmitted light in long wavelength back into the Si substrate for secondary absorption. It can be realized by textured metal contact[11], AR coatings, and diffuse reflector with high refractive index containing light confinement textures, Ag/TiO_2 nanoparticles and white paint.[12,13] Among these anti-reflective designs, the LTSs of the Si substrate are easy to realize and effectively reduces the reflection of incident light on Si surface, efficiently increasing the conversion efficiency of the c-Si solar cell, thus it has been widely used and plays a very important role in enhancing light absorption.

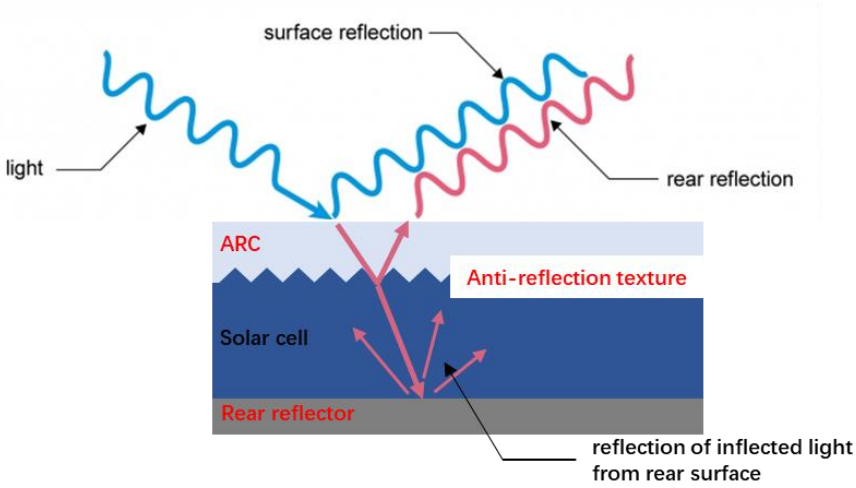

Figure 1.9. The anti-reflection design for Si solar cells

1.1.4 Conventional Si texture fabrication method

Currently, the thinnest Si substrate is reported to be 30 μm.[14] The drawback of this thinner substrate is that conversion efficiency decreases due to decreased amount of light absorbed by the substrate because of the shorten optical path length. Therefore, it

is necessary to increase the amount of light absorption by fabricating light confinement structure on the substrate surface of the thin c-Si solar cell. Si pyramid structure is widely used in thin c-Si solar cells with broad acceptability in industrial fabrication for it effectively reduces the refraction of incident light with only a small increase in surface area. Another light trapping structure Si nanowire (SiNW) are widely used to combine with new solar cell materials functionally to achieve both low cost by reducing the amount of Si material be used and high efficiency due to the advantages of nanostructures: large PN junction area, extremely low light reflectance and can fusion with dissimilar materials. Figure 1.10 (a) and (b) shows the SEM images of Si pyramid structure and Si nanowire structure respectively.

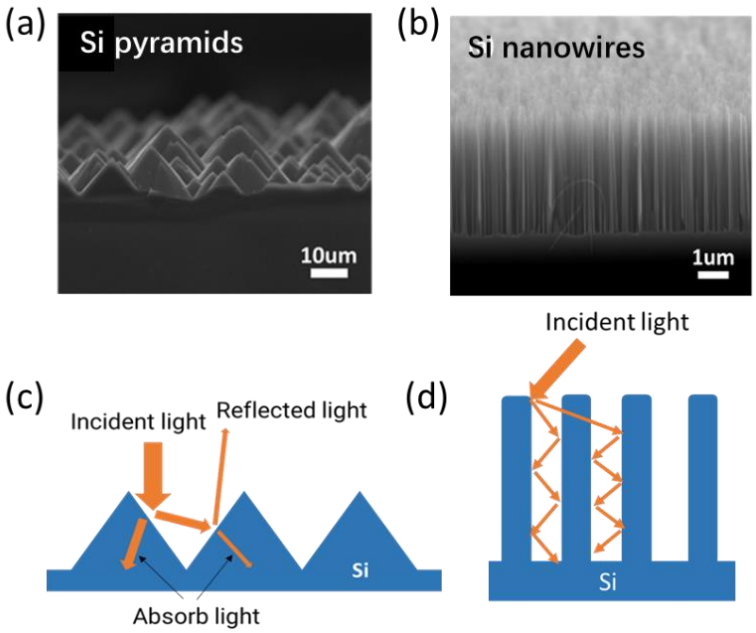

Figure 1.10. (a) Cross-sectional SEM images of Si pyramid structure; (b) Cross-sectional SEM images of Si nanowire structure; (c) Light trapping principle of Si pyramid texture; (d) Light trapping principle of Si nanowire texture

These two structures can effectively reduce the reflection of incident light by reduced reflection due to multiple reflections and reduced transmission due to increased optical path length (Figure 1.10 (c)(d)). Conventional wet etching methods are as follows:

(i) Anisotropic alkaline etching

The commonly used method of fabricating pyramid textures on Si surfaces, in industrial production is anisotropic alkaline etching method, the mechanism in shown in Figure 1.11 (a). Conventional alkaline solution consisting of KOH(or NaOH) and surfactant, the texture formation is relevant to the nucleation and growth of pyramids.[15] At temperature lower than 75 °C, the phenomena such as absorption of unreactive and massive ions and particles (K^+, IPA) on the surfaces limits the access of OH^- (hydroxide ions)to Si substrate, which directs to the dominant formation of nuclei.[16] At high temperature of 80 °C, the pyramidal textures are formed together with the flocculent precipitation on the surface following the possible reactions [17]:

$$Si + 2OH^- + H_2O \rightarrow SiO_2(OH)_2{}^{2-} + 2H_2 \uparrow \qquad (1.1)$$

Generated hydrogen bubbles directly adhere to Si surface and works as a barrier to suppress chemical reaction.[18] The poor bubble detachment leads to insufficient pyramid nucleation and results in poor texture uniformity and micro scale texture size. And the etching processes took 20min for dense of textures on Si surface with large etching margin of dozens of micrometers. Therefore, using alkaline solution requires the precise control of high temperatures as well as additional techniques to control the uniform distribution of pyramidal textures.

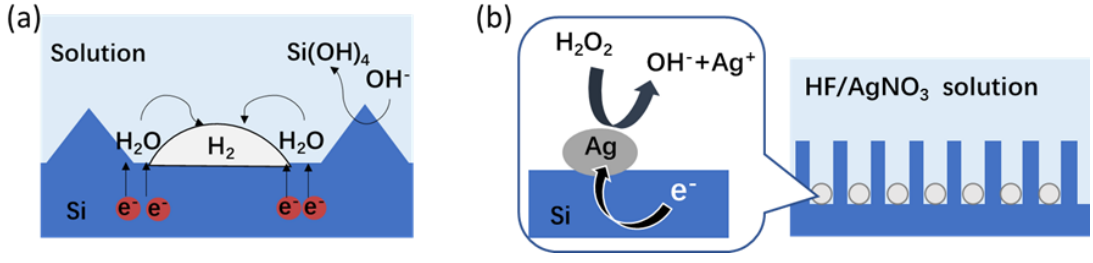

Figure 1.11. (a) Schematic diagrams of the etching mechanism of anistropic alikaline etching; (b) Schematic diagrams of the etching mechanism of metal-assited chemical etching.

(ii) Metal-assisted electroless etching

Metal-assisted chemical etching (MACE) method, reported by Li and Bohn, is a surprisingly simple and facile wet chemical process that produced high aspect ratio silicon nanowires(SiNWs) using transition metal catalysts like Ag. [19, 20]

Figure 1.11 (b) shows the fabrication mechanism of SiNWs by metal assisted electroless etching process. There are two steps for MACE method. First is electroless Ag plating. Si is immersed in mixed solution of HF/$AgNO_3$, the reaction occurs is showed in formula (1.2). The silver ions (Ag^+) near the Si surface absorb electrons in the Si and form nano-sized Ag nuclei which are deposited on the Si surface. Due to the higher electronegativity, the Ag nuclei deposited on the Si surface has a strong attraction for electrons from Si and becomes negatively charged.[21] Since Ag nuclei have strong catalytic activity, Ag^+ in the solution undergoes a cathodic reaction on the surface of these Ag nuclei and be reduced. Therefore, Ag+ is more likely to obtain electrons from Ag nuclei and deposit around them than on the bare Si surface, resulting in formation and growing of Ag particles on the surface of Si substrate.

$$Si + 6F^- \rightarrow SiF_6^{2-} + 4e^-$$

$$Ag^+ + e^- \rightarrow Ag$$

$$Si + 6F^- + 4Ag^+ \rightarrow SiF_6^{2-} + 4Ag \qquad (1.2)$$

Second step is etching. Si wafer with Ag particles is immersed in mixed solution of HF/H_2O_2, H_2O_2 as the oxidant, reacts directly with Ag nanoparticles forming Ag^+ locally around the nanoparticles as formula (1.3) showes, at the same time Ag particles extract electrons from Si, so that Si is oxidized to a tetravalent compound and dissolved in the solution.

$$2Ag + H_2O_2 + 2H^+ \rightarrow 2Ag^+ + 2H_2O$$

$$Si + 4Ag^+ + 6F^- \rightarrow 4Ag + SiF_6$$

$$Si + 2H_2O_2 + 4H^+ + 6F^- \rightarrow SiF_6^{2-} + 4H_2O \quad (1.3)$$

Therefore, the part of the Si surface that is in contact with the Ag particles will be continuously dissolved, resulting in Ag particles sink down into the Si bulk and the unetched part form nanowire structures. The MACE method does not require high temperature and vacuum conditions, and the full solution method, which can be carried out at room temperature, is a simple and economical preparation method. The Si nanowires obtained from the preparation have a single orientation and a controllable cross-sectional shape, which have been widely used in recent years.

1.1.5 Si nanostructures and application in crystalline Si solar cells

In recent years, nano-sized Si light confinement structures have attracted increasing attention. This is due to the fact that nano-sized Si textures have a smaller specific surface area and less etching margin than conventional micron-sized Si textures as well as good light absorption properties, making them ideal for applications to thin c-Si solar cells and organic/Si hybrid solar cells to further improve the conversion efficiency. For example, nano-sized Si pyramid(Si nanopyramid) textures for thin c-Si solar cells[22, 23, 24], SiNWs for hybrid heterojunction solar cells[25,26], shown in Figure1.12 (a) and (b). For Si nanopyramid textures, it reduces the consumption of Si substrates during process, making it ideal for use in ultra-thin Si photovoltaics and various light-weight and flexible c-Si devices.[27,28] In the meanwhile, it offers the potential of conformal layer formation of organic material by means of low-cost solution-based deposition techniques on top of Si nanopyramids. For example, by employing Si nanopyramid texture, ultra-thin Si as a bottom cell combined with wide-gap materials such as metal halide perovskite or group III-V compound semiconductor, high efficiency (35%) tandem solar cell can be realized.[29] On the other hand, Si nanowires not only exhibit an excellent light absorption capability by light antireflective and scattering effects, but also offers the

radial p–n junction architectures which provide a large junction area for charge separation. Recently, hybrid solar cell of SiNWs/organic with power conversion efficiency (PCE) of 16.1% has been achieved.[30] The interface engineering of solar cell by nanostructures are achieved mainly through three areas: enhanced light absorption; optimization of surface morphology; and modified interface properties. However, till now, the power conversion efficiency of these new generation c-Si solar cells is far from satisfactory for commercial applications. In order to put these cost -effective solar cells into practical use, further structural optimization is necessary to improve their performance.

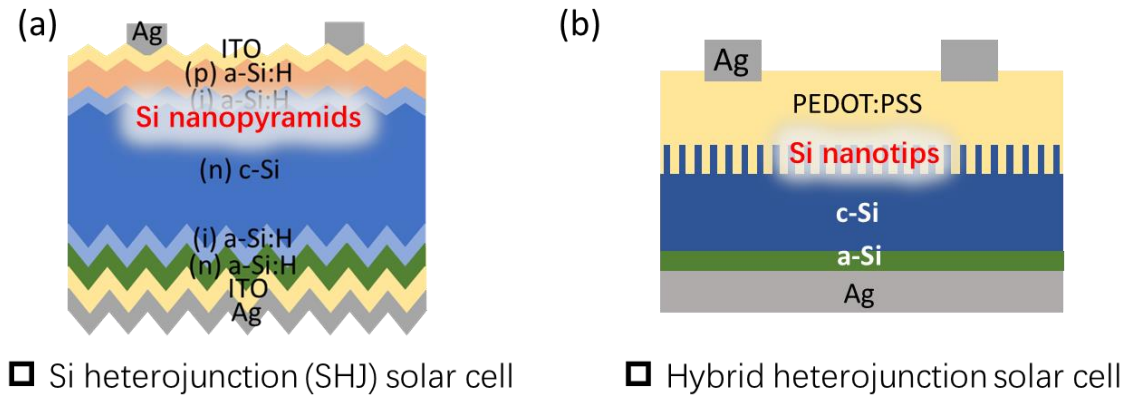

Figure 1.12. (a) Schematic diagram of Si heterojunction solar cell structure employing Si nanoptramids structure; (b) Schematic diagram of Organic/Si hybrid solar cell structure employing Si nanowire structure

Due to these demands, various sub-micron as well as nano-sized Si textured structures have been developed. The mainstream for fabricating nano textures is a two-step etching method, which is first pre-masking with metal particles like Germanium dots, Ag particles, or by polymer materials formed by lithography processes such as laser-interference lithography and nano-imprint lithography[31, 32] then come up with wet/dry etching process. Glass microbeads are also employed by mixing in etching solution to destruct hydrogen(H_2) bubbles generated during the etching process. And

the mainstream methods for fabricating SiNWs are laser ablation, chemical vapor deposition (CVD), thermal evaporation, and metal-assisted chemical etching. These methods successfully reduced the texture size while most of these methods are expensive, resource intensive, and not generally designed for applications requiring large area production.[33] It can be seen that for the further development of new generation of low-cost c-Si solar cells, the fabrication of nanostructures is very important, which requires better understanding of the optical and electrical properties of the nanostructures and morphology management of them.

1.2 Research purpose

As described above, Si based solar cell is the current mainstream now, and reducing the manufacturing cost of solar cells is the market demand of great concern now, and this can be realized by the exploration of new device architectures and the implementation of new materials. Among them, the reduction of manufacturing cost has made the application of thin c-Si solar cells and c-Si heterojunction hybrid solar cells a development trend of new generation solar cells, and the application of Si nanostructures in these cell structures is of vital importance.

The reduction of the thickness of Si substrates and the combination of c-Si with new materials such as organic semiconductors, carbon nanotubes, and pervoskite place new demands on optimization of Si light confinement structures. Si textures fabricated by conventional wet etching methods are usually in micrometer size and unevenly distributed, making them difficult to be applied to next-generation c-Si solar cell structures. The fabrication of Si nanotextures, in turn, requires complex equipment. To overcome these problems, a new method is urgently needed to be developed to fabricate Si light confinement textures in nano scale simply and efficiently, as well as realizing the control of the morphology and distribution of Si textures. Thus in this study, we would like to optimize the Ag-assisted all-solution process to fabricated different Si nanotextures with both low etching margin and low fabrication cost, by employing Ag mask by electroless plating. We need Si nanostructures not only to have a size smaller than 1 μm and a uniformly dense distribution, but also to have a narrow size distribution,

in order to achieve efficient light absorption, reduced surface defects, and facilitate the fusion of Si textures with other semiconductor materials.

References

[1] https://www.weforum.org/agenda/2023/02/renewables-world-top-electricity-source-data

[2] https://www.gminsights.com/pressrelease/solar-silicon-wafer-market.

[3] Khatib H. IEA world energy outlook 2011—A comment[J]. Energy policy, 2012, 48: 737-743.

[4] Woodhouse M A, Smith B, Ramdas A, et al. Crystalline silicon photovoltaic module manufacturing costs and sustainable pricing: 1H 2018 Benchmark and Cost Reduction Road Map[R]. National Renewable Energy Lab.(NREL), Golden, CO (United States), 2019.

[5] https://www.vdma.org/international-technology-roadmap-photovoltaic

[6] Taguchi M, Yano A, Tohoda S, et al. 24.7% record efficiency HIT solar cell on thin silicon wafer[J]. IEEE Journal of photovoltaics, 2013, 4(1): 96-99.

[7] H. Sai et al., Progress in Photovoltaics: Research and Applications 27, 1061 (2019)

[8] El-Khozondar H J, El-Khozondar R J, Al Afif R, et al. Modified solar cells with antireflection coatings[J]. International Journal of Thermofluids, 2021, 11: 100103.

[9] El-Khozondar H J, Alshembari A A, Shabat M M, et al. Two layers corrugated semiconductor solar cell[J]. Optik, 2019, 181: 933-940.

[10] Peter Amalathas A, Alkaisi M M. Nanostructures for light trapping in thin film solar cells[J]. Micromachines, 2019, 10(9): 619.

[11] Yue G, Sivec L, Owens J M, et al. Optimization of back reflector for high efficiency hydrogenated nanocrystalline silicon solar cells[J]. Applied Physics Letters, 2009, 95(26).

[12] Banerjee S, Mandal S, Dhar S, et al. Nanomirror-embedded back reflector layer (BRL) for advanced light management in thin silicon solar cells[J]. Industrial & Engineering Chemistry Research, 2019, 58(28): 12678-12686.

[13] Pfeffer F, Eisenlohr J, Basch A, et al. Systematic analysis of diffuse rear reflectors for enhanced light trapping in silicon solar cells[J]. Solar Energy Materials and Solar Cells, 2016, 152: 80-86.

[14] Lin C C, Chuang Y J, Sun W H, et al. Ultrathin single-crystalline silicon solar cells for mechanically flexible and optimal surface morphology designs[J]. Microelectronic Engineering, 2015, 145: 128-132.

[15] Wang F, Zhang Y, Yang M, et al. Insights into nucleation engineering in Si pyramidal

texturing for high performance heterojunction solar cells applications[J]. Journal of Alloys and Compounds, 2018, 752: 53-60.

[16] Yang L, Liu Y, Wang Y, et al. Optimization of silicon pyramidal emitter by self-selective Ag-assisted chemical etching[J]. RSC advances, 2014, 4(47): 24458-24462.

[17] Wind R A, Hines M A. Macroscopic etch anisotropies and microscopic reaction mechanisms: a micromachined structure for the rapid assay of etchant anisotropy[J]. Surface Science, 2000, 460(1-3): 21-38.

[18] Nguyen C T, Koyama K, Tu H T C, et al. Texture size control by mixing glass microparticles with alkaline solution for crystalline silicon solar cells[J]. Journal of Materials Research, 2018, 33(11): 1515-1522.

[19] Li X, Bohn P W. Metal-assisted chemical etching in HF/H 2 O 2 produces porous silicon[J]. Applied Physics Letters, 2000, 77(16): 2572-2574.

[20] Zhang, Ming-Liang, et al. "Preparation of large-area uniform silicon nanowires arrays through metal-assisted chemical etching." The Journal of Physical Chemistry C 112.12 (2008): 4444-4450.

[21] Smith Z R, Smith R L, Collins S D. Mechanism of nanowire formation in metal assisted chemical etching[J]. Electrochimica Acta, 2013, 92: 139-147.

[22] Li G, Li H, Ho J Y L, et al. Nanopyramid structure for ultrathin c-Si tandem solar cells[J]. Nano letters, 2014, 14(5): 2563-2568.

[23] Zhong S, Wang W, Zhuang Y, et al. All-solution-processed random Si nanopyramids for excellent light trapping in ultrathin solar cells[J]. Advanced Functional Materials, 2016, 26(26): 4768-4777.

[24] Isabella O, Vismara R, Linssen D N P, et al. Advanced light trapping scheme in decoupled front and rear textured thin-film silicon solar cells[J]. Solar energy, 2018, 162: 344-356.

[25] Shen X, Sun B, Liu D, et al. Hybrid heterojunction solar cell based on organic–inorganic silicon nanowire array architecture[J]. Journal of the American Chemical Society, 2011, 133(48): 19408-19415.

[26] Moiz S A, Alahmadi A N M, Aljohani A J. Design of silicon nanowire array for PEDOT: PSS-silicon nanowire-based hybrid solar cell[J]. Energies, 2020, 13(15): 3797.

[27] Omer A A A, He Z, Hong S, et al. Ultra-thin silicon wafers fabrication and inverted pyramid texturing based on cu-catalyzed chemical etching[J]. Silicon, 2021, 13: 351-359.

[28] Gao Z, Geng Q, Wang Z, et al. Conformal PDMS films for strengthening flexibility and retaining absorption in pyramid ultra-thin c-Si solar cells[J]. Solar Energy, 2022, 247: 520-530.

[29] Bati A S R, Zhong Y L, Burn P L, et al. Next-generation applications for integrated perovskite solar cells[J]. Communications Materials, 2023, 4(1): 2.

[30] Um H D, Choi D, Choi A, et al. Embedded metal electrode for organic–inorganic hybrid nanowire solar cells[J]. ACS nano, 2017, 11(6): 6218-6224.

[31] Heinke R, Ehrhardt M, Lorenz P, et al. Dry etching of monocrystalline silicon using a laser-induced reactive micro plasma[J]. Applied Surface Science Advances, 2021, 6: 100169.

[32] Amalathas A P, Alkaisi M M. Fabrication and replication of periodic nanopyramid structures by laser interference lithography and UV nanoimprint lithography for solar cells applications[M]//Micro/Nanolithography-A Heuristic Aspect on the Enduring Technology. London, UK: IntechOpen, 2018.

[33] Q. Qing, S.K. Pal, B.Z. Tian, X.J. Duan, B.P. Timko, T. Cohen-Karni, V.N. Murthy, C.M. Lieber Nanowire transistor arrays for mapping neural circuits in acute brain slices Proceedings of the National Academy of Sciences of the United States of America, 107 (5) (2010), p. 1882

2 Experimental Methods

2.1 Sample Preparation Method

2.1.1 Radio frequency (RF) magnetron sputtering method

Sn-doped In2O3 (ITO) was deposited using a load-lock sputtering system (CS-200 manufactured by ULVAC, Inc.) A schematic diagram of the RF sputtering system is shown in Figure 2.1. The sputtering method is a phenomenon in which high-energy ion or atom bombardment of a target material causes the target atoms to be knocked out of its surface as particles, which can be used to deposit thin films.[1,2]

In the RF magnetron sputtering used in this study, a high-frequency voltage is applied between the target and substrate, making it possible to deposit films on insulator targets, which cannot be used with DC voltage due to ion charging problems. The deposition process is as follows. First, Ar is introduced into the high vacuum chamber, and after the flow rate is stabilized, high-frequency voltage is applied. The applied voltage causes Ar to collide with electrons and ionize into Ar^+ ions and electrons. Since the area of the substrate side is larger than that of the target, more electrons flow from the chamber side to the target side. As a result, the target side is negatively charged and the substrate side positively charged, and the generated Ar^+ ions accelerate and collide with the target side. In addition, a magnet is placed under the target and a magnetic field is applied to confine the electrons near the target. This allows more Ar^+ ions to be generated near the target, thereby improving the deposition rate.

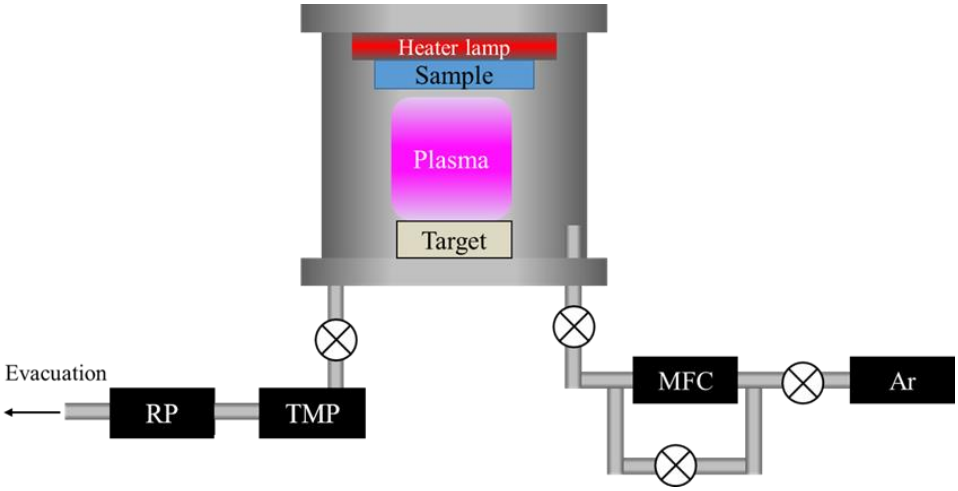

Figure 2.1 Schematic s diagram of the of Radio frequency magnetron sputtering

2.1.2 Plasma-Enhanced Chemical Vapor Deposition (PECVD)

Figure 2.2 shows a schematic diagram of the deposition chamber for the plasma-assisted chemical vapor deposition method.[3] In this study, i-a-Si:H, boron (B)-doped p-a-Si:H and phosphorous doped *n*-nc-Si:H layers were deposited by a multichamber PECVD system. The principle of film deposition is explained using an example of B-doped p-a-Si:H layer. A high-frequency voltage is applied while heating the substrate in a deposition chamber filled with raw material gases of SiH_4, B_2H_6, and H_2. At that time, the raw material gas becomes plasma, and various radicals (SiH_n^+, SiH_{2n}^+) are generated. The radicals react with atoms on the heated substrate surface or dangling bonds, forming a thin film.[4]

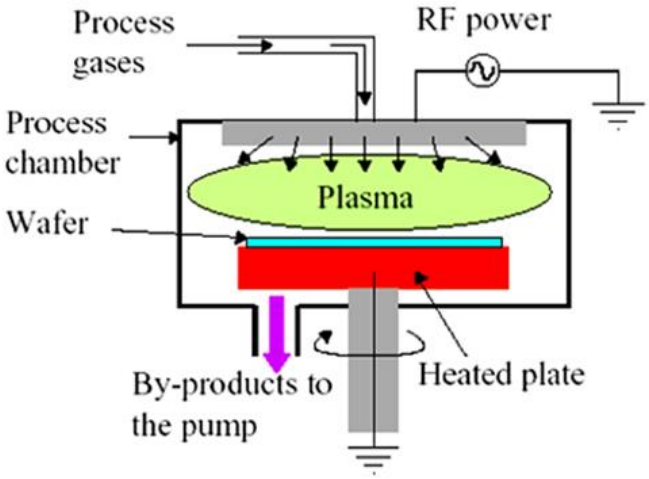

Figure 2.2. schematic diagram of the deposition chamber for the plasma-assisted chemical vapor deposition method

2.1.3 Vacuum Evaporation

This method was used for the deposition of electrodes for solar cells measurements. Figure 2.3 shows a schematic diagram of the vacuum evaporation equipment. The vacuum evaporation method is one of the deposition techniques that have been used for a long time. In this method, an electric current is applied to a high-resistance evaporation boat in a vacuum to generate heat. By placing the evaporation material on the boat, the evaporation material on the boat is heated and melts, evaporates, or sublimates. The particles of the gaseous material collide with the substrate and adhere to it, depositing a thin film. By placing a mask with a pattern between the sample and the source, it is possible to deposit metals in various shapes. In this experiment, Ag and Al(aluminum) were used as the evaporation materials, and tungsten was used as the evaporation boat.

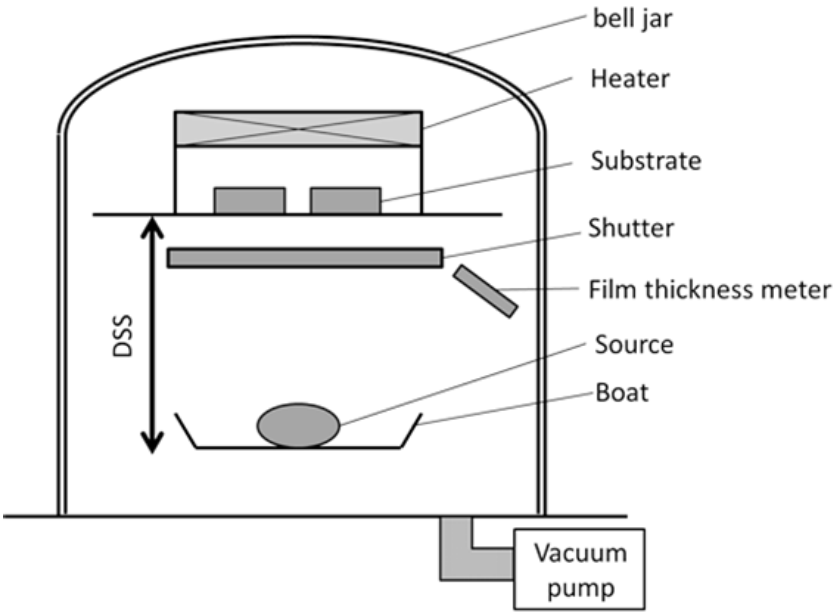

Figure 2.3 Schematic diagram of the vacuum evaporation equipment.

2.1.4 spin-coating

Spin coating is used for the fabrication of thin films to deposit uniform coating of organic materials on flat surfaces [5], the main advantage is the ability to produce very uniform films quickly and easily. The spin coating method includes three steps: batching, high-speed spinning, and evaporation to form the film(Figure 2.4).[6] Firstly, the material to be deposited on the substrate is diluted into a solvent, and then the solution is slowly dropped onto the substrate. When the substrate spins at a high speed, a uniform covering is formed under the joint action of the centripetal force and surface tension of the liquid. Most of the solvent is removed by evaporation during spinning and remained part by subsequent baking at high temperature. When the remaining solvent evaporates, a relatively flat film with a thickness ranging from a few nanometers to a few micrometers can be formed. The thickness of the film can be controlled by controlling the spinning time, rotation speed, drop volume, concentration and viscosity of the solution used. The spin-coating method is widely used in organic electronics and nanotechnology and builds on many techniques used in other semiconductor

industries.[7] Spin-coating is applied in this study to deposite SnO_2/perovskite/ spiro-MeOTAD layers for perovskite top cell and PEDOT:PSS for organic/Si hybrid solar cell.

Figure 2.4. Schematic diagram of spin coating process.

2.2 Measurement apparatus

2.2.1 Scanning Electron Microscope (SEM), Energy-Dispersive X-ray spectroscopy (EDX)

The surface morphology of the samples was observed using a scanning electron microscope (JSM-7001FA, manufactured by JEOL Ltd.). The electron acceleration voltage was set to 20 kV with the irradiation current flow of 15 A. By irradiating an electron beam from an electron gun in a vacuum chamber and scanning it against a sample, secondary electrons are generated from the area where the electron beam collided. Secondary electrons are less from the horizontal part and increase as the inclination increases, so that information on the unevenness of the sample surface can be obtained by expressing the intensity of the secondary electrons by contrast.[8]

Then, Energy-Dispersive X-ray spectroscopy (EDX) was used to perform elemental analysis of the samples. EDX is a method to detect element-specific characteristic X-rays generated when a sample is irradiated with electron beams and to obtain information on elements in the sample. During the experiment, the chamber was set to a vacuum below 10-4 Pa, the distance from the electron gun to the sample was 10 mm, the acceleration voltage was 20 kV, and the irradiation current was 12 mA. The schematic diagram of the equipment is shown in Figure 2.5.

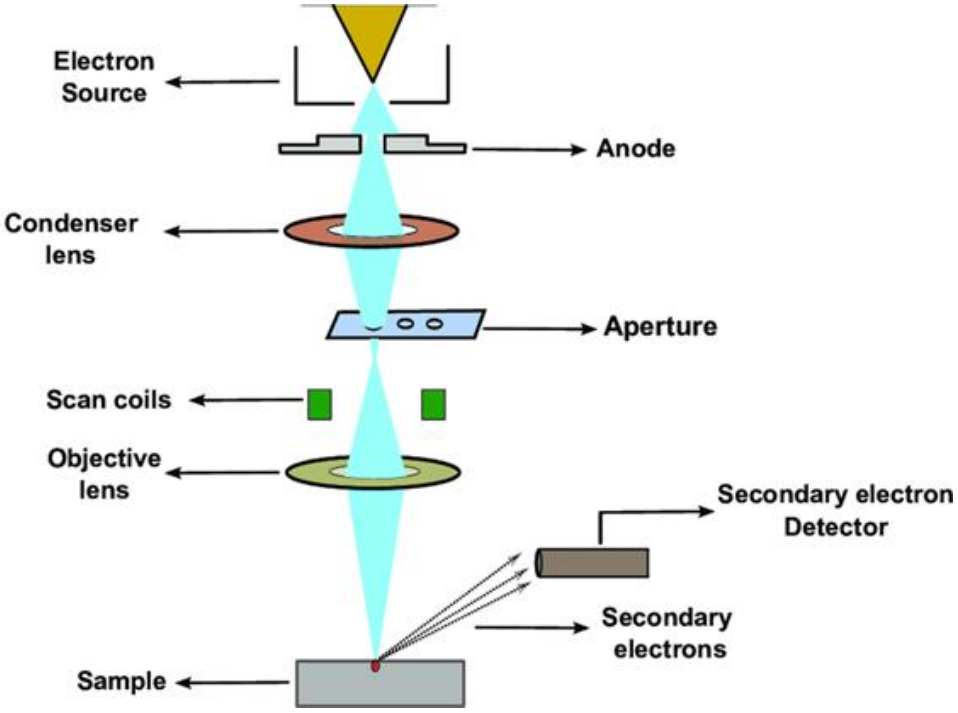

Figure 2.5. Schematic illustration of Scanning Electron Microscope.[9]

2.2.2 Spectrophotometer

To characterize the optical performance, reflectance and transmittance of the samples were measured by UV-VIS-NIR spectrophotometer (PerkinElmer, Lambda 950) equipped with an integral sphere (Lab-sphere, 150 mm RSA ASSY). Light emitted from the spectrophotometer enters the integrating sphere and then reaches the sample surface. The light reflected by the sample surface is repeatedly reflected in the integrating sphere, and detected by the detector to get the reflectance.[10] In the transmittance measurement, the light emitted from the spectrophotometer shoots on the sample first, and the transmitted light is repeatedly reflected in the integrating sphere until detected by the detector. The transmittance is measured. The 100% reflection baseline is measured with barium sulfate plate, and the 100% transmission baseline is taken without the sample. The schematic diagram is shown in Figure 2.6.

In this measurement, the reflectance and the transmittance for each wavelength are measured. After the measurement, the absorptance was determined from the obtained value by the equation (2.1).

Absorbance (λ) = 100%-reflectance (λ)-transmittance (λ) (2.1)

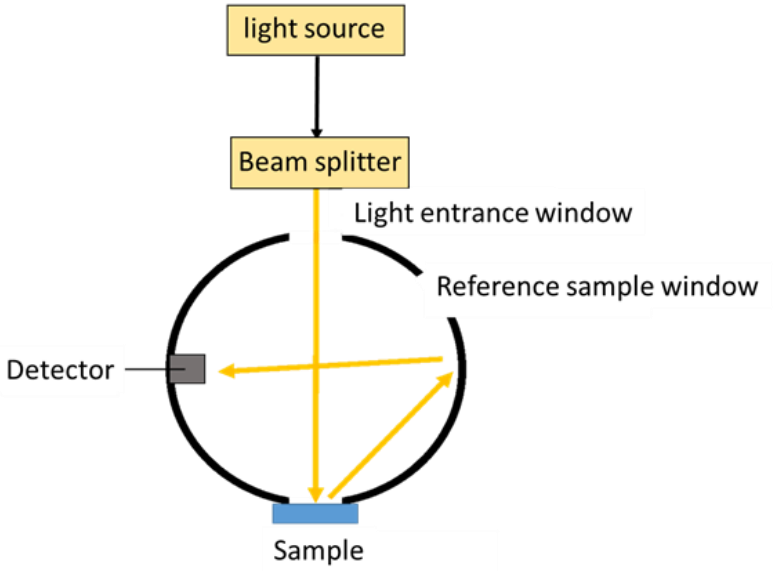

Figure 2.6. Schematic illustration of quasi-steady-state photoconductance (QSSPC) characterization (JASCO Corporation, V-570)

2.2.3 Transmission electron microscopy (TEM)

A TEM is an instrument used to obtain a magnified projection image of a sample, similar to an optical microscope. However, the light source used for optical microscopy has a wavelength in the human visible light range (400~800 nm), whereas the light source used for TME is an X-ray with a much smaller wavelength of 0.0025 nm at an acceleration voltage of 200 kV. The magnification can be changed by changing the acceleration voltage, etc., and the magnification range is wide enough to cover the observation of entire cells on the scale of tens of μm (several hundred times) to the observation of atomic arrangement structures on the sub-nm scale (several million times). In this study,

the cross-section of the devices was analysed by TEM at an acceleration voltage of 200 kV (JEOL JEM-ARM200F) at JFE Techno-Research Corporation.

2.2.4 Current-voltage (J-V) measurement

The current density−voltage (J−V) characteristics were evaluated using a dual-light solar simulator (Wacom, WXS-50S-L2) under standard test conditions (STC; 100 mW cm-2, air mass 1.5 global, 25℃). Figure 2. 7 shows the relationship between voltage and current density of a solar cell. From the figure, the current density at V = 0 is called the short-circuit current density (J_{SC}) and the voltage at I = 0 is called V_{OC}. J_{SC} is the maximum current density output by this solar cell and V_{OC} is the maximum voltage. The power that can be extracted from this solar cell is represented by the area enclosed by the dotted line in the figure, but the actual current density and voltage characteristics are smaller than the area shown by the dotted line (J_{SC} x V_{OC}) because of the curved shape.

When a load resistor RL is connected to a solar cell, the relationship between the voltage at both ends and the current density is I=V/RL, which is a straight line. The intersection of this straight line and the current density-voltage characteristic curve is the operating point, and the current density at that time is called the operating current density (Jop) and the voltage is called the operating voltage (Vop). The maximum output voltage Pmax can be obtained when the load is such that the area of Jop × Vop is the maximum. The conversion efficiency (η) is calculated by dividing Pmax by the incident light intensity Pin. Furthermore, it is called the curve factor (FF: Fill Factor) of the power (Vop x Jop) at the operating point (Pmax) and the area of the dotted line (V_{OC} x J_{SC}), and the conversion efficiency η can be calculated by V_{OC} x J_{SC} x FF.[11] The characteristics of a solar cell are evaluated by V_{OC}, J_{SC}, and FF, and the larger these values are, the higher the conversion efficiency and the higher the performance. The shape of the J-V curve also gives a rough idea of what factors affect performance degradation. Figure 2.7 shows the ideal J-V curve and the J-V curve when performance degradation is caused by various factors.

The ideal J-V curve is a rectangle formed by J_{SC} x V_{OC}. However, since the actual J-V curve is curved due to resistance and other factors, the curve is drawn such that it has an area

smaller than the J_{SC} x V_{OC} square. In a high-performance solar cell, the curve takes a shape closer to a rectangle, as shown in Figure 2.8(a).

From this point, the J-V curve is explained in the case of performance degradation due to resistance and other factors.[11] Figure 2.9 shows the equivalent circuit of a solar cell. If the parallel (shunt) resistance of the solar cell is small, the current generated by the light will flow into the parallel circuit, reducing the current flowing through the junction of the solar cell and lowering the voltage of the solar cell. Figure 2.8 (b) shows that the current at the operating point is decreasing, with a slope appearing from the J_{SC} area due to the decrease in the current flowing. Furthermore, for very low shunt resistance, Figure 2.8 (c) shows that the slope at J_{SC} is even larger and V_{OC} also decreases.

If the series (series) resistance is large, the current drops because of the power loss at that resistance. Figure 2.8(d) shows that the current decreases at high voltages, resulting in a slope from V_{OC} and a decrease in current. At very high voltage (Figure 2.18(e)), the slope increases further, J_{SC} also decreases, and performance deteriorates.

If a Schottky contact is present, rectangularity appears in that area. The ease of current flow changes as voltage is applied, resulting in an S-shaped curve as shown in Figure 2.7, an ideal solar cell, the series resistance should be zero and the shunt resistance infinite.

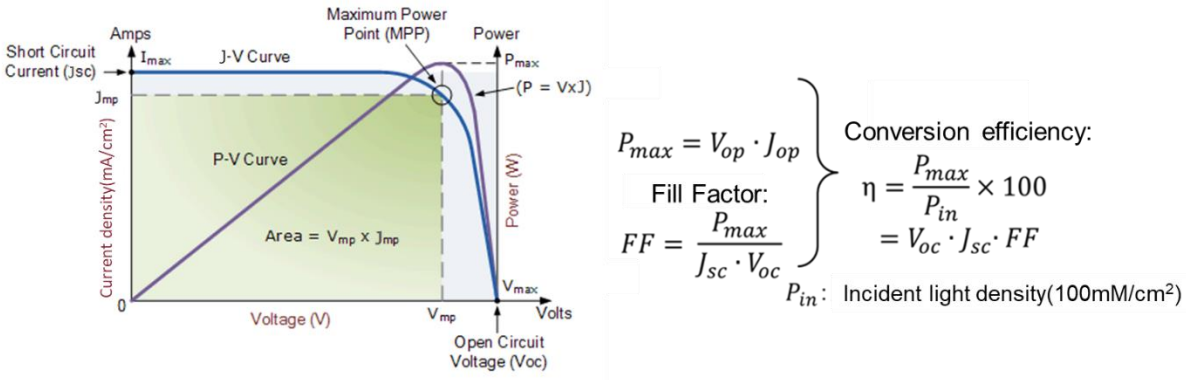

Figure 2.7. J-V characteristic evaluation.

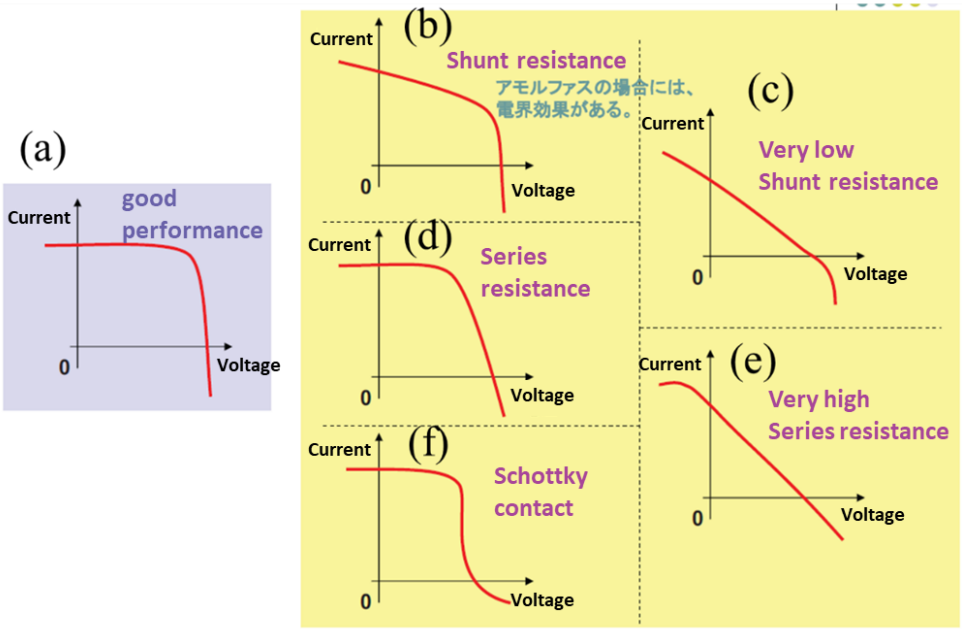

Figure 2.8. (a) Ideal J-V curve; (b) low shunt resistance; (c) very low shunt resistance; (d) high series resistance; (e) very high series resistance; (f) When Schottky junction is present.

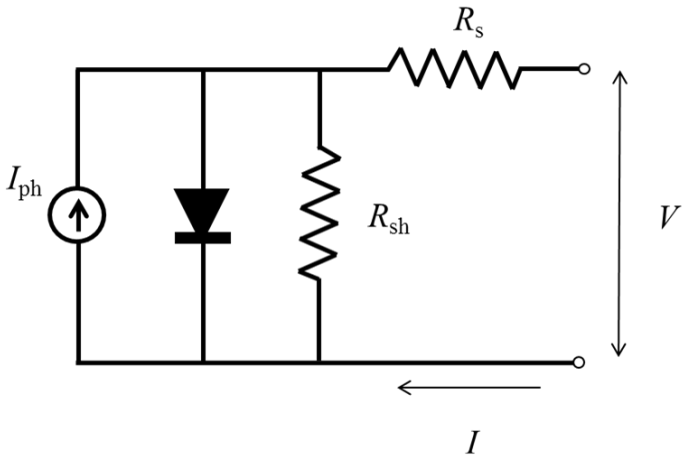

Figure 2.9. Equivalent circuit of solar cell.

2.2.5 External Quantum Efficiency (EQE)

External Quantum Efficiency (EQE) of solar cells, otherwise known as Spectral Responsivity or IPCE (Incident Photo-Electron Conversion Efficiency). External quantum

efficiency is used to characterize the ability of each incident photon to be converted into an electron and transmitted to an external circuit, and the unit of EQE is usually percentage. EQE measurement is one important method that is implemented to observe solar cells' behaviour in a specific range of wavelength.[12] The measurement principle of external quantum efficiency eqe is to illuminate the solar cell with adjustable-intensity bias light to simulate the working status of the cell under different lighting conditions, and at the same time measure the short-circuit current generated by the solar cell under the illumination of monochromatic light of different wavelengths, thereby Obtain the spectral response of the solar cell. During the measurement process, a white light source of continuous wavelength is first illuminated on the monochromator and forms monochromatic light of a specific wavelength, which is then modulated by the optical cutter into an AC light source of a specific frequency. The calibrated monochromatic light is incident on the surface of the solar cell, the same number of incident photons is illuminated on the solar cell under test, and the generated photocurrent signal is demodulated and read out by the lock-in amplifier. By dividing the radiant energy of the incident light and the generated current, we can obtain the spectral response value at a certain wavelength. By continuously changing different wavelengths for inspection, the SR spectrum of the component can be obtained. After unit conversion, the EQE spectrum can be obtained. The schematic diagram is shown in Figure 2.10.

In this study, the EQE of monocrystalline Si-based solar cells was measured with an EQE setup (Bunkou Keiki, CEP-25BXS) to explore the influence of Si nanostructures on the cell efficiency in different light wavelength ranges.

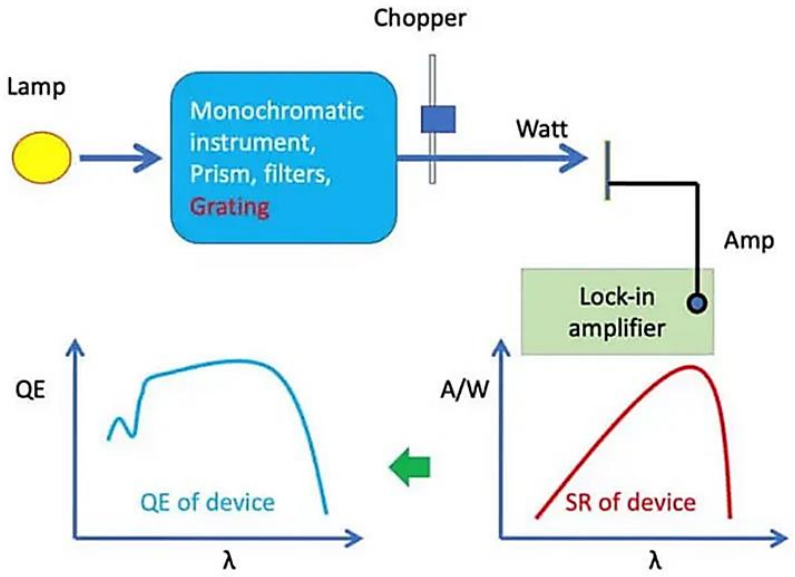

Figure 2.10. Schematic diagram of the test principle of external quantum efficiency EQE/spectral response SR.

References

[1] K. Fukutani, Curr. Opin. Solid. State Mater. Sci. 6, 153 (2002).

[2] 小林春洋 「スパッタ薄膜 基礎と応用」日刊工業新聞社 (1993).

[3] 尾池工業株式会社「スパッタリングとは」、http://www.oike-kogyo.co.jp/dry-coating/making/sputtering.html.

[4] 東方化研株式会社 イオンプレーティング部, ホームページ(PECVD).

[5] Yilbas B S, Al-Sharafi A, Ali H. Self-cleaning of surfaces and water droplet mobility[M]. Elsevier, 2019.

[6] https://www.inseto.co.uk/what-is-spin-coating-ikb-075/

[7] Cai G, Xue L, Zhang H, et al. A review on micromixers[J]. Micromachines, 2017, 8(9): 274.

[8] Kobelkokaken HP https://www.kobelcokaken.co.jp/leo/en/.

[9] Marturi N. Vision and visual servoing for nanomanipulation and nanocharacterization in scanning electron microscope[D]. Université de Franche-Comté, 2013.

[10] P. Campbell et al., Solar Energy Materials & Solar Cells, 65 369-375 (2001)

[11] http://www.pveducation.org/

[12] Ananda W. External quantum efficiency measurement of solar cell[C]//2017 15th International Conference on Quality in Research (QiR): International Symposium on Electrical and Computer Engineering. IEEE, 2017: 450-456.

3. Si nano-pyramid structure and application in SHJ solar cell

3.1 Introduction

3.1.1 Background

3.1.1.1 The needs to reduce texture size

Currently, crystalline Si solar cells account for ~95% of the world photovoltaic market.[1] The share of monocrystalline Si solar cells has exceeded that of multi-crystalline Si ones in recent years, because of the strong demands for higher-efficiency devices and the cost reduction of monocrystalline Si ingots. In monocrystalline Si solar cells, random up-right pyramids consisting of {111} facets are commonly used to reduce the optical reflection loss and enhance the light absorption within Si absorbers close to the Lambertian limit.[2,3] Random up-right pyramids with a size of 2-10μm are easily formed by anisotropic alkaline etching that utilizes the difference in etching rates between different crystal facets of Si.[4]

In recent years, there has been an urgent need to reduce the size of Si pyramid texture under 1um for some reasons. First, smaller pyramids are well suited to thin Si solar cells. In particular, thin Si wafers with a thickness below 100 μm have received widespread attentions aimed at further cost reduction.[5-7] In addition, the excellent mechanical flexibility of thin Si solar cells opens the new opportunities as light-weight and flexible devices for integrated photovoltaic applications.[8] Compared to the conventional micrometer-sized Si pyramids (micropyramids), the nanometer-sized pyramids (nanopyramids) are advantageous particularly for thin Si wafers since they can be formed with minimal etching margins.[9,10] Second, smaller pyramids allow to form finer screen-printed Ag fingers by minimizing spreading of the Ag paste, which in turn improves the photocurrent density in Si solar cells and reduces the Ag consumption.[11] Third, nanopyramids are more favorable to perovskite/Si tandem cells than micropyramids[12,13], as surface textures with a smaller peak-to-bottom height offer the potential for depositing a high-quality perovskite thin film (typical thickness is < 1 μm) conformally on top of the textured Si surfaces by means of low-cost solution-based techniques.

3.1.1.2 Si nano-pyramids fabrication

In general, the size of pyramids becomes smaller by forming nucleation sites more densely on the Si surface. The promotion of nucleation can be realized with masking materials processed by either bottom-up approaches such as metal nanoparticles, or top-down approaches such as laser-interference lithography[14] and nano-imprint lithography.[15] Ohta et al. reported that Si nanopyramids with a size of 400 - 600 nm can be formed uniformly by using self-assembled Ge islands as etching masks.[16] Similarly, Zhong et al. reported that Ag nanoparticles pre-deposited on Si wafers by a solution process can be used as etching masks for the following alkaline etching process.[17,18]

From the industrial perspective, however, the etching process should be as simple as possible because the multi-step approaches are generally complex and may require additional process equipment. Recently, one-step approaches for processing nanopyramids were also investigated by several groups. Alsafour et al. reported that the size of pyramids can be controlled down to 1μm by adding K_2SiO_3 in an alkaline solution.[19] They concluded that K_2SiO_3 is effective to control the etching rate and promote the nucleation. In addition, Nguyen et al. reported that the size of pyramids can be controlled to 0.3–2μm by adding glass beads in an alkaline solution and mixing them vigorously.[20] In this case, the nucleation is promoted by breaking H_2 bubbles on the Si surface physically with glass beads, as the chemical reaction is blocked by the H_2 bubbles. However, no solar cell results by these methods have been reported yet.

3.1.2 Research purpose

In this work, we propose a novel one-step solution method that enables us to fabricate nanopyramids on monocrystalline Si surface with a minimal etching margin. The process is carried out by immersing Si wafers into a mixed solution of KOH, $AgNO_3$, HF, and additives. The simultaneous presence of Ag ions (Ag^+) and hydroxide ions (OH^-) in the solution permits the continuous generation of Ag nanoparticles (NPs) during the anisotropic etching process, which function as etching masks. The average size of

pyramidal textures can be widely controlled by the concentration of $AgNO_3$ in the solution, from a few micrometers down to <500 nm. The Si wafers with nanopyramid textures exhibit excellent optical performance, which leads to an efficiency improvement in Si heterojunction (SHJ) solar cells. The results obtained in this work provide new opportunities for high-efficiency and low-cost Si solar cells and their application to perovskite/Si tandem cells, since it has been demonstrated that the efficiency of perovskite/Si tandem cells with fully textured c-Si is effectively improved compared to that with single-side texturing configuration.[21]

3.2 Experimental Details

Phosphorus-doped n-type Czochralski (CZ)-grown monocrystalline Si wafers (double-side-polished, 1-5 Ω· cm, <100>-oriented) with a thickness of ~200 µm were used for the etching experiments. The Ag-assisted alkaline etching process is schematically shown in Figure 3.1. After cleaning processes with acetone and deionized water, the planar Si wafer was textured by dipping in four different kinds of mixed solution contains the following components: KOH, surfactant (Pure Etch TK81, Hayashi Pure Chemicals Ltd.)(), organic masking material (Pure Etch TT72, Hayashi Pure Chemicals Ltd.), and a $AgNO_3$ solution of HF (46%-48%): $AgNO_3$: DI water (10 ml: 0.1 g: 40 ml), for 15 minutes at 70°C. As shown in the table 3.1, the concentration of $AgNO_3$ solution was varied from 0 M to 1.2 mM, and the other conditions in the etching solution were fixed, which were 6% for KOH solution, 13% for TK81 solution, and 8% for TT72 solution. As a control, four groups of alkaline etching solutions with different compositions were utilized: group A: KOH solution, TK81 and TT72 solutions; group B: KOH solution only; group C: KOH solution and TK81 solution; group D: KOH solution and TT72 solutionFor the reference micropyramid textures, a planar Si wafer was textured by the mixed solution without adding the $AgNO_3$ solution under the same condition. After etching, the samples were immersed in HNO_3 solution to remove the residual Ag.

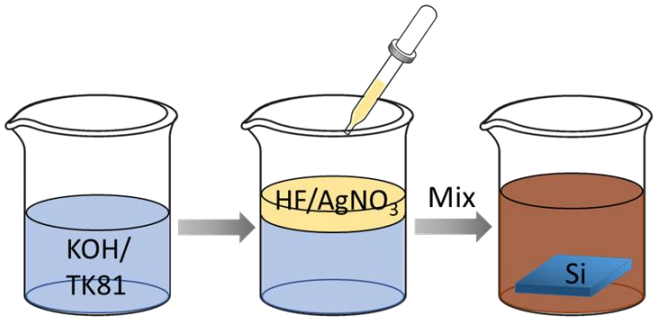

Figure 3.1. Schematic diagram of Ag-assisted alkaline etching process

Table 3.1. The composition of four different etching solutions for Si anisotropic etching

	A	B	C	D
	Reference (conventional micro-TEX [1])			
Etchant	KOH	KOH	KOH	KOH
Surfactant	TK81	×	TK81	×
Masking	TT72	×	×	TT72
$AgNO_3$	0-1.2mM	0-1.2mM	0-1.2mM	0-1.2mM

3.3 Si nanopyramid fabrication

3.3.1 Impact of Ag^+ concentration

We first explored the effect of Ag^+ concentration in the etching solution on the formation of Si pyramids. A matrix of top-view SEM images in Figure 3.2 shows the etching results of 16 textured Si wafers processed with 4 different alkaline solutions (Figure 3.2 a, b, c, d) and 4 different Ag^+ concentrations of 0, 0.8, 1 and 1.2 mM. Among them, TK81 is a surfactant - an organic solvent that can milder the reaction rate - and TT72 plays the role of masking.[22] It can be seen in Figure 3.2 (a1-4) that micron-sized Si pyramids are formed by our standard etching process (KOH + TT72 + TK81), but the size distribution is rather spreading and hardly changed by modifying the concentration of Ag^+. In contrast, alkaline etching in pure KOH solution results in only few isolated pyramid islands as shown in Figure 3.2 b1 because of the lack of nucleation sites. This situation is not improved by adding $AgNO_3$, which is expected to generate nucleation

sites, probably because the excess etching rate in this solution hinders the formation of nucleation.[23] Adding the masking material TT72 into the KOH etching solution results in uniformly distributed Si pyramids with a size of several micrometers (Figure 3.2 c1). With the presence of Ag^+, Si textures shrink in size but with very sparse and uneven distribution (Figure 3.2 c2-4), which can be attributed to competing masking effects by Ag NPs and TT72, and to the excess etching rate. It can be seen in Figure 3.2 d that the average size of Si pyramids can be effectively reduced from 1.8 µm to 565 nm by increasing the Ag^+ concentration in the alkaline solution with the surfactant TK81, which is Ag-assisted etching solution. This indicates that the combination of the Ag^+ solution and surfactant is the key to form nanopyramids.

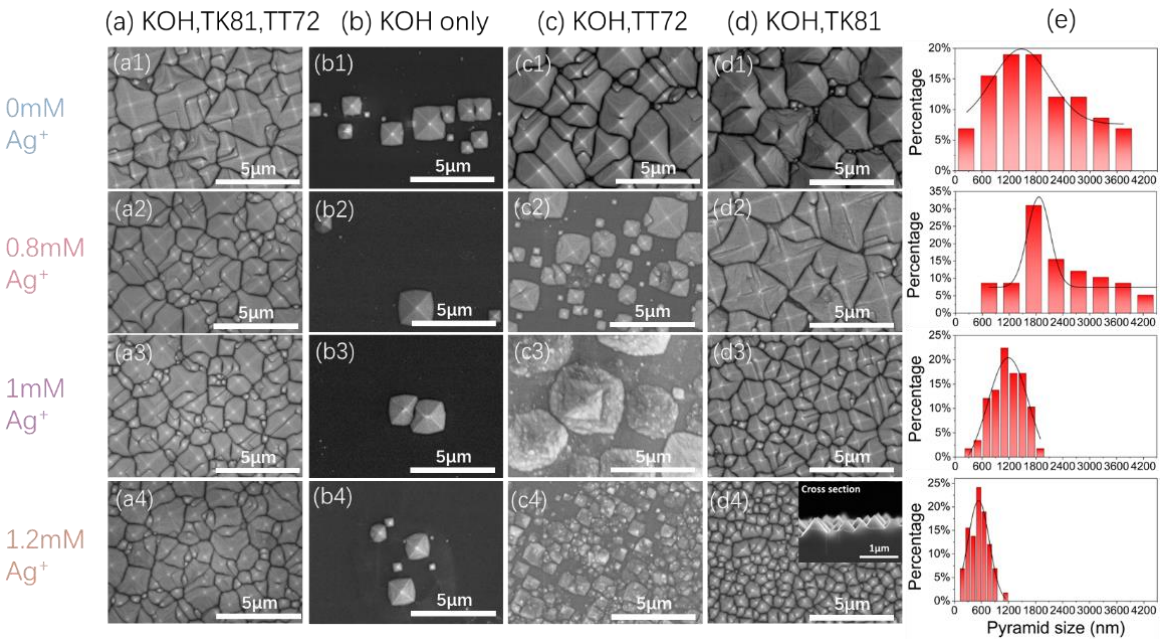

Figure 3.2. Top-view SEM images of 16 textured Si wafers processed with alkaline solutions of 4 different compositions: group(a) KOH, TK81, TT72(Reference etching solution); group (b) KOH; group (c) KOH, TT72; group (d) KOH, TK81 (Ag-assisted etching solution)and different $AgNO_3$ concentrations of 0mM, 0.8mM, 1mM and 1.2mM; group (e) size distribution of Si pyramids in group (d).

Further, Figure3.3 shows the SEM images of the Si surface after etching for 1 min at different Ag^+ concentrations before removal of the Ag nanoparticles(NPs) with HNO_3 solution, and it can be seen that the number of Ag NPs remaining on the surface of the Si after the etching increased with the concentration of the Ag^+ in the etching solution, which also proves that the number and density of the Ag NPs generated on the Si surface during the etching reaction are proportional to the concentration of the Ag^+. What's more, with the presence of Ag makes the initially generated Si pyramid smaller in size, and the reaction rate is gradually accelerated with the increase of the Ag^+ concentration, and the nucleation sites of the Si pyramids are more densely packed. This indicates that the Ag particles play a role in accelerating the reaction rate and increasing the nucleation sites. Meanwhile, measurement results show that the concentration of Ag^+ in the etchant does not affect the aspect ratio of the Si pyramid, and the aspect ratios of the Si pyramid sizes obtained at four different Ag^+ concentrations are all around 0.6-0.7.

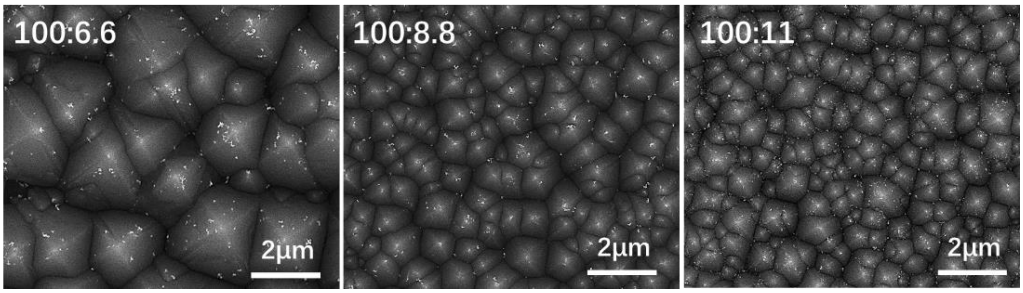

Figure 3.3 SEM images of the Si surface after etching for 1 min at different Ag^+ concentrations before Ag removal.

These different surface morphologies impact on the spectral reflectance. The reflectance of Si surface decreases with the increase in the Ag^+concentration from 0.8 to 1.2 mM as shown in Figure 3.4. The nanopyramids obtained with the 1.2 mM Ag^+ concentration outperforms the standard micropyramids, showing the lowest reflectance among the samples investigated. This result can be attributed to the improved light in-coupling effect by the sharp nanopyramids with uniform size distribution as confirmed in Figure 2d. It is also worth noting that the size distribution in Si nanopyramids is relatively narrow, which is known to be beneficial to reduce the

surface reflectance. [24] Furthermore, the etching margin is reduced from 3.3 µm of the reference method to 1.7 µm with the Ag-assisted etching method.Another possible reason for the improved light in-coupling is the increase in the base angle (shaper pyramids),[25] though we have not yet confirmed this experimentally.

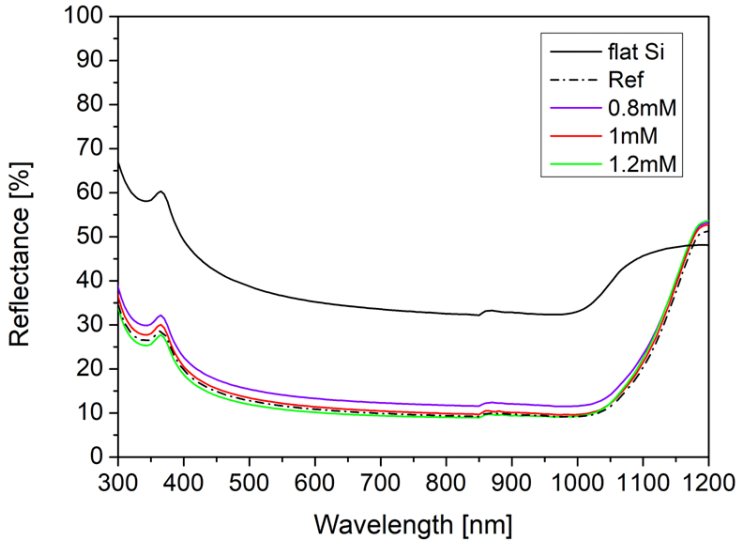

Figure 3.4. Reflectance of the Si pyramids fabricated by conventional alkaline etching and Ag-assisted alkaline etching with $AgNO_3$ concentrations of 0.8mM, 1mM and 1.2mM.

3.3.2 Impact of etching time

Figure 3.5 demonstrates the SEM images of the Si texture size change with etching time from 30s-30min under the condition of $AgNO_3$ concentration of 1.2 mM, TK81 of 90ml, and reaction temperature of 70℃. It can be seen that when the etching time is 30 seconds, the Si pyramids are in the nucleation stage. Since the uniformly distributed Ag nanoparticles generated on the Si surface act as etching mask, the distribution of the Si Pyramids is very uniform and dense during the nucleation stage. While as the etching time increases, Pyramids gradually increase in size with the same aspect ratio of around 0.6-0.7, but with the average size still under 1µm even the etching time is 30min. At the same time, flat portion on the Si surface that remains unetched can be observed within the etching time of 10 min, which increases the light reflectivity

of the Si texture. The average size of the Si texture within 15 min is less than 1 um, and after continuing to prolong the etching time to 30 min, size distribution of the Si pyramids gradually widens, with some Si pyramids exceeding 1μm. It can therefore be concluded that the etching time mainly affects the average size and size distribution of the Si pyramids. The nanoscale size of the Si pyramids benefits from the uniform nucleation sites caused by the dense Ag particle etch mask formed on the Si surface. The optimal etching time is 15 min to obtain densely distributed Si nanopyramid textures.

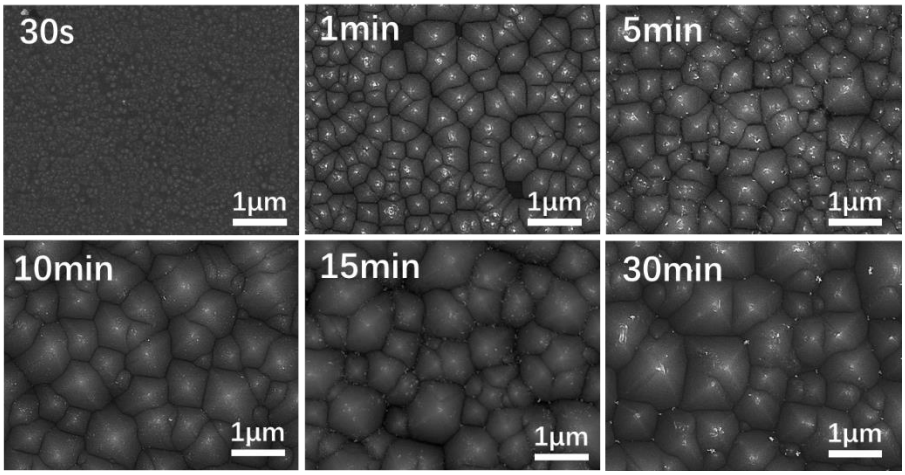

Figure 3.5. SEM images of the Si texture size change with etching time of 30s, 1min, 5min, 10min, 15min and 30min under the condition of AgNO3 concentration of 1.2 mM, TK81 of 90ml, and reaction temperature of 70℃.

3.3.3 Impact of etching temperature

Figure 3.6 demonstrates the top and cross-section SEM images of the variation of the texture morphology of the Si pyramid with the etching temperature at $AgNO_3$ concentration of 1.2 mM and an etching time of 15 min. It can be seen that the etching reaction rate is accelerated with increasing temperature. At 60℃, the obtained Si pyramids are larger in size and cannot be uniformly distributed, with remnants of flat parts that have not been etched. At 70℃, the size of the Si pyramid decreases, and the distribution is uniform and dense. When the etching temperature was further increased

to 80℃, the size of the Si pyramid increased again. As the temperature increases, the size of the Si pyramids first decreases and then increases slightly; while the distribution and size distribution of the Si pyramids become denser as the temperature increases. Studies have shown that the etching rate is proportional to the etching temperature.[26, 27] Therefore, the etching reaction speed is relatively slow with the reaction temperature of 60℃, and the H_2 bubbles generated by the reaction between Si and KOH escape slowly, and are easy to attach to the Si surface to hinder the further occurrence of the etching reaction, resulting in a larger Si pyramid size and the formation of unetched flat areas. And as the etching temperature increases, a suitable reaction rate is reached, and the formation of Ag nanoparticles and the escape of H_2 bubbles are brought to a dynamic equilibrium, allowing the etching mask of Ag nanoparticles to be fully utilized. And further increase in the etching rate makes the etching process too long within the same time, which has the same effect as increasing the etching time, leading to an increase in the size and widening of the size distribution of the Si pyramids. The aspect ratios of the Si pyramid sizes obtained at different temperatures are in the range of 0.6-0.7. In conclusion, 70℃ is the optimum etching temperature. Figure 3.7 shows the light reflectance of the Si pyramid texture at different etching temperatures, which is in agreement with the results obtained from SEM observations, the lowest light reflectance was obtained for the Si pyramid texture at 70 ℃ due to the dense distribution and homogeneous texture size.

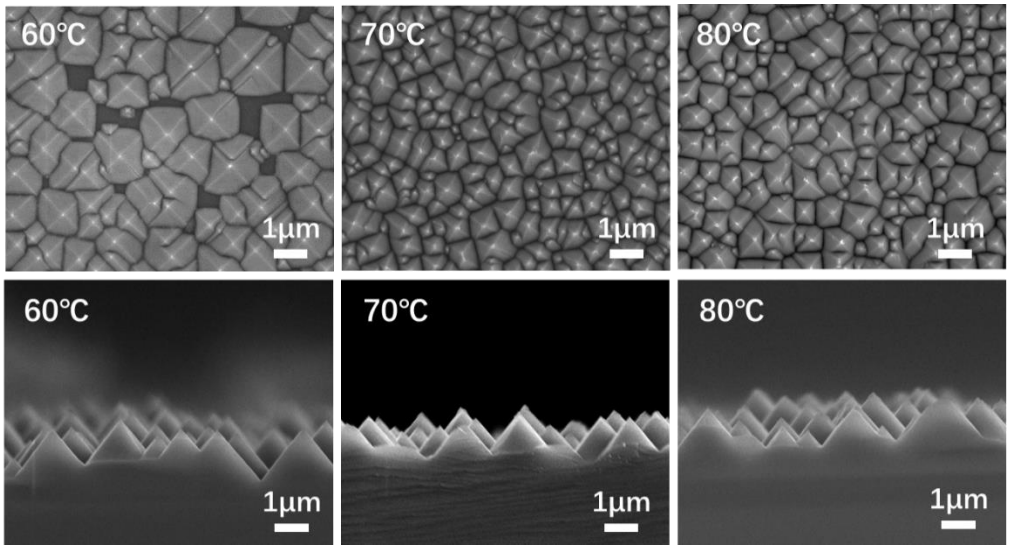

Figure 3.6. Top and cross-sectional SEM images of the Si pyramids etched under different etching temperaturws of 60℃, 70℃ and 80℃ at AgNO3 concentration of 1.2 mM and an etching time of 15 min.

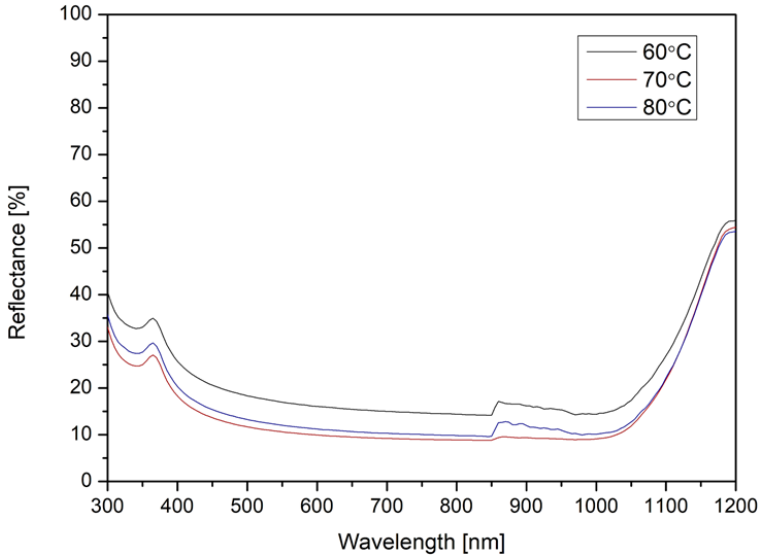

Figure 3.7. Light reflectance of the Si pyramid texture etched under different etching temperatures of 60℃, 70℃ and 80℃

3.3.4 Impact of surfactant TK81 amount

Figure 3.8 demonstrates the top view SEM image of the variation of the texture morphology of the Si pyramid when the TK81 concentration is 13%, 24% and 35%, respectively with Ag concentration varying from 0,8mM to 1.2mM. The other

etching conditions are fixed, with etching time of 15 min under 70℃. It can be seen that the texture size of the Si pyramid gradually decreases with the increase of TK81 concentration. This is due to the fact that TK81 is a surfactant that slows down the etching reaction, in the other word, the rate of pyramid growth. What's more, surfactant TK81 also slows down the escaping rate of H_2 bubble, allowing more Ag nanoparticles to remain on the Si surface, and therefore allowing more and denser nucleation sites to have the opportunity to form, resulting in smaller nanoscale Si pyramids. When the concentration of TK81 was 35%, we obtained the smallest Si pyramid texture so far with an average size of 390 nm. (Figure 3.8)

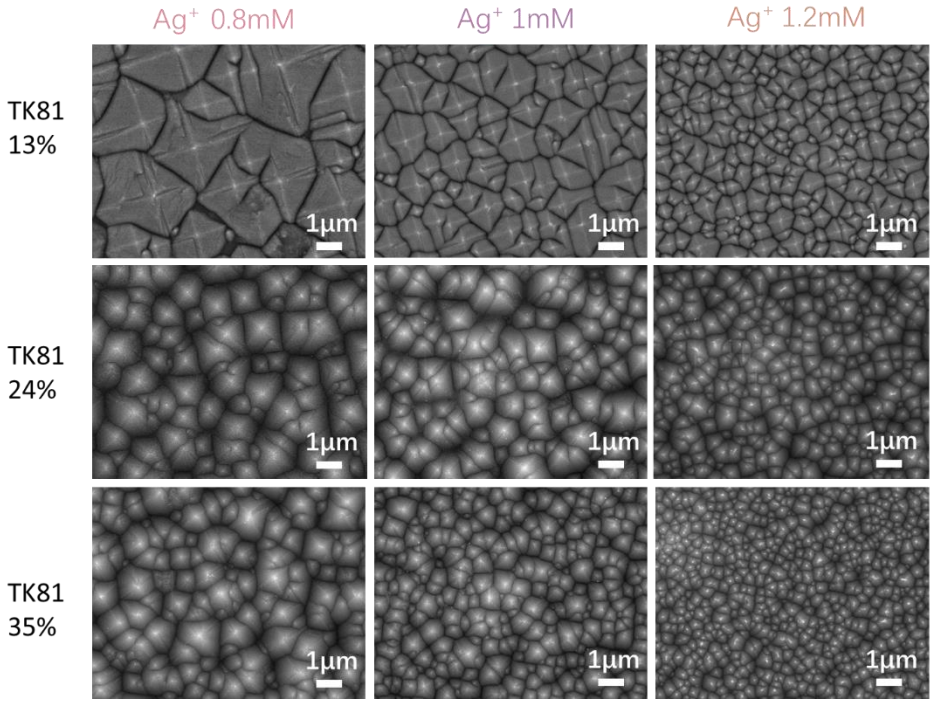

Figure 3.8. Top view SEM images of the variation of the texture morphology of the Si pyramid when the TK81 concentration is 13%, 24% and 35% with Ag concentration varying from 0,8mM to 1.2mM.

3.4 Mechanism

3.4.1 Anisotropic alkaline etching

We herein discuss the mechanism of the Ag-assisted alkaline etching process, which provides a wide range of size tunability in Si pyramid textures from few microns to sub-microns with improved size distribution. As well known, Si pyramid structures are formed by anisotropic etching due to the different etching rates between the {100} and {111} planes. However, Si surface will be etched parallel downward under an intense etching reaction, due to the the reduced difference in the etching rates in different directions. Thus the etching rate must be controlled at an appropriate range. [28]

Figure 3.9 (a) shows the theoretical schematic illustrations of the three main steps for the formation of pyramidal textures in the standard etching process. First, Si reacts with an alkaline solution according to the following chemical equation,

$$\mathrm{Si} + 2\mathrm{OH}^- + \mathrm{H_2O} \rightarrow \mathrm{SiO_2(OH)_2}^{2-} + 2\mathrm{H_2}\uparrow \ . \qquad (3.1)$$

Generated hydrogen (H_2) bubbles directly adhere to the Si surface and work as a barrier to suppress the chemical reaction.[29] The poor bubble detachment leads to insufficient pyramid nucleation and results in poor texture uniformity and a low etching rate (Figure 2(b)). It is known that the size of Si pyramids can be effectively reduced by continuously destroying the newly generated H_2 bubbles during etching.[30] For this purpose, a surfactant is utilized to increase the wettability of the etchant, which promotes the H_2 bubbles to leave the surface quickly and helps the etchant to fully contact with the Si surface.[31] Besides, masking material in etching solution creates the starting points for pyramid nucleation by attaching to the Si surface and hence stopping the corrosion reaction by OH^- locally. The more nucleation sites there are, the more uniform and denser Si pyramids are formed after etching. However, growing H_2 bubbles are prone to carry away the polymer flakes contained in TT72, resulting in the formation of flat areas.

Therefore, the keys to control the size of pyramids are (i) the stability and the density of masking materials for providing dense nucleation sites on the Si surface, and (ii) the quick removal of H_2 bubbles to promote the reaction of etching components with the Si surface.

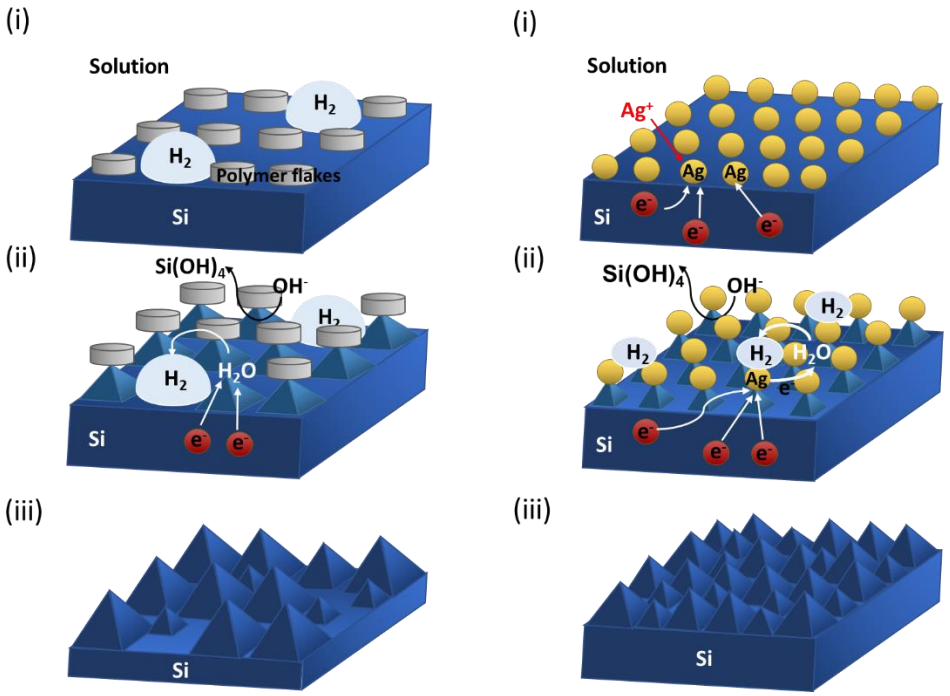

(a) Conventional alkaline etching (b) Ag-assisted alkaline etching

Figure 3.9. Schematic demonstrations are proposed for possible mechanisms of (a) Cnventional alkaline etching and (b) Mechanism Ag-assisted alkaline etching: (i) electroless Ag plating on Si substrate; (ii) Ag-assisted anisotropic alkaline etching; (iii) Formation of the Si nanopyramid structures.

3.4.2 Ag-assisted alkaline etching

Figure 3.9 (b) illustrates a possible working mechanism of the Ag-assisted alkaline etching method, where the Ag NPs act as masking material instead of polymer flakes as well as promoting the detachment of H_2 bubbles.A tan suspension is observed when the HF:$AgNO_3$ solution is added to the alkaline solution. It is noted that the precipitation

increases with increasing concentration of $AgNO_3$. However, when the ratio of $AgNO_3$ to KOH exceeds a certain value, the solution becomes clear instantly. This can be due to the following chemical reactions,

$$KOH + AgNO_3 \leftrightharpoons AgOH + KNO_3 \ , \quad (3.2)$$

$$2AgOH \rightarrow Ag_2O \downarrow + H_2O. \quad (3.3)$$

The reaction between KOH and $AgNO_3$ produces AgOH precipitates, which are unstable and can be further decomposed into Ag_2O, a kind of insoluble black-brown precipitate, making the solution to appear tan suspension. When the amount of $AgNO_3$ exceeds the given KOH, the reaction of Eq. (2) shifts to the left until the KOH is completely consumed and the solution contains only $AgNO_3$, where the clarified liquid state is restored again. Within the critical point, the reaction remains in equilibrium and results in the coexistence of Ag ions (Ag^+) and hydroxide ions (OH^-). Consequently, two kinds of reaction occur after the Si substrate is immersed in the mix solution: (i) electroless Ag plating to form Ag NPs on Si surface due to the stronger oxidability of Ag^+ than that of H^+(hydrogen ions), and (ii) anisotropic alkaline etching.[32,33]

Here the fluoride ions (F^-) in the solution participate in the reaction of Ag NP formation. The series of reactions occur at the Si surface as follows:

$$Si + 6F^- \rightarrow SiF_6{}^{2-} + 4e^- \ , \quad (3.4)$$

$$Ag^+ + e^- \rightarrow Ag \ , \quad (3.5)$$

$$Si + 6F^- + 4Ag^+ \rightarrow SiF_6{}^{2-} + 4Ag \ . \quad (3.6)$$

In this study, Ag NPs are continuously formed on the Si surface during the etching process, creating uniform and dense nucleation sites. This can be confirmed from the SEM and EDX images of the Si surface after etching for 1 min as shown in supplementary data

Figure 3.9; Ag NPs with a size of ~ 10 nm are identified on the Si surface and they tend to gather on top of the pyramids, indicating that they act as etching masks.

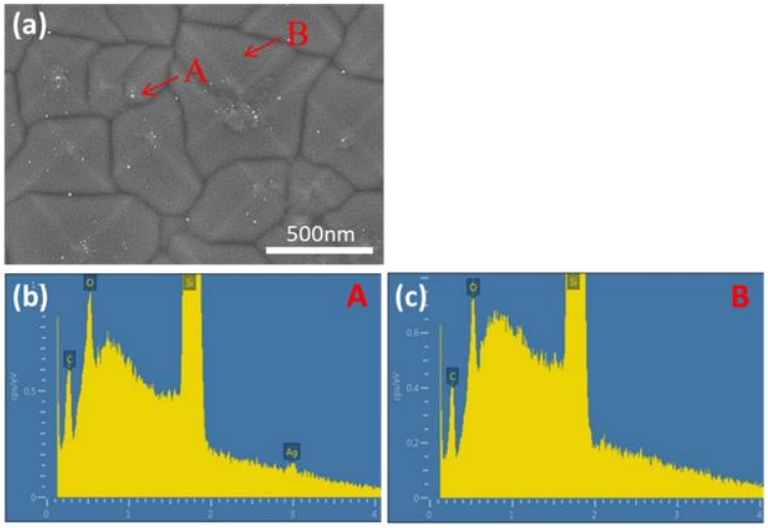

Figure 3.10. (a) Backscattered electron image of a Si nanopyramid texture prepared by Ag-assisted alkaline etching method with 1.2 mM $AgNO_3$, and (b, c) EDX spectroscopy spectra analyzed for two different measured positions on the Si surface.

In the meanwhile, H_2 bubbles are generated preferentially on Ag nanoparticles instead of Si surface due to the higher electronegativity of Ag,[34] which is expected to promote the detachment of finer H_2 bubbles from the Si surface. To confirm this, the generation of H_2 bubbles under different etching conditions is compared as shown in Figures. 3.11 (a)-(c). Under the reference etching condition, H_2 bubbles escape slowly in large size as shown in Figure 3.11 (a). In contrast, finer H_2 bubbles are generated intensively for the case of KOH/$AgNO_3$ etching solution as shown in Figure 3.11 (b). However, such an intensive reaction would wash away Ag NPs immediately from the Si surface, and therefore they are unable to produce nucleation sites constantly. Such an intensive reaction and generation of H_2 bubbles are suppressed effectively by adding the surfactant (TK81), as shown in Figure 3.11 (c). The effect of the surfactant can be confirmed by the decrease in the etching rate from 0.5 to 0.1 μm/min by adding the

surfactant, this milder reaction rate is likely to allow Ag NPs to stay on Si surface for a while and act as etching masks. In this study, Ag NPs aids the formation of nucleation sites, while TK81 moderates the generation of H_2 bubbles, their combined effect resulting in finer pyramids as shown in Figure 3.2 (d4). From these results, we conclude that the etching condition that provides fine and dense masking and appropriate etching rate is crucial to obtain the precise size control of nanopyramids with good uniformity. This provides a guideline to reduce the texture size further, i.e., combining more dense nucleation sites with a slower etching rate. In fact, we succeeded in producing Si nanopyramids with an average size of 400 nm with an even denser arrangement and more uniform size distribution, as shown in Figures 3.11 (d,e,f), by further increasing the concentration of surfactant to three times the original in the etching solution. Unfortunately, the reflectance of this sample is elevated in the long wavelength range since the texture size becomes smaller than the incident light wavelength, which results in slight decreases in J_{SC} and cell efficiency. However, Si nanopyramids as small as 300 nm are very promising for the use in perovskite/Si tandem solar cells [35,36] and Si/organic hybrid heterojunction solar cells [37], because nanotexture helps to greatly improve front light absorption, while enable excellent perovskite/organic film formation, which open the possibility of depositing thin films on textured Si using a solution-based coating process.

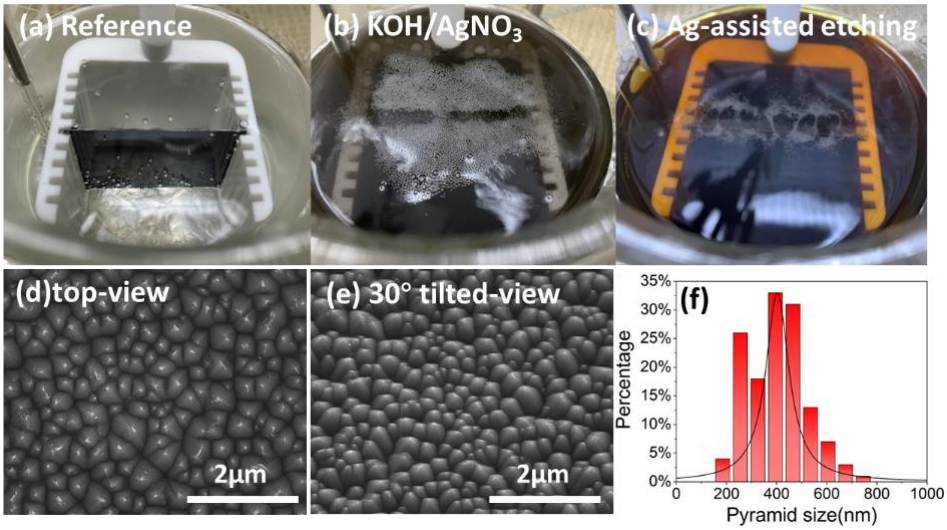

Figure. 3.11. Digital photographs showing the (a) Reference, (b) KOH and 1.2mM $AgNO_3$ and (c) KOH, surfactant and 1.2mM $AgNO_3$ solutions with the c-Si substrates; (d) Etching rate; (e) Si nanopyramids etched with high surfactant content; (f) Size distribution of Si nanopyramids etched with triple concentration of TK81.

3.5 Application of Si nanopyramids to Si heterojunction solar cell

3.5.1 Experiment

To demonstrate the effectiveness of Si nanopyramid textures in a device, SHJ solar cells were fabricated using n-type float zone (FZ) Si wafers (1-5 Ω·cm, 280μm, <100>-oriented, Topsil). The cell structure is schematically shown in Figure 3.12 (c). Intrinsic (*i*-) and doped (*p*- and *n*-type) hydrogenated amorphous Si (a-Si:H) films were successively grown on both sides of a cleaned Si wafer by plasma-enhanced chemical vapor deposition (PECVD). After that, In_2O_3:Sn (ITO) and Ag electrodes were formed by means of magnetron sputtering with shadow masks, followed by thermal annealing at 160°C. The device area was designated to be 1 cm^2. Si:H and nc-Si:H layers were successively deposited on the both sides of the wafers by means of parallel-plate plasma-enhanced chemical vapor deposition (PECVD) operated at a radio frequency (RF) of 13.56 MHz using SiH4, H2, B2H6, and PH3 as source gases. Two-step growth of (i)a-Si:H was applied

at both the front and the rear surfaces for better surface passivation. The detailed growth conditions for the (p)a-Si:H and (p)nc-Si:H layers are shown in Table 1 . Prior to the growth of (p)nc-Si:H layers, a CO_2 plasma treatment was applied to the (i)a-Si:H surface for 30 s to promote an immediate crystalline nucleation at the interface.[38] After the PECVD process, In2O3:Sn (ITO) films and Ag electrodes were formed on both sides of the precursor by means of magnetron sputtering with shadow masks at room temperature. The cell area was designed to be 4 cm^2 (18 × 24 mm^2). The front grid was composed of Ag fingers (≈100 µm in width) with a pitch of 1.95 mm, resulting a Ag coverage of ≈5%. Thermal annealing was carried out at 160 °C after the ITO depositions to recover the lifetime degradation during sputtering. [39-41]

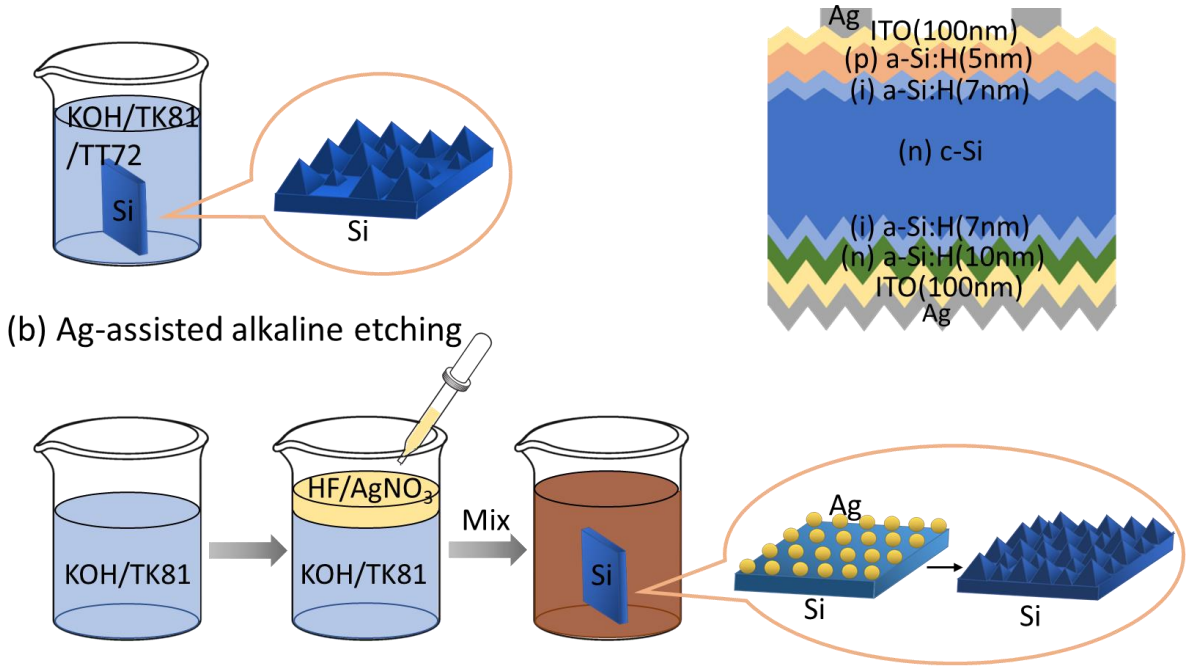

Figure 3.12. (a) Conventional alkaline etching process; (b) Ag-assisted alkaline etching process; (c) Schematic diagrams of heterojunction solar cell.

3.5.2 Result and discussion

We fabricated SHJ solar cells using the textured Si wafers prepared by our Ag-assisted alkaline etching process to verify its adaptability to solar cell devices. Figure 3.13

summarizes the photovoltaic parameters of the SHJ solar cells fabricated in this work generated from I-V curve. For each texturing condition, 7 small-area SHJ cells were fabricated and characterized. It can be seen in Figure 3.13 (a) that J_{SC} increases gradually as the ratio of $AgNO_3$ increases, which shows an obvious enhancement from 37.9 to 38.4 mA/cm^2. This result is consistent with the reflectivity results of the Si textures, which are awing to the greatly enhanced light absorption leading to the increase of the current density. In contrast, the V_{OC} and the FF are less sensitive to the surface textures as shown in Figure 3.13 (b) and (c), respectively, although a slight but marginal V_{OC} drop is observed for the smallest texture. This result indicates that Si surface with nanopyramids can be well passivated with the intrinsic a-Si:H layer, and the effect of process-induced metal (Ag) contamination of Si wafers is negligible in the device level. Accordingly, the average conversion efficiency is improved by using the nanopyramid texture as shown in Figure 3.13 (d), with the highest conversion efficiency of 21.91% and FF of 0.8.

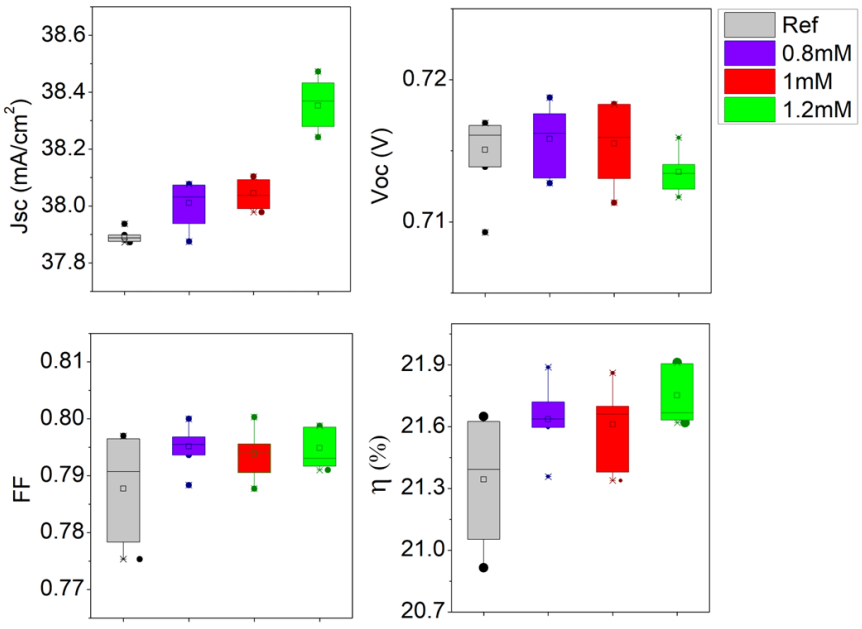

Figure 3.13. Solar cell efficiency and J–V parameters of the c-Si SHJ solar cells employing Si micro-pyramid texture and Si nanopyramid texture fabricated by Ag-assisted alkaline etching method.

Figure 3.14 shows the EQE and the reflectance spectra of the solar cells. The J_{SC} gain by applying the nanopyramid texture originates from the EQE improvements in the ranges of 400-600 nm and 800-1000 nm which coincide with the reduction in the reflectance in the same wavelength region. Therefore, the J_{SC} gain is attributed to the improved light in-coupling as well as the light trapping effect by using the nanopyramids. Note that the solar cell treated with the 0.8 mM $AgNO_3$ exhibits the highest reflectance, while its J_{SC} is comparable to that of the reference cell. This is probably caused by the thinner p-i a-Si:H layers thickness on the front side of the solar cell treated with the 0.8 mM $AgNO_3$ due to the micron-scale texture, resulting in increased light absorption at the Si substrate portion compared to the reference cell. From these results, the Si nanopyramids fabricated by the Ag-assisted alkaline etching method enables to achieve high-efficiency Si solar cells with the smaller texture size (0.5–1 µm), showing a potential for being applied to thin Si solar cells and perovskite/Si tandem cells.

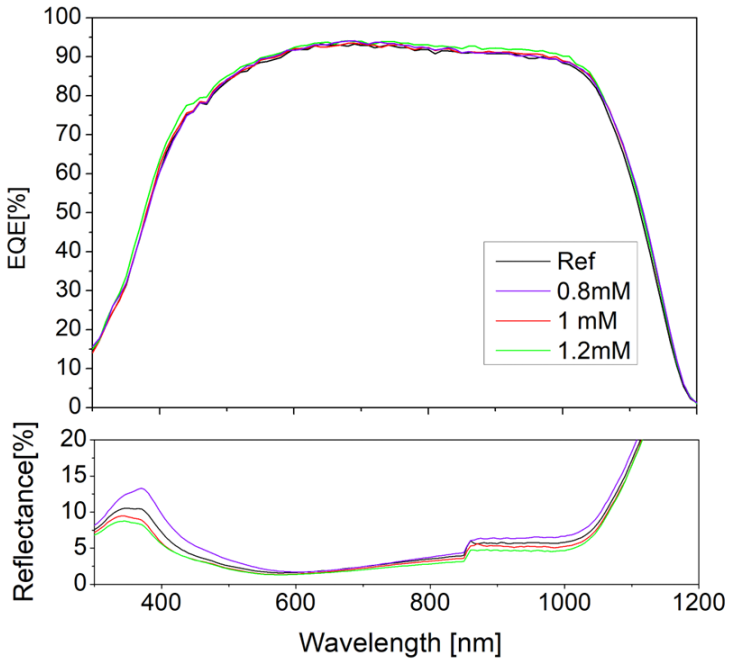

Figure 3.14. EQE spectra of the c-Si SHJ solar cells employing Si micro-pyramid texture and Si nanopyramid texture fabricated by Ag-assisted alkaline etching method.

3.6 Conclusion

In conclusion, we proposed a simple one-step chemical etching methodology using Ag-containing alkaline solution for controlling the size of Si pyramids. Nanopyramid textures with an average size of ~500 nm have been successfully formed on the Si surface with a narrow size distribution. SHJ solar cells with Si nanopyramids fabricated by this method showed higher cell performance than those with the conventional micropyramids, exhibiting an enhanced J_{SC} and conversion efficiency. The nanopyramids obtained by our method feature regularly shaped tetrahedral structures with a narrow size distribution, which results in an enhanced light in-coupling and light trapping capabilities compared with Si micropyramids fabricated by the conventional alkaline etching. The etching margin of Si nanopyramids is also reduced by half. The mechanism of the etching process can be explained by the equilibrium reaction of $AgNO_3$ and KOH in the solution. Under proper conditions, Ag NPs are continuously generated on the Si surface during the etching process, acting as efficient etching masks as well as promoting the detachment of fine H_2 bubbles from the Si surface. As a result, dense nucleation sites and uniform chemical reaction over the Si surface are realized, and nanoscale Si pyramid textures with a narrow size distribution can be formed with a minimal etching margin. These features of Si nanopyramids are promising for applications such as thin Si solar cells, advanced screen-printed metallization and perovskite/Si tandem solar cells.

References

[1] T. Saga, NPG Asia Mater. 2020, 2, 96.

[2] MK. Basher, MK. Hossain, MAR. Akand, Optik 2019, 176, 93.

[3] SE. Han, G. Che, Nano Lett. 2010, 10, 4692.

[4] V. H. Nguyen, A. Novikov, M. Shaleev, D. Yurasov, M. Semma, K. Gotoh, Y. Kurokawa, N. Usami. Mater Sci Semicond Process 2020, 114, 105065.

[5] CC. Lin, YJ. Chuang, WH. Sun, C. Cheng, YT. Chen, ZL. Chen, CH. Chien, FH. Ko, Microelectron Eng 2015, 145, 128.

[6] S. Wang, B. D. Weil, Y. Li, K. X. Wang, E. Garnett, S. Fan, Y. Cuiet, Nano Lett. 2013, 13, 4393.

[7] H. Sai, T. Oku, Y. Sato, M. Tanabe, T. Matsui, K. Matsubara, Prog Photovolt 2019, 12, 1061.

[8] S. Saha, MM. Hilali, EU. Onyegam, D. Sarkar, D. Jawarani, RA. Rao, L. Mathew, RS. Smith, D. Xu, UK. Das, B. Sopori, SK. Banerjee, Appl. Phys. Lett. 2013, 102, 163904.

[9] S. Wang, BD. Weil, Y. Li, KX. Wang, E. Garnett, S. Fan, Y. Cui, Nano Lett. 2013, 13, 4393.

[10] P. Yoon, H. Chung, H. Song, JH. Seo, S. Shin, Appl. Therm. Eng. 2015, 90, 559.

[11] M. Ju, K. Mallem, S. Dutta, N. Balaji, D. Oh, EC. Cho, YH.Choa, Y. Kima,J. Yi, Mater Sci Semicond Process 2018, 85, 68.

[12] F. Sahli, J. Werner, BA. Kamino, M. Bräuninger, R. Monnard, BP. Salomon, L. Barraud, L. Ding, JJD. Leon, D. Sacchetto, G. Cattaneo, M. Despeisse, M. Boccard, S. Nicolay, Q. Jeangros, B. Niesen & C. Ballif, Nat. Mater. 2018, 17, 820.

[13] M.Yamaguchi, F. Dimroth, JF. Geisz, NJ. Ekins-Daukes. J. Appl. Phys. 2021. 129, 240901.

[14] R. Heinke, M. Ehrhardt, P. Lorenz, K. Zimmer. Appl. Surf. Sci. 2021, 6, 100169.

[15] AP. Amalathas, MM. Alkaisi, J. Thirumalai. In Micro/Nanolithography: A Heuristic Aspect on the Enduring Technology. IntechOpen, 2018.

[16] Y. Ota, D. Yurasov, A. Novikov, M. Shaleev, K. Gotoh, Y. Kurokawa, N. Usami. J. Appl. Phys. 2019, 58, 045505.

[17] S. Zhong, W. Wang, Y. Zhuang, Z. Huang, W. Shen. Adv. Funct. Mater. 2016, 26, 4768-4777.

[18] S. Zhong, W. Wang, M. Tan, Y. Zhuang, W. Shen, Adv. Sci. 2017, 4, 1700200.

[19] A. Alasfour, JY. Zhengshan, W, Weigand, D. Quispe, ZC. Holman. Sol. Energy Mater. Sol. Cells 2020, 218, 110761.

[20] CT. Nguyen, K. Koyama, HTC. Tu, K. Ohdaira, H. Matsumura. J. Mater. Res. 2018, 33, 1515.

[21] Y. Hou, E. Aydin, M. De Bastiani, C. Xiao, F.H. Isikgor, D. J. Xue, B. Chen, H. Chen, B. Bahrami, A.H. Chowdhury, A. Johnston, S. Baek, Z. Huang, M. Wei, Y. Dong, J. Troughton, R. Jalmood, A.J. Mirabelli, T.G. Allen, E.V. Kerschaver, M.I. Saidaminov, D. Baran, Q. Qiao, K. Zhu, S.D. Wolf, E.H. Sargent. Science 2020, 367,1135.

[22] I. Zubel, I. Barycka, K. Kotowska, M. Kramkowska. Sens. Actuators A: Phys. 2001, 87, 163.
[23] AM. Al-Husseini, B. Lahlouh. Bull. Mater. Sci. 2019, 42, 1.
[24] MK. Basher, M. Khalid Hossain, M. Jalal Uddin, MAR. Akand, KM. Shorowordi. Optik 2018, 172, 801.
[25] J. Wang, F. Zhong, H. Liu, L. Zhao, W. Wang, X. Xu, Y. Zhang. Sol Energy 2021, 221, 114.
[26] Fan Y, Han P, Liang P, et al. Differences in etching characteristics of TMAH and KOH on preparing inverted pyramids for silicon solar cells[J]. Applied Surface Science, 2013, 264: 761-766.
[27] Haiss W, Raisch P, Bitsch L, et al. Surface termination and hydrogen bubble adhesion on Si (1 0 0) surfaces during anisotropic dissolution in aqueous KOH[J]. Journal of Electroanalytical Chemistry, 2006, 597(1): 1-12.
[28] W. Chen, Y. Liu, Li. Yang, J. Wu, Q. Chen, Y. Zhao, Y. Wang, X. Du. Sci. Rep. 2018, 8, 1.
[29] CR. Yang, PY. Chen, YC. Chiou, RT. Lee, Sens. Actuators A: Phys. 2005, 119, 263.
[30] JM. Kim, YK. Kim. Sol. Energy Mater. Sol. Cells 2004, 81, 239.
[31] AK. Chu, J.S. Wang, ZY. Tsai, CK. Lee. Sol. Energy Mater. Sol. Cells 2009, 93, 1276.
[32] T. Ohmi, Appl. Surf. Sci. 1997, 44, 121.
[33] K. Peng, H. Fang, J. Hu, Y. Wu, J. Zhu, Y. Yan, and S. T. Lee, Chem. - A Eur. J. 2006, 12, 7942.
[34] X. Li, PW. Bohn. Appl. Phys. Lett 2000, 77, 2572.
[35] B. Chen, J.Y. Zhengshan, S. Manzoor, S. Wang, W. Weigand, Z. Yu, G. Yang, Z. Ni, X. Dai, Z.C. Holman, J. Huang. Joule 2020, 4, 850.
[36] P. Tockhorn, J. Sutter, A. Cruz, P. Wagner, K. Jäger, D. Yoo, F. Lang, M. Grischek, B. Li, A. Al-Ashouri, E. Köhnen, M. Stolterfoht, D. Neher, R. Schlatmann, B. Rech, B. Stannowski, S. Albrecht, C. Becker. Research Square 2022.
[37] G. Lin, Z. Gao, T. Gao, Y. Chen, Q. Geng, Y. Li, L. Chen, M. Li. J Materiomics 2021, 7, 1161.
[38] L. Mazzarella, S. Kirner, O. Gabriel, S. S. Schmidt, L. Korte, B. Stannowski, B. Rech, R. Schlatmann, Phys. Status Solidi 2017, 214, 1532958.
[39] H. Sai, H. Umishio, T. Matsui. Solar RRL 2021, 5, 2100634. [40] H. Sai, HJ. Hsu, PW. Chen, PL. Chen, T. Matsui. Phys. Status Solidi A 2021, 218, 2000743.
[40] H. Sai, PW. Chen, HJ. Hsu, T. Matsui, S. Nunomura, K. Matsubara. J. Appl. Phys. 2018, 124, 103102.

4. Si nano-pyramid structure and application in Perovskite/Si tandem solar cell

4.1 Introduction

4.1.1 Background

4.1.1.1 Perovskite/Si tandem solar cell

Currently, crystalline Si (Si) photovoltaic (PV) technology accounts for about 95% of the worldwide PV market due to the abundance of Si, long-term reliability, relatively high power conversion efficiency (PCE) and the continuous reduction in the production cost.[1] Thus, Si-PV is expected to provide an economical and sustainable solution as a major renewable energy resource towards a decarbonized society. Meanwhile, the PCE of the state-of-the-art Si solar cell (>26%) [2,3] is approaching its single-junction efficiency limit (29.4%) [4,5] as a result of the continuous research in recent years. Stacking a wide bandgap material on top of the Si subcell to form a tandem device architecture is one of the routes to overcome the fundamental efficiency limitations of single-junction Si devices. Lead halide perovskites [6,7] are a promising class of materials for tandem integration with Si in terms of bandgap matching and tunability (1.5−2.3 eV), high efficiency (25.7% in single-junction device [8,9]) and potential for low-cost production using solution-based deposition processes. Figure 4.1 (a) shows the basic structure of a perovskite/c-Si tandem cell, by stacking a wide bandgap perovskite cell on a Si cell, Increased efficiencies is able to realzied without adding substantial cost by achieving spectral distributed absorption (Figure 4.1 (b)).

Recently, a PCE of 33.2% has been achieved experimentally in a perovskite/Si tandem solar cell [10], which far exceeds the limit of Si solar cells and is a great leap towards the realization of high-energy density PV.

Amongst various tandem design architectures (i.e., two-, three- and four-terminal devices)[11,12], the two-terminal tandem solar cell - a monolithic series connection of two subcells via a recombination junction - is the most compatible architecture for the current Si PV technology. In two-terminal architecture, most of the currently reported

perovskite/Si tandems are based on Si bottom cells featuring a front-planar rear-textured structure to ensure the growth of high-quality perovskite layers by solution-based processes such as a spin coating method. Besides, an indium-tin-oxide (ITO) layer is commonly used as a recombination junction layer for electrical interconnection between top and bottom cells, which often causes a high interfacial reflection and thus an optical loss in the bottom cell.[13,14] To mitigate the interfacial reflection, an optical coupler based on ITO/hydrogenated nanocrystalline Si oxide (nc-SiO_x:H) (~100 nm) bilayer design was proposed [14-16], leading to a PCE of 29.7%.[17] However, depositing such a thick nc-SiO_x:H layer is a challenge in the industrial production due to its low deposition rate. The use of an ITO interlayer is also an issue because it requires an additional physical vapor deposition (PVD) process as well as involving the use of a scarce metal (i.e., indium).

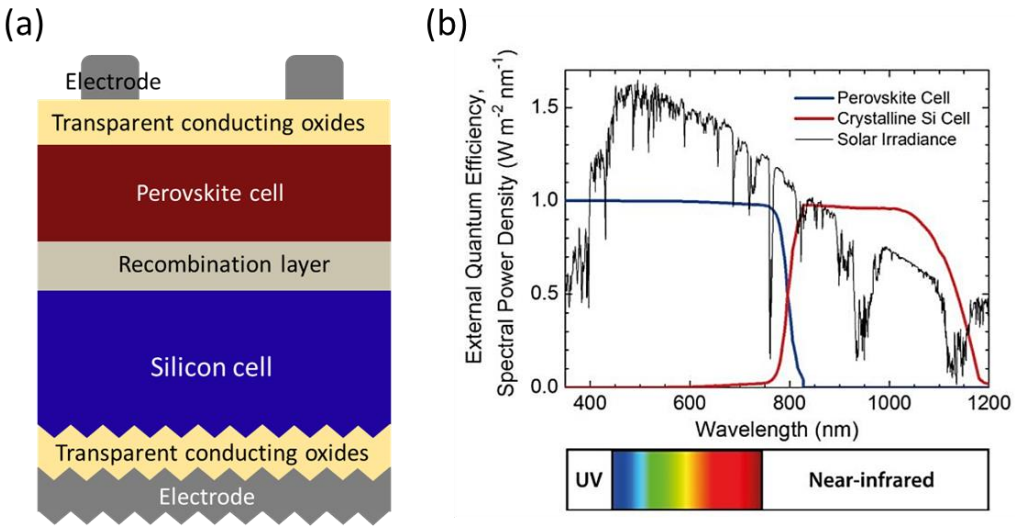

Figure 4.1. (a) Schematic diagram of basic structure of perovskite/Si tandem solar cell; (b) Absorption spectrum of both perovskite and silicon sub-cells(Perovskite Cells for Tandem Applications https://www.epfl.ch/labs/pvlab/research/page-124775-en-html/).

4.1.1.2 Double-side Si nano texture in perovskite/Si tandem solar cell

In order to further improve the utilization of the incident light of tandem solar cells without sacrificing the production cost, fabrication of tandem devices made with double-side textured Si wafers has become a compelling research topic.[18-26] Figure 4.2 shows the schematic diagram of perovskite/Si tandem solar cell with double-side textured Si bottome cell. There are two approaches of implementing double-sided Si textures in tandem devices; one is a micron-sized Si pyramid (micro-pyramid) texture prepared by the standard anisotropic etching in alkaline solutions. In this case, the perovskite layer needs to be deposited by vacuum processes such as co-evaporation to provide a conformal perovskite layer deposition over the micron-sized pyramid surface, though vacuum equipment is costly in general.[19-22] Alternatively, the perovskite layer can be formed on such a micro-pyramid texture by solution processes including spin coating[23] and blade coating[24] if the perovskite layer is sufficiently thick (typically greater than 1 μm), whereas this might suffer from a trade-off between the absorber thickness and the carrier diffusion length. The other approach is to use nanoscale Si textures with a feature size as small as 1 μm, which is compatible with solution-based processes.[25-27] Tockhorn et al. demonstrated a PCE of 29.8% in a perovskite/Si tandem cell by introducing sinusoidal periodic textures with a size around 500 nm fabricated by nanoimprint lithography.[26] Ying et al. presented a 28.2% efficient perovskite/Si tandem solar cell by using a very small sized Si texture (~<100 nm) fabricated by the metal-assisted etching technique followed by the surface reconstruction process.[27] However, these nanoscale texturing techniques are applied only for the front side Si wafer while the rear side micro-pyramid texture needs to be prepared in a separate process. Thus, an asymmetric Si texturing approach as such might not be suitable for industrial-scale production.

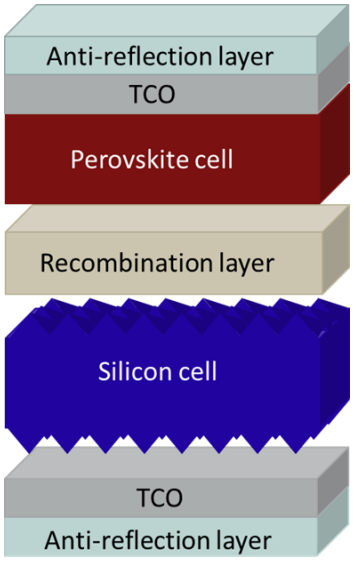

Figure 4.2. The schematic diagram of perovskite/Si tandem solar cell with double-side textured Si wafer.

4.1.2 Purpose

Given the situation mentioned above, an Si pyramid texture of less than 1 μm which can be fabricated by the simple alkaline etching process is highly desired to make Si bottom cell compatible with the subsequent solution-based perovskite deposition processes, which is economically viable, and is attractive for large-scale industrial production. However, there are limited reports on the practical applications of the solution processed Si nanostructures in perovskite/Si tandem solar cells.[26] In particular, there is still a lack of detailed research regarding the actual impact of the size and morphology of nanoscale Si textures on the interface properties and performance of perovskite/Si tandem solar cells.

Recently, we have developed an original methodology to fabricate Si nanopyramid texture using an Ag-assisted one-step etching process.[28] This allowed us to vary the average size of the Si pyramid texture from >1 μm down to ~500 nm by adjusting the concentration of $AgNO_3$ in the etching solution. The both-side textured Si wafers were subjected to our standard Si heterojunction (SHJ) cell process and an improved solar cell

performance was demonstrated using the nanopyramid texture with an average size of ~600 nm. In this work, we extend our methodology to apply the nanostructured SHJ bottom cells to perovskite/Si tandem solar cells that feature an interlayer-free design and all spin-coated top cells. The results show that the best tandem cell performance is obtained when the Si pyramid size is around 400-500 nm, showing a significant improvement in the bottom cell response compared with the devices with front-planar rear-textured Si bottom cells. This technology enables both the uniform deposition of perovskite top cell component layers by solution processing and the significant improvement in light absorption of tandem solar cells without implementing the complex and thick optical multilayers at the top/bottom cell interface, which is expected to provide a guidance for the interface design of double-sided textured Si for industrial perovskite/Si tandem solar cells.

4.2 Experiment

4.2.1 Fabrication of Si nanopyramid texture

Figure 4.3 shows the fabrication flow of perovskite/Si tandem cells. Mirror-polished *n*-type floating zone (FZ)-grown monocrystalline Si wafers (1-5 Ω· cm, <100>-oriented) with a thickness of ~280 μm were used for the Si bottom cells. After cleaning processes with acetone and deionized water, the planar Si wafer was textured by dipping in mixed solution containing the following components: KOH, surfactant (Hayashi Pure Chemicals Ind. Ltd., Pure Etch TK81), $AgNO_3$ solution of HF (46%-48%): $AgNO_3$: DI water (10 ml: 0.1 g: 40 ml). For the conventional reference micro-pyramid textures, a planar Si wafer was textured by the mixed solution using organic masking material (Hayashi Pure Chemicals Ind. Ltd., Pure Etch TT72,) instead of $AgNO_3$ solution. We fabricated differently sized Si nanopyramid textures under three surfactant (Hayashi Pure Chemical Ind., Ltd., TK81) concentrations of 50%, 30% and 10%. The $AgNO_3$ concentrations of 1.0 or 1.2 mM was added in the solution (Table 4.1). After etching, the samples were immersed in HNO_3 solution to remove the residual Ag. The surface morphology of the Si substrates was

characterized by field emission SEM (Hitachi High-Tech S-4300 SEM). In this study, we measured the bottom width of over 150 pyramids and used their average value to represent the pyramid size of each texture. To characterize the optical performance, reflectance of the samples was measured by UV-VIS-NIR spectrophotometer (PerkinElmer, Lambda 950) equipped with an integrating sphere (Lab-sphere, 150 mm RSA ASSY).

Table 4.1. Five groups of different etching conditions of Ag-assisted alkaline etching for size control of Si nanopyramids.

	A	B	C	D	E
TK81 concentration	50%	30%	10%	10%	10%
AgNO3 concentration	1.2mM	1.2mM	1.2mM	1.0mM	1.0mM
Temperature	70℃	70℃	70℃	70℃	80℃
Time	15min	5min	15min	15min	15min

4.2.2 Fabrication of the Si bottom cells

SHJ bottom cells were fabricated using the same Si wafers with thickness of ~280μm. Si nanopyramid textures with different sizes were formed on both sides of the Si wafer by the Ag-assisted alkaline etching process described above. The Si wafers were subjected to our standard cleaning process.[29] No special cleaning was done after the Ag-assisted alkaline etching process.After cleaning the wafers, *i*-a-Si:H/*n*-a-Si:H and *i*-a-Si:H/*p*-a−Si:H layers were deposited on the rear and front sides of the Si wafer, respectively, in a multichamber PECVD system.[30] In this study, we deposited phosphorous doped *n*-nc-Si:H as a recombination junction layer on top of the *p*-a-Si:H layer.[32] Prior to depositing *n*-nc-Si:H, a CO_2 plasma treatment was carried out on the underlying *p*-a-Si:H layer for 10 s to facilitate the nucleation of the nc-Si:H growth.[33] Then, ITO−Ag stacked layers were deposited on the rear side of the wafer without a mask by magnetron sputtering.

4.2.3 Fabrication of the perovskite top cells

3min of UV-ozone pre-treatment was implemented to remove the organic pollutants on front surface of SHJ bottom cells. 300μL of SnO_2 nanoparticle colloidal solution(diluted in deionized water) was spin coated on the front surface of SHJ bottom cells with 2000 rpm for 30 s, and then annealled at 100 °C for 1 h in dry air. UV-ozone treatment was implemrnted for substreats again for 10 min. For the preparation of $Rb_{0.05}(FA_{0.83}MA_{0.17})_{0.95}PbI_{0.83}Br_{0.17}$ perovskite[34] solution, 1.26 M formamidinium iodide (FAI), 1.4 M PbI_2, 0.25 M $PbBr_2$, 0.09 M RbI, and 0.25 M methylammonium bromide (MABr), was dissolved in mixed solution of dimethylformamide (DMF) and dimethylsulfoxide (DMSO) to the ratio of 4:1 (V:V). Next, shaking the perovskite precursor solution for about 20 hours and then filtering it with a 0.45 μm pore size PTFE filter at room temperature immediately before utilization. 40 μL of the perovskite precursor solution was dropped onto the substrate, and two different programs are used for the spin-coating: 1300 rpm for 5 s with 200 rpm/s ramp followed by 5000 rpm for 30 s with 2000 rpm/s ramp. During the spin-coating process, 300 μL of anhydrous anisole was also dropped onto the rotating substrate at the time of the 30s, and then the substrate was annealed at 110 °C for 15 min. The HTL soluton was composed of 69 mg of spiro-MeOTAD and 800 μL of chlorobenzene. 14 μL of Li-TFSI (574 mg/mL in acetonitrile) and 27.1 μL of 4-tertbutylpyridine were mixed into the spiro-MeOTAD solution for doping, and the solution was shaken for 3 h at room temperature before utilization. Then spin-coating of 50 μL doped spiro-MeOTAD solution onto the substrate with 4000 rpm for 30 s. At last, Substrates were putted in dry air (<1% relative humidity) for 12h. Next, ITO (In_2O_3/SnO_2 90/10 wt.% in target) with a thinknes of 130nm was formed in an $Ar-O_2$ (O_2: 0.5%) gas mixture by magnetron rf-sputtering system. It is worth mentioning that a long target-substate distance of 250 mm was used to limit the sputter-induced damage on perovskite top cell. The sheet resistivity of the ITO layer was ~ 40 Ω/sq. Then, Ag (250 nm) finger contacts capped by ITO (20 nm) thin layers were sputtered in the same system. The resulting device area was ~1 cm^2. The devices were

then annealed at 50 °C for 1 h in N_2 atmosphere. Some of the devices were coated with a 110 nm-thick MgF_2 AR layer using a vacuum evaporator. The finished devices were left in vacuum for about 1 week prior to measurement. The thicknesses of ITO and MgF_2 layers were roughly optimized using an optical simulator (OPAL 2) for maximizing the J_{SC} in tandem devices.[35] In optical simulation, the optical constants of each layer were taken from the simulation database. The finiehed structure of the double-side textured perovskite/Si tandem cell is shown in 4.4 (a). For characterization, A shadow black mask with fixed illumination area of 1.0 cm^2 was used which includes the Ag finger but excludes the Ag busbar (see Fig. 4.4(b)). A Keithley 2400 source meter was used for the measurement of the solar cells' J–V parameters, which were recorded in both forward and reverse scan directions in the voltage range from −0.1 V to 1.9 V. The scan rate was 0.15 V/s. External quantum efficiency (EQE) spectra were measured with an EQE setup (Bunkou Keiki, CEP-25BXS). For tandem devices, red (λ>750 nm) or blue (λ<650 nm) light bias was applied using optical filters to saturate photocurrent of the unmeasured subcell. No electrical bias was applied. The cross-section of the devices was captured by field-emission SEM at AIST and by HAADF-STEM (JEOL JRM-ARM200F) at JFE Techno-Research Corporation.

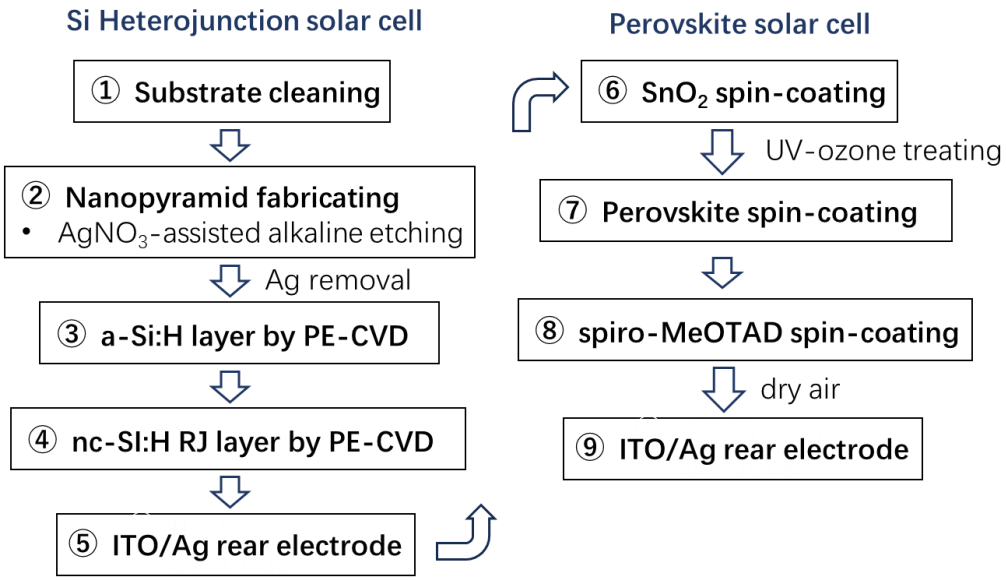

Figure 4.3. Flow chart of fabrication process of Si heterojunction bottom cell and perovskite top cell.

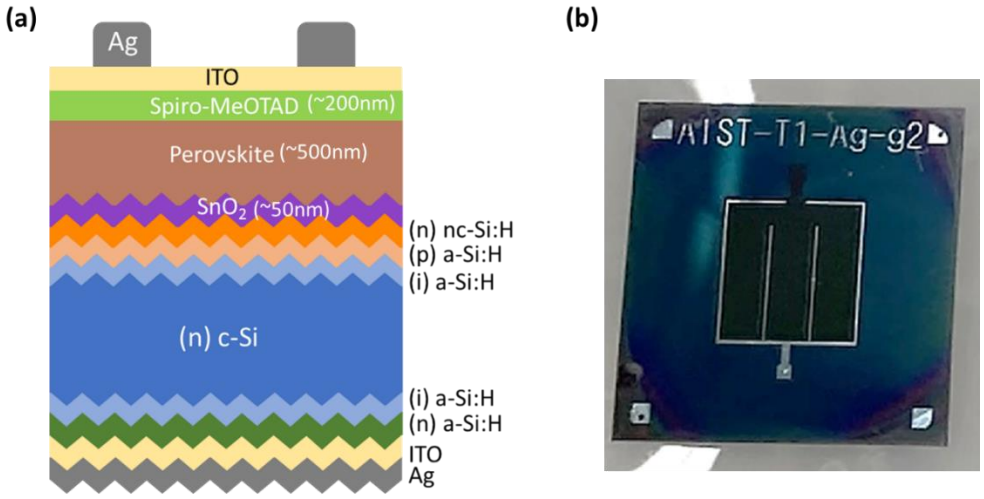

Figure 4.4. (a)The schematic diagram of perovskite/Si tandem solar cell with double-side Si nanopyramid textured Si wafer. (b) A photo of a tandem solar cell fabricated on a 25×25 mm^2 Si substrate. The active cell area is 1.21 cm^2 including Ag fingers and busbar, while the illumination area for J-V measurement was defined to be 1.0 cm^2 using a black shadow mask (not shown).

4.3 Result and discussion

4.3.1 Fabrication of Si nanopyramid texture and SHJ bottom cell

We used an Ag-assisted etching process to fabricate Si nanopyramid textures.[36] This process allows us to control the size of Si pyramid texture at the nanoscale by adjusting the concentration of $AgNO_3$ in the alkaline solution. We fabricated differently sized Si nanopyramid textures under three surfactant (Hayashi Pure Chemical Ind., Ltd., TK81) concentrations of 50%, 30% and 10%. The $AgNO_3$ concentrations of 1.0 or 1.2 mM was added in the solution. As shown in the top-view and the corresponding cross-sectional scanning electron microscope (SEM) images of the Si pyramids in Fig. 4.5 (a), the average size of the Si pyramids decreases from ~900 to ~400 nm with increasing TK81 concentration. A conventional micro-pyramid texture was also prepared under the standard etching condition using KOH, TK81 and an additional surfactant TT72.[36] Here we term these samples and corresponding devices by referring to the average size of each texture (A_{420nm}, B_{530nm}, C_{680nm}, D_{950nm}, and E_{1050nm}). It is noted that the homogeneity of the size distribution is improved, as shown in the corresponding histogram in Fig. 4.4(b), as the texture size becomes smaller.

The following is a brief explanation of the etching mechanism of the Ag-assisted alkaline etching method used in this study. First, the Si surface is plated with Ag nanoparticles which act as a uniform and dense etching mask. At the same time, anisotropic etching of Si occurs at the Ag-Si contact site, forming an Si nanopyramid texture. H_2 bubbles formed during etching are preferentially generated on the Ag particle site due to its high electronegativity, leaving the Si-etchant contact area and enhancing the etching rate. Such an intensive reaction and generation of H_2 bubbles are controlled effectively by adding TK81. The TK81 acts as a surfactant to promote the detachment of H_2 bubbles and also suppress the excess reaction. From our observation, we conclude that the combination of fine and dense masking and an appropriate etching rate is crucial to obtain the precise size control of Si pyramids with good uniformity. It should be mentioned that the Ag consumption for Si nanotexturing used in this work is estimated

to be 8 mg/W, which is lower than that for the Ag screen printing (25 mg/W).[37] We expect that this amount can be further reduced by process optimization. In addition, Ag could be replaced with other base metals like Cu and Ni, which are known to be applicable to metal-assisted Si etching.

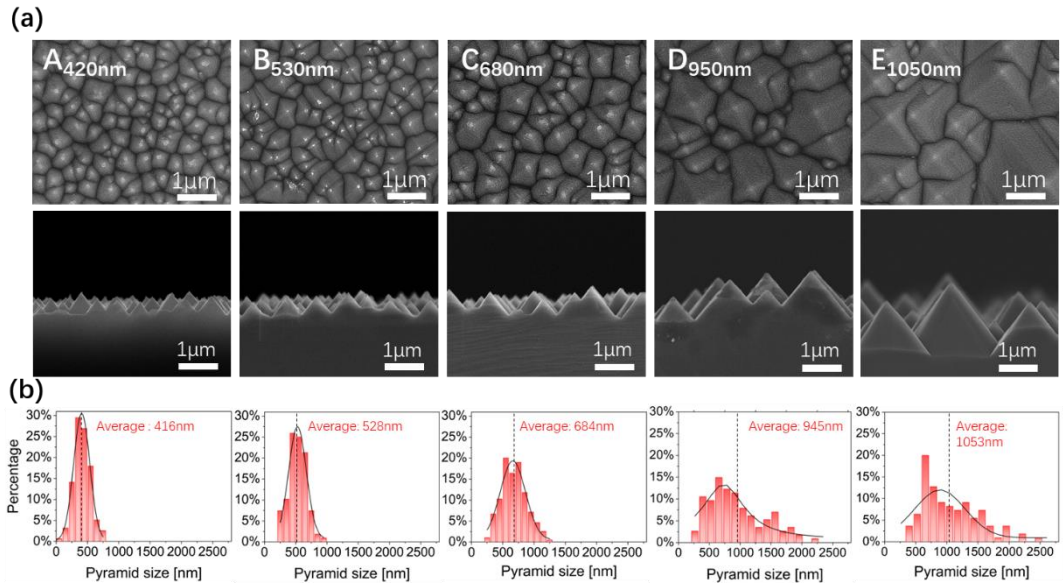

Fig 4.5. (a) Top-view and corresponding cross-sectional SEM images of the four different textured Si wafers processed with Ag-assisted alkaline etching under different conditions (A_{420nm}: TK81=50%, $AgNO_3$=1.2 mM, B_{530nm}: TK81=30%, $AgNO_3$=1.2 mM, C_{680nm}: TK81=10%, $AgNO_3$=1.2 mM, D_{950nm}: TK81=10%, $AgNO_3$=1.0 mM). For comparison, an SEM image of a reference Si texture is shown (E_{1050nm}: TK81=10%, $AgNO_3$=0 mM, TT72=8%); (b) Histogram of the lateral size distribution of Si textures A_{420nm}, B_{530nm}, C_{680nm}, D_{950nm}, and E_{1050nm}.

The size of the pyramid texture influences the spectral reflectance (*R*) of the Si wafer, as shown in Fig. 4.6(a). As the texture size decreases, the *R* in the wavelengths of 400-1000 nm firstly decreases slightly and then increases. It is noted that nanopyramid textures C_{680nm} and D_{950nm} outperform the standard micro-pyramid texture E_{1050nm} in terms of the absorbance of the Si wafer (1-*R*) among the samples investigated, This is in good

agreement with our previous work and attributed to the improved light in-coupling effect by the sharp nanopyramids with uniform size distribution.[27] For smaller pyramids (A_{420nm} and B_{530nm}), the *R* starts to increase when the wavelength is greater than the average size of the Si pyramids. This is because light in-coupling by random pyramids is based on ray optics and works well only if the size of the pyramids is sufficiently large with respect to the wavelength of the incident light. If the size of the pyramids becomes smaller than the wavelength of the light, the light in-coupling efficiency therefore decreases significantly which results in a poor light trapping effect and less absorption within the Si wafer.[38] In addition, the light trapping effect becomes less efficient with the decrease in texture size, resulting in the blue shift of the absorption edge at ~1100 nm as seen in Fig. 4.6(a). Nevertheless, the *R* of the samples A_{420nm} and B_{530nm} is still much lower than that of the both side planar Si as well as the front-planar rear-textured Si.

To investigate the influence of texture size on the spectral sensitivity of Si solar cells, external quantum efficiency (EQE) measurement was performed for the SHJ bottom cells without forming any top cell component layers. Instead, an ITO layer and an Ag-grid were deposited on top of the bottom cell precursors that have *n*-Si absorber sandwiched by undoped/doped hydrogenated amorphous Si (a-Si:H) and a following doped hydrogenated nanocrystalline Si (nc-Si:H) layer on the front side, forming a test cell structure of Ag-grid/ITO/*n*-nc-Si:H/*p*-a-Si:H/*i*-a-Si:H/*n*-Si/*i*-a-Si:H/*n*-a-Si:H/ITO/Ag.[39] Figure 4.6(b) shows the EQE curves of the SHJ solar cells with differently textured Si wafers. The solar cell parameters of the representative devices (A_{420nm}, E_{1050nm}, reference) are given in Table 4.2. It is evident that the both sided textured Si provides a much higher spectral response in the wavelengths of 600-1200 nm compared with that of the reference front-planar rear-textured Si because of the reduced reflection. For both sided textured Si bottom cells, in contrast to the reflectance spectra, the variation in the EQE spectra is less pronounced, regardless of the size of the pyramid textures. This is because the top ITO layer works as an antireflection (AR) layer which suppresses the variation of

the optical properties in these wafers. However, a slight redshift of the EQE curve can be seen for wavelengths of >1050 nm with an increase in the size of the pyramid texture, indicating that the light trapping effect near the band gap wavelength is enhanced by enlarging the pyramid size. On the other hand, the EQE in the short wavelengths around 300-650 nm decreases with decreasing the texture size, which originates from the absorption loss due to the thickening of the component layers (a-Si:H, nc-Si:H, ITO) because the deposition time of these layers was not adjusted with respect to the texture size.

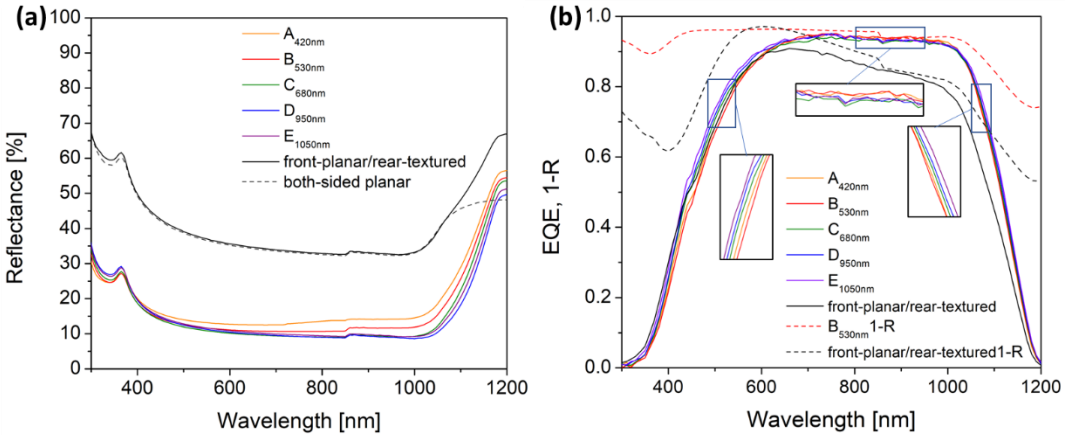

Fig. 4.6. (a) Spectral reflectance of the bare Si wafers with differently sized pyramid textures fabricated by Ag-assisted alkaline etching (A_{420nm}, B_{530nm}, C_{680nm}, D_{950nm}) and by the conventional alkaline etching (E_{1050nm}). For comparison, the reflectance spectra of the double-sided planar Si and front-planar rear-textured Si are shown. (b) EQE spectra of the SHJ single-junction solar cells employing Si wafers used for the reflectance measurement in (a) except double-sided planar Si. For clarity, 1-R spectra are shown for the representative solar cells (B_{530nm} and reference). Note that the thickness of the front component layers (*ip*-a-Si:H, *n*-nc-Si:H, ITO) for the double-side textured cells were not optimized.

Table 4.2. J-V parameters of SHJ single-junction solar cells with typical three Si wafers used for tandem solar cells. Note that the devices contain 25 nm-thick *n*-nc-Si:H recombination junction layer between front ITO and *p*-a-Si:H layers. For device A_{420nm}, good passivation was achieved before we lose the optimum PECVD conditioning.

Si wafer	J_{SC} (mA cm^{-2})	V_{OC} (V)	FF	PCE (%)
Reference (front-planar rear-textured)	34.5	0.718	0.762	18.9
A_{420nm}	36.6	0.712	0.752	19.6
E_{1050nm}	37.0	0.712	0.768	20.2

4.3.2 Tandem cell performance

4.3.2.1 J-V performace

Next, we fabricated monolithic two-terminal perovskite/Si tandem solar cells using the differently textured Si bottom cells shown above. The structure of our perovskite/Si tandem solar cells is shown schematically in Fig. 4.7(a). The bottom cell was prepared in the front-junction configuration. On top of the *p*-a-Si:H hole contact layer, an *n*-nc-Si:H recombination layer was grown in situ by plasma-enhanced chemical vapor deposition (PECVD), enabling transparent conductive oxide (TCO)-free interconnection between the top and bottom cells. [32]Then, the perovskite top cell was deposited in the *n-i-p* deposition sequence starting from SnO_2 (~50 nm) as electron transport layer (ETL), perovskite as light absorber layer (500-600 nm) and doped 2,2',7,7'-Tetrakis [N,N-di(4-methoxyphenyl)amino] -9,9'-spirobifluorene (Spiro-MeOTAD) (~200 nm) as hole transport layer (HTL). The bandgap of the perovskite absorber layer used in this study is ~1.63 eV which provides reasonable current matching in the present tandem device design. These *n-i-p* stacked layers were deposited entirely by spin coating. Finally, ITO and Ag-grid front electrodes were made by sputtering through shadow masks. No buffer layer was used between Spiro-MeOTAD and ITO layers. The details of our tandem device design and fabrication process can be found elsewhere.[32] Figure 4.7(b) shows the current density-voltage (J-V) curves of the perovskite/Si tandem cells with differently textured Si bottom cells. For comparison, a tandem cell with a front-planar rear-textured

Si bottom cell was also prepared as a reference. It can be seen from the J-V curves that the solar cell performance is significantly affected by the texture size of the Si bottom cell. In particular, there is a substantial decrease in V_{OC} from 1.75 to 0.89 V with enlarging the texture size from ~500 to ~1000 nm. The anomalously high J_{SC} (>19 mA cm^{-2}) seen for devices D_{950nm} and E_{1050nm} can be attributed to both the electrical shunting through the top cell and the non-uniform perovskite layer formation on large textures as discussed below. In contrast, the V_{OC} of device B_{530nm} remains as high as that of the reference sample. The J_{SC} of device B_{530nm} is higher by 0.8 mA cm^{-2} compared to the reference cells. Overall, this results in an increase in the solar cell efficiency from 19.0 to 20.3%. Unexpectedly, device A_{420nm} exhibits poorer performance in both V_{OC} and J_{SC}. This originates from the degradation of the bottom cell rather than the decrease in the top cell performance. It was found that the a-Si:H passivation quality is strongly dependent on the PECVD conditioning particularly when being deposited on such a small-sized pyramid texture.[40] As shown in Table S1 (Supporting Information), we have attained a reasonably high performance single-junction device using the Si substrate A_{420m}. However, after making a minor change in the deposition reactor of the intrinsic a-Si:H layer, we have subsequently been unable to reproduce good quality a-Si:H passivation in our nanotextured devices. Although we have not yet found which PECVD deposition parameter is a key in passivating the nanopyramid surface like A_{420nm}, such a technical issue can be solved by the minor tuning of the deposition parameters.

4.3.2.2 Interface morphology

The dependence of the device performance on texture size can be understood by analysing the cross-sectional SEM images of these devices shown in Fig. 4.7(c). For devices A_{420nm} and B_{530nm}, it is seen that these nanopyramids allow the perovskite layer to be uniformly deposited on the textured Si surface by the spin coating method. It is also found that the top of the perovskite layers is planarized when formed by such a solution-based deposition process. which is not particularly ideal from an optical point

of view. However, an AR monolayer coating can effectively reduce the optical reflection at the top-cell surface, as shown later. On the other hand, there seems to be a local thickness non-uniformity in the SnO_2 layers, which will be evidenced by a transmission electron microscope (TEM) analysis below. For device C_{680nm}, the peak of the large pyramid almost reaches the top surface of the perovskite layer, at which the thickness of the perovskite layer is very thin (~50 nm). This might cause a local electrical shunting path, accounting for the decrease of all solar cell parameters. For devices D_{950nm} and E_{1050nm}, due to the excessive size of the pyramids, none of the constituent layers of the top cell uniformly covered the substrate. The perovskite and spiro-MeOTAD layers are punched through by some of the large pyramid peaks, which results in considerable electrical shunting and thus the photogenerated carriers of the Si bottom cell can be collected by the top electrode without carrier exchange via the recombination junction layer. Also, the average thickness of the perovskite layer becomes thinner, explaining the very high J_{SC} (~20 mA cm^{-2}) solely generated by the Si bottom cell, as shown in Fig. 4.7(b). As shown in the top-view SEM images in Fig. 4.8, it is confirmed that the density of the uncovered pyramid tip increases from D_{950nm} to E_{1050nm} while no uncovered area is identified for samples A_{420nm}, B_{530nm}, and C_{680nm}.

In Fig. 4.7(c), it can be seen that the height of the pyramids of each sample is smaller by a factor of ~0.6-0.7 compared with their average lateral size as measured by the top-view SEM images, which originates from the pyramid angle between the Si {111} facet and the Si {100} plane. Given that device B_{530nm} shows the best solar cell performance, the height of the pyramids being as small as the thickness of the perovskite layer (500 nm) and its tight size distribution are the prerequisites to benefit from texturing Si while preserving the good electrical properties of the top cell. We note that the solar cell performance of device C_{680nm}, D_{950nm} and E_{1050nm} is expected to be improved by simply thickening the perovskite layer well above the texture size. However, we note that there must be a trade-off between the thickness of the perovskite layer and the carrier diffusion length.

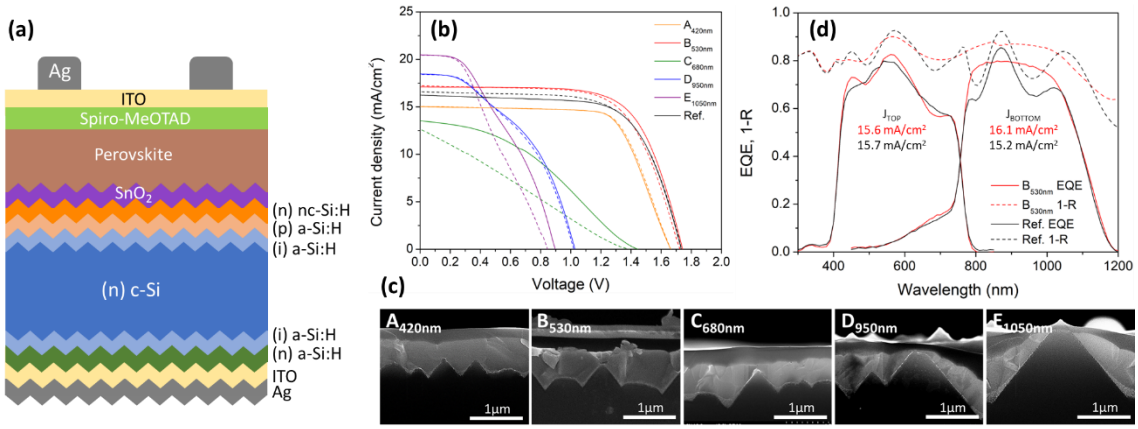

Fig. 4.7. (a) Schematic diagram of the monolithic two-terminal perovskite/Si tandem solar cells fabricated in this study. (b) Current density-voltage (J-V) curves (solid lines: forward scan, dashed lines: reverse scan) and (c) The corresponding cross-sectional SEM images of the perovskite/Si tandem cells with differently textured Si bottom cells. Note that these SEM images are taken from the samples without the front ITO layer, while the device B_{530nm} has an ITO and an MgF_2 layers on top of the spiro-MeOTAD HTL layer. (d) EQE and 1-*R* spectra of the tandem cells made with a front-planar rear-textured Si (reference) and with an optimally textured Si featuring an average size of 530 nm (B_{530nm}).

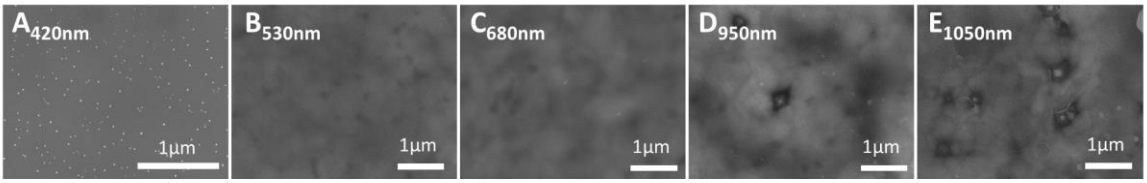

Fig. 4.8. Top-view SEM images of the perovskite/Si tandem solar cells with differently textured Si bottom cells. These SEM images were captured where no top electrode was deposited.

4.3.2.3 cell performance

Figure 4.7(d) compares the EQE spectra of the tandem cells made with a front-planar rear-textured Si (reference) and with an optimally textured Si featuring an average size

of 530 nm (B_{530nm}). It is clarified that the J_{SC} gain by applying the nanopyramid texture originates from the EQE improvements of the bottom cell in the wavelength range of 800-1050 nm thanks to the elimination of the optical interferences in the reflectance spectrum. No significant change is found in the longer wavelength region (>1050 nm), agreeing with the EQE of the Si single-junction solar cells shown in Fig. 4.6(b). The increase of the bottom cell current J_{bottom}, which can be calculated by integrating the product of the EQE curves and the air mass 1.5 global solar spectrum, is 0.9 mA cm^{-2}. On the other hand, no obvious change is found in the top cell spectral response by the Si texture although the interference bumps are slightly reduced in the wavelengths of 400-750 nm. As a result, the increase of J_{bottom} is roughly matched with that of J_{SC}, indicating that J_{SC} of the reference tandem solar cell is limited by the J_{bottom} in these devices.

Next, we have applied an AR coating on top of the tandem solar cells to clarify if the gain in the J_{bottom} by Si texturing can still be preserved after implementing such an optical management. EQE spectra of tandem cells with and without nanopyramid texture after the MgF_2 (110 nm) coating on top of the front ITO layer are shown in Fig. 5. It is demonstrated that the EQE of the bottom cell with the nanopyramid Si texture still prevails even after applying the AR layer on top of the ITO layer. As a result, a gain in the J_{bottom} by ~1 mA cm^{-2} is obtained, leading to a 22.1% efficient tandem solar cell (J_{SC}=18.8 mA cm^{-2}, V_{OC}=1.693 V, FF=0.692, area=1.0 cm^2). The V_{OC} of this solar cell is relatively low compared to the V_{OC} (1.81 V) reported.[31] The V_{OC} loss comes from the inferior top cell performance due to the slightly excessive size of the nanopyramids used in this sample (B_{530nm}). In fact, V_{OC} as high as 1.81 V has been obtained with the bottom cell using a nanopyramid texture A_{420nm}, when the superior a-Si:H passivation was achieved. As mentioned earlier, however, we find that the a-Si:H passivation quality is strongly dependent on the PECVD conditioning particularly when being deposited on such a small-sized pyramid texture.[40] Unfortunately, after making a minor change in the deposition reactor of the intrinsic a-Si:H layer, we have subsequently been unable to reproduce good quality a-Si:H passivation in our nanotextured devices. Although we

have not yet found which PECVD deposition parameter is a key in passivating the nanopyramid surface like $A_{420nm,}$ such a technical issue can be solved by the minor tuning of the deposition parameters. Therefore, it is believed that the tandem cell performance can be further improved by using the nanopyramid texture like A_{420nm} in the future. Since our baseline process for the perovskite top cell is not yet well-established, even higher efficiency is expected with further optimization.

Figure 4.9 shows the cross-sectional high-angle annular field scanning transmission electron microscopy (HAADF-STEM) images of device B_{530nm}. Similar to the SEM images shown in Fig. 4.7(c), the perovskite layer is formed on a rough surface while its top surface is planarized. The cracks found in the perovskite layer and the voids (black holes) seen in both the perovskite and spiro-MeOTAD layers are most likely created by mechanical damage during the TEM sample preparation, as no such features are found in SEM images. In the magnified images, it can be seen that both i-p-a-Si:H (~10 nm) passivating contact layers and n-nc-Si:H (~25 nm) recombination junction layer grown by PECVD provide excellent conformal coverage on the Si nanopyramid surface even at the peak and valley positions. It is also clearly seen that surface roughing occurs in the n-nc-Si:H layer with a roughness height of ~10 nm. This small surface roughening was found to provide an antireflection effect at the SnO_2/Si interface in the case of a planar Si surface.[39] We observed a preliminary result that this favorable effect is still present in the case of depositing n-nc-Si:H layer on the nanopyramid Si, although the effect becomes less pronounced (Supporting Information Figure S3). On the other hand, the SnO_2 layer formed by spin coating shows relatively poor surface coverage. In particular, the thickness of SnO_2 at the valley position is ~100 nm which is thicker by a factor of two than that on the planar surface. In contrast, almost no SnO_2 layer is deposited at the tip of the pyramid. This poor coverage of SnO_2 layer can also be identified by the top-view SEM images of the Si bottom cells with an SnO_2 layer spin-coated on top (shown in Figure 4.10). As the size of the Si pyramid texture increases, the area without SnO2 coverage gradually increases, which potentially results in creating shunting paths or uneven

electron collection in the top cell. Nevertheless, at least for samples B_{530nm}, it is worth noting that this locally uncovered SnO_2 layer does not result in significant shunt or charge collection loss judging from the J-V and EQE results. Since we do not use a highly conductive recombination junction layer like ITO, this might help in preventing the local shunt creation. Alternatively, the application of a vacuum processed SnO_2 such as by atomic layer deposition[41] would be a solution to achieve complete coverage of the SnO_2 layer over the textured Si.

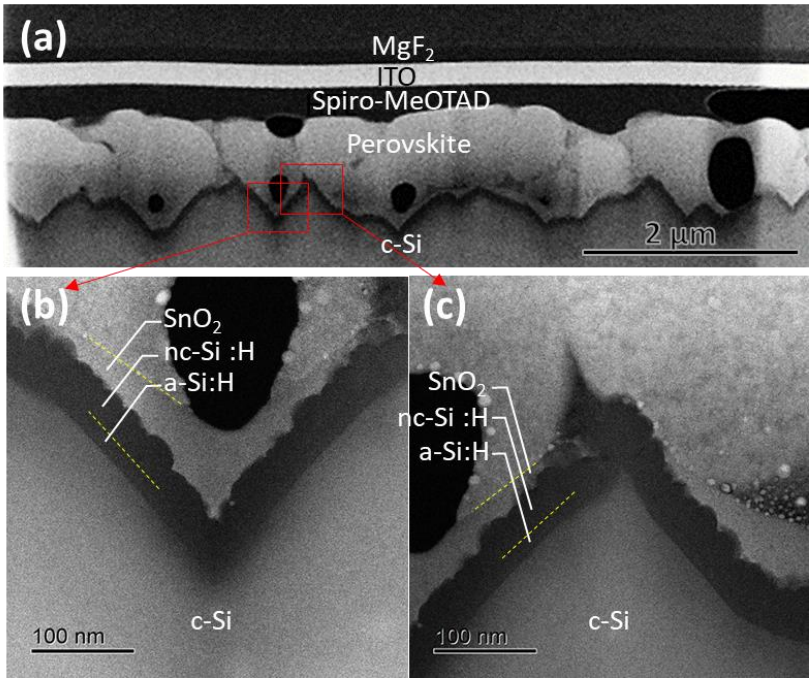

Fig. 4.9. (a) Cross-sectional HAADF-STEM images of perovskite/Si tandem solar cell fabricated with the nanopyramid Si texture B_{530nm}. The high magnification images at the valley and peak positions of a Si pyramid are shown in (b) and (c), respectively.

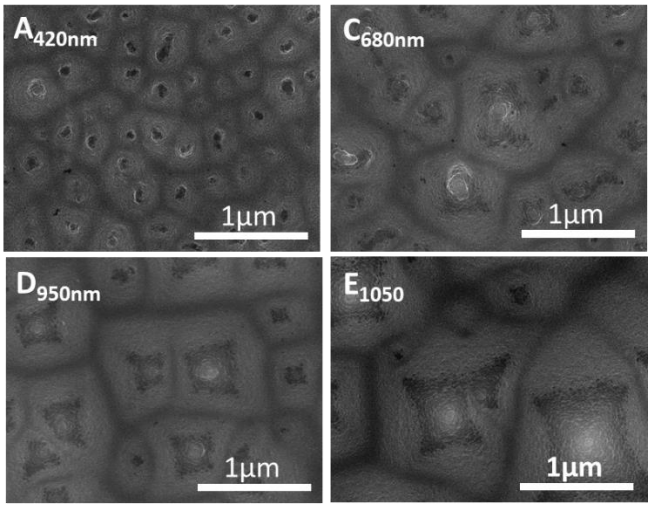

Fig. 4.10. Top-view SEM images of the SnO_2 layers formed by the spin-coating method on differently sized Si pyramids.

Next, we applied an AR coating on top of the tandem solar cells to clarify if the gain in the J_{bottom} by Si texturing can still be preserved after implementing such an optical management. EQE spectra of tandem cells with and without nanopyramid texturing after the MgF_2 (110 nm) coating on top of the front ITO layer are shown in Fig. 4.10. It is demonstrated that the effect of the Si nanopyramid texture on the light in-coupling in the bottom cell can still be preserved after applying an AR layer on top of the ITO layer. As a result, a gain in the J_{bottom} by ~1 mA cm^{-2} is obtained, leading to a 22.1% efficient tandem solar cell (J_{SC}=18.8 mA cm^{-2}, V_{OC}=1.693 V, FF=0.692, area=1.0 cm^2). In terms of PCE, this tandem cell performs slightly less efficiently compared to the reference cell made in the same batch (J_{SC}=17.5 mA cm^{-2}, V_{OC}=1.812 V, FF=0.730, PCE=23.2%, area=1.0 cm^2) because the overall loss in V_{OC} and FF is more than the gain in J_{SC}. The V_{OC} and FF losses come from the inferior top cell performance due to the slightly excessive size of the nanopyramids used in this particular sample (B_{530nm}). In fact, V_{OC} as high as 1.81 V has been obtained using the nanopyramid texture A_{420nm}, when the superior a-Si:H passivation was achieved (not shown). Therefore, it is believed that the tandem cell performance can be further improved by using a nanopyramid texture like A_{420nm} in the

future. In addition, since our baseline process for the perovskite top cell is not yet well-established, even higher efficiency is expected with further optimization.

The tandem cell performance presented here is still limited by the low J_{SC} (18.8 mA cm^{-2}) compared to the J_{SC} (~20 mA cm^{-2}) of the state-of-the-art tandem cell.[22] This gap mainly originates from the different top-cell configuration. In the *n-i-p* configuration used in this study, the refractive index mismatching at the interface between the ITO (*n*~2.0) and the thick spiro-MeOTAD (*n*~1.6) layers causes a large reflection loss, whereas the recent tandem cell based on inverted *p-i-n* configuration has no such an optical issue. Despite the inferior optical properties, the *n-i-p* configuration presented here still offers high-efficiency potential by implementing a thinner HTL layer. For example, the replacement of spiro-MeOTAD with similar derivatives such as evaporated 2,2',7,7'-tetra(N,N-di-p-tolyl)amino-9,9-spirobifluorene (spiro-TTB) with much lower thickness (~25 nm) has been demonstrated in perovskite/Si tandem solar cells with J_{SC}~19.5 mA cm^{-2} and efficiencies ~27%.[42] The simpler cell design and deposition process for *n-i-p* configuration than *p-i-n* configuration would be advantageous in industrial application.

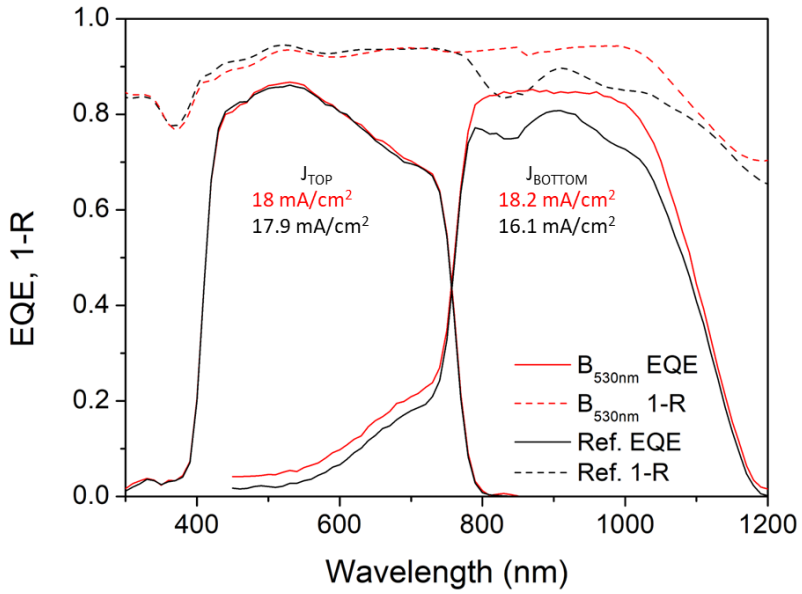

Fig. 4.10. EQE spectra of tandem solar cells with double-sided nanopyramid Si texture (B530nm) and reference front-planar rear-textured Si after the MgF2 AR coating on top of the front ITO layer. Note that the measurement artifact appearing in the bottom cell response (wavelengths: 450-720 nm) caused by the top-cell shunting was not corrected.

In terms of the nanoscale texture design, a similar approach has been reported where the Si nanopyramid texture with an average size of 500 nm was used for solution processing of perovskite top cell in monolithic two-terminal perovskite/Si tandem solar cells.[28] The size of the pyramid texture they used agrees well with our optimal texture size (i.e., A_{420nm} or B_{530nm}) for perovskite deposition. Nevertheless, their results show no distinct improvement in either top-cell or bottom-cell current, which is different from our observation. This is probably because they have employed refractive-index matching layers comprised of ITO (20 nm) and *n*-nc-SiO_x:H (90-110 nm) double interlayers which effectively suppress the internal reflection at the interface between the top and bottom cells. In contrast, our results prove that the nanopyramid texture provides a similar AR effect without using such a multilayer coating that requires an additional PVD process and the very long deposition time for a thick *n*-nc-SiO_x:H layer by PECVD. Thus, the biggest advantage of our device architecture is the TCO-free interface design which

offers the opportunity towards realizing industrially feasible high-efficiency tandem solar cells. The use of nanopyramid texture on both sides of the Si wafer is also beneficial in improving tandem solar cell performance without additional cost, if compared to the use of single-sided textured Si or asymmetrically textured Si that has been used for perovskite/Si tandem solar cell development at a laboratory scale.

Finally, we address the possible industrial solution processes for the fabrication of the perovskite layer. In this study, we employed the spin coating method as it is most widely used in the laboratory. However, it is known that spin coating is not industrially feasible because of the large waste of the precursor materials and the limitation for the large-area uniform deposition. Instead, various industrial solution processes have been proposed such as blade coating[43], spray coating[44], inkjet printing[45] etc. Although the compatibility of these processes needs to be investigated, it is expected that the nanoscale texture developed here can be used for these industrial solution processes if the same/similar precursor solution is used.

4.3.3 Future work

At this stage, we have successfully fabricated uniform distributed Si nanopyramid texture with an average size of 400nm on the surface c-Si substrates. However, after being applied to Si/perovskite tandem cells, the highest efficiency has reached 22.1%, which is still to be further improved compared with the current highest record of 33.8%[46]. There are mainly two issues waiting for further improvement, one is surface passivation of the bottom cell and the other is structural optimization of the top perovskite cell. We found that under the same a-Si:H passivation layer deposition conditions by PECVD, the passivation effect on nano-sized Si pyramids is very unstable, especially with the size of Si nanopyramids decreased. This may be caused by an overly thick passivation layer, thus tt is necessary to further adjust the deposition conditions of PECVD to match the thickness of a-Si:H passivation layer with the nano-texture to achieve the perfect passivation effect. At the same time, by changing the thickness of the perovskite layer

which match the difference size of Si nanotextures, better current matching could be achieved . In addition, using the current mainstream p-i-n structure instead of the n-i-p structure utilized in this study and using new materials such as C60 as the n-layer of perovskite top cell is expected to further improve the efficiency of tandem cells.

4.4 Conclusion

We explored the effect of size variation of Si nanopyramid textures of the bottom cell on the overall perovskite/Si tandem cell performance. Double-sided Si nanopyramid textures having different average sizes of 400-900 nm with improved size distribution were fabricated using an original Ag-assisted alkaline etching method and applied in the bottom cell of perovskite/Si tandem cells. As the size of the Si pyramid increases, the light absorption of the bottom cell gradually increases, while excessive pyramid size (>600 nm) causes severe electrical shunting and thickness inhomogeneity in the perovskite absorber layer, resulting in the degradation in the performance of tandem cells, particularly in the V_{OC}. We find that the optimum Si texture size is around 400-500 nm, by which the perovskite top cell can be processed entirely by the conventional spin-coating method without creating an electrical shunting path in the top cell. Compared to the front-planar rear-textured reference Si bottom cell, the double-sided textured Si bottom cell with an average size of 530 nm provides a J_{SC} improvement by ~1.0 mA cm^{-2} and a higher PCE as a result of the increased spectral response in the Si bottom cell due to the suppressed interfacial reflection between the top and bottom cells. The results obtained in this study show the great potential for cost-effective tandem cell manufacturing using the solution-based top cell process without needing the costly multilayer optical coating nor the lithography patterning step at the top/bottom interface.

References

[1] International Technology Roadmap for Photovoltaic (ITRPV). **2021**.

[2] K. Yoshikawa, H. Kawasaki, W. Yoshida, T. Irie, K. Konishi, K. Nakano, T. Uto, D. Adachi, M. Kanematsu, H. Uzu, K. Yamamoto *Nat. Energy* **2017**, *2*, 17032.

[3] H. Lin, M. Yang, X. Ru, G. Wang, S. Yin, F. Peng, C. Hong, M. Qu, J. Lu, L. Fang, C. Han, P. Procel, O. Isabella, P. Gao, Z. Li, X. Xu *Nat Energy* **2023.** https://doi.org/10.1038/s41560-023-01255-2

[4] A. Richter, M. Hermle, S. W. Glunz *IEEE J. Photovoltaics* **2013**, *3*, 1184.

[5] S. Schafer, R. Brendel *IEEE J. Photovoltaics* **2018**, *8*, 1156.

[6] A. Kojima, K. Teshima, Y. Shirai, T. Miyasaka *J. Am. Chem. Soc.* **2009**, *131*, 6050.

[7] M. M. Lee, J. Teuscher, T. Miyasaka, T. N. Murakami; H. J. Snaith *Science* **2012**, *338*, 643.

[8] M. Kim, J. Jeong, H. Lu, T. K. Lee, F. T. Eickemeyer, Y. Liu, I. W. Choi, S. J. Choi, Y. Jo, H. Kim, S. Mo, Y. Kim, H. Lee, N. G. An, S. Cho, W. R. Tress, S. M. Zakeeruddin, A. Hagfeldt, J. Y. Kim, M. Grätzel, D. S. Kim *Science* **2022**, *375*, 302.

[9] J. Park, J. Kim, H.S. Yun, M. J. Paik, E. Noh, H. J. Mun, M. G. Kim, T. J. Shin, S. I. Seok *Nature* **2023**, *616*, 724.

[10] NREL Best Research-Cell Efficiency Chart, https://www.nrel.gov/pv/cell-efficiency.html

[11] A. W. Ho-Baillie, J. Zheng, M. A. Mahmud, F. J. Ma, D. R. McKenzie, M. A. Green *Appl. Phys. Rev.* **2021**, *8*, 041307.

[12] P. Tockhorn, P. Wagner, L. Kegelmann, J. C. Stang, M. Mews, S. Albrecht, L. Korte *ACS Appl. Energy Mater.* **2020**, *3*, 1381.

[13] F. Sahli, B. A. Kamino, J. Werner, M. Bräuninger, B. P-Salomon, L. Barraud, R.Monnard, J. P. Seif, A. Tomasi, Q. Jeangros, A. H-Wyser, S. D. Wolf, M. Despeisse, S. Nicolay, B. Niesen, C. Ballif *Adv. Energy Mater.* **2018**, *8*, 1701609.

[14] L. Mazzarella, M.Werth, K. Jäger, M. Jošt, L. Korte, S. Albrecht, R. Schlatmann, B. Stannowski *Opt. Express* **2018**, *26*, A487.

[15] L. Mazzarella, Y.H. Lin, S. Kirner, A. B. Morales-Vilches, L. Korte, S. Albrecht, E. Crossland, B. Stannowski, C. Case, H. J. Snaith, *Adv. Energy Mater.* **2019,** *14*, 1803241.

[16] R. Santbergen, R. Mishima, T. Meguro, M. Hino, H. Uzu, J. Blanker, K. Yamamoto, M. Zeman *Optics Express* **2016**, 24, A1288.

[17] A. Al-Ashouri, E. Köhnen, B. Li, A. Magomedov, H. Hempel, P. Caprioglio, J. A. Márquez, A. B. M. Vilches, E. Kasparavicius, J. A. Smith, N. Phung, D. Menzel, M. Grischek, L. Kegelmann, D. Skroblin, C. Gollwitzer, T. Malinauskas, M. Jošt, G. Matic, B. Rech, R. Schlatmann, M. Topic, L. Korte1, A. Abate, B. Stannowski, D. Neher, M. Stolterfoht, T. Unold, V. Getautis, S. Albrecht *Science* **2020**, *370*, 1300.

[18] D. A. Jacobs, M. Langenhorst, F. Sahli, B. S. Richards, T. P. White, C.Ballif, K. R. Catchpole, U. W. Paetzold *J. Phys. Chem. Lett.* **2019**, *10*, 3159.

[19] F. Sahli, J. Werner, B. A. Kamino, M. Bräuninger, R. Monnard, B. P. Salomon, L. Barraud, L. Ding, J. J. D. Leon, D.Sacchetto, G. Cattaneo, M. Despeisse, M. Boccard,

S. Nicolay, Q. Jeangros, B. Niesen, C. Ballif *Nat. Mater.* **2018**, 17, 820.
[20] X. Luo, H. Luo, H. Li, R. Xia, X. Zheng, Z. Huang, Z. Liu, H. Gao, X. Zhang, S. Li, Z. Feng, Y. Chen, H. Tan *Adv. Mater.* **2023**, *35*, 2207883.
[21] L. Mao, T. Yang, H. Zhang, J. Shi, Y. Hu, P. Zeng, F. Li, J. Gong, X. Fang, Y. Sun, X. Liu, J. Du, A. Han, L. Zhang, W. Liu, F. Meng, X. Cui, Z. Liu, M. Liu *Adv. Mater.* **2022**, *34*, 2206193.
[22] X. Y. Chin, D. Turkay, J. A. Steele, S. Tabean, S. Eswara, M. Mensu, P. Fiala, C. M. Wolf, A. Paracchino, K. Artuk, D. Jacobs, Q. Guesnay, F. Sahli, G. Andreatta, M. Boccard, Q. Jeangros, C. Ballif *Science* **2023**, 381, 59.
[23] Y. Hou, E. Aydin, M. D. Bastiani, C. Xiao, F. H. Isikgor, D. Xue, B. Chen, H. Chen, B. Bahrami, A. H. Chowdhury, A. Johnston, S. W. Baek, Z. Huang, M. Wei, Y. Dong, J. Troughton, R. Jalmood, A. J. Mirabelli, T. G. Allen, E. V. Kerschaver, M. I. Saidaminov, D. Baran, Q. Qiao, K. Zhu, S. D. Wolf, E. H. Sargent *Science* **2020**, *367*, 1135.
[24] B. Chen, Z. J. Yu, S. Manzoor, S. Wang, W. Weigand, Z. Yu, G. Yang, Z. Ni, X. Dai, Z. C. Holman, J. Huang *Joule* **2020,** *4*, 850.
[25] C. Becker, J. Sutter, P. Tockhorn, A. B. M. Vilches, B. Stannowski, S. Albrecht Optica Publishing Group, **2020**, PvW1G. 4.
[26] P. Tockhorn, J. Sutter, A. Cruz, P. Wagner, K. Jäger, D. Yoo, F. Lang, M. Grischek, B. Li, J. Li, O. Shargaieva, E. Unger, A. Al-Ashouri, E. Köhnen, M. Stolterfoht, D. Neher, R. Schlatmann, B. Rech, B. Stannowski, S. Albrecht, C. Becker *Nat. Nanotechnol.* **2022**, *17*, 1214.
[27] Z. Ying, Z. Yang, J. Zheng, H. Wei, L. Chen, C. Xiao, J. Sun, C. Shou , G. Qin, J. Sheng, Y. Zeng, B.Yan, X. Yang, J. Ye *Joule* **2022**, *6*, 2644.
[28] A. Harter, S. Mariotti, L. Korte, R. Schlatmann, S. Albrecht, B. Stannowski *Prog. Photovolt. Res. Appl.* **2023**,1, doi:10.1002/pip.3685.
[29] SN. Granata, T. Bearda, F. Dross, I. Gordon, J. Poortmans, R. Mertens *Energy Procedia* **2012**, 27, 412.
[30] H. Sai, T. Oku, Y. Sato, M. Tanabe, T. Matsui, K. Matsubara *Prog. Photovolt.: Res. Appl.* **2019**, *27*, 1061.
[31] H. Umishio, H. Sai, T. Koida, T. Matsui *Prog. Photovolt.: Res. Appl.* **2021**, *29*, 344.
[32] C. McDonald, H. Sai, V. Svrcek, A. Kogo, T. Miyadera, T. N. Murakami, M. Chikamatsu, Y. Yoshida, T. Matsui ACS Appl. Mater. & Interfaces 2022, 14, 33505.
[33] L. Mazzarella, S. Kirner, O. Gabriel, S. S. Schmidt, L. Korte, B.Stannowski, B. Rech, R. Schlatmann *Phys. Status Solidi A* **2017**, *214*, 1532958.
[34] M. Saliba, T. Matsui, K. Domanski, J. Y. Seo, A. Ummadisingu, S. M. Zakeeruddin, J. P. Correa-baena, W. R. Tress, A. Abate, A. Hagfeldt, M. Grätzel *Science* **2016,** *354*, 206.
[35] https://www2.pvlighthouse.com.au/calculators/OPAL%202/OPAL%202.aspx.
[36] Y. Li, H. Sai, T. Matsui, Z. Xu, V. H. Nguyen, Y. Kurokawa, N. Usami Sol. RRL. 2022, 6, 2200707.
[37] L. Wang, Y. Zhang, M. Kim, M, Wright, R. Underwood, R. S. Bonilla, B. Hallam Prog. Photovolt. Res. Appl. 2023, https://doi.org/10.1002/pip.3687.

[38] H. Sai, Y. Kanamori, K. Arafune, Y. Ohshita, M. Yamaguchi Prog. Photovolt.: Res. Appl. 2007, 15, 415.
[39] H. Sai, H. Umishio, T. Matsui Sol. RRL 2021, 5, 2100634.
[40] B. Stegemann, J. Kegel, M. Mews, E. Conrad, L. Korte, U. Stürzebecher, H. Angermann Energy Procedia 2013, 38, 881.
[41] Y. Kuang, V. Zardetto, R. van Gils, S. Karwal, D. Koushik, M. A. Verheijen, L. E. Black, C. Weijtens, S. Veenstra, R. Andriessen, W. M. M. Kessels, M. Creatore ACS Appl Mater Interfaces 2018, 10, 30367.
[42] E. Aydin, J. Liu, E. Ugur, R. Azmi, G. T. Harrison, Y. Hou, B. Chen, S. Zhumagali, M. De Bastiani, M. Wang, W. Raja, T. G. Allen, A. U. Rehman, A. S. Subbiah, M. Babics, A. Babayigit, F. H. Isikgor, K. Wang, E. Van Kerschaver, L. Tsetseris, E. H. Sargent, F. Laquai, S. De Wolf, Energy Environ. Sci. 2021, 14, 4377.
[43] J. Yang, E. L. Lim, L. Tan, Z. Wei Adv. Energy Mater. 2022, 12, 2200975.
[44] E. J. Cassella, E. L. K. Spooner, T. Thornber, M. E. O'Kane, T. E. Catley, J. E. Bishop, J. A. Smith, O. S. Game, D. G. Lidzey Adv. Sci. 2022, 9, 2104848.
[45] F. Schackmar, H. Eggers, M. Frericks, B. S. Richards, U. Lemmer, G. Hernandez-Sosa, U. W. Paetzold Adv. Mater. Technol. 2021, 6, 2000271.
[46] https://www.pv-magazine.com/2023/05/30/kaust-claims-33-7-efficiency-for-perovskite-silicon-tandem-solar-cell/

5.Si nanowire structures

5.1 Introduction

5.1.1 Background

5.1.1.1 PEDOT:PSS/Si Hybrid heterojunction solar cells (HHSCs)

Another way to reduce the cost is employing organic materials. In recent years, c-Si heterojunction hybrid solar cells (HHSCs) utilizing solution processable materials have received great attention thanks to low-temperature dopant free fabrication process and low production cost compared to c-Si solar cells. The highest reported power conversion efficiency (PCE) of HHSCs is 16.2%.[1] Among different hole-selective materials, poly(3,4-ethylenedioxythiophene): poly(styrenesulfonate) (PEDOT:PSS) was vastly applied as hole transporting layers to form p-n junction with n-type Si (n-Si) to form hybrid c-Si solar cells since it possesses high conductivity, high transparency, wide band gap, and relatively high work function, ϕm = 5.0 eV.[2] Figure 5.1 shows the structure of Organic/Si hybrid heterojunction solar cells employing PEDOT: PSS. This kind of heterojunction solar cells rely on interfacial band offsets of the heterojunction between the hole-selective materials and c-Si substrates, rather than the conventional high-temperature diffused homo junction, to effectively separate photon-generated carriers, which can reduce the fabricating cost a lot.[3] However, till now, the power conversion efficiency of these new generation solar cells is far from satisfactory for commercial applications compared with the traditional bulk Si solar cells. In order to put these cost -effective solar cells into practical use, further structural optimization is necessary to improve their performance.

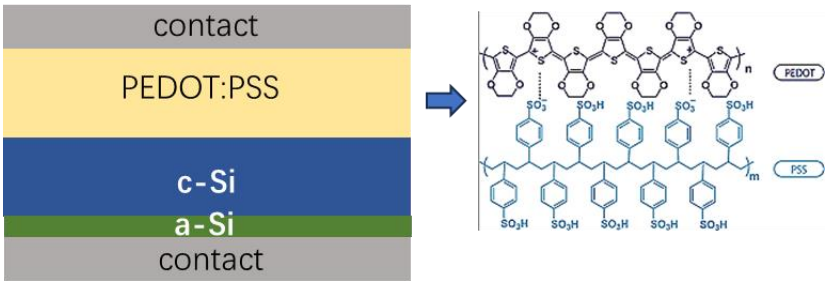

Figure 5.1. Shematic of PEDOT:PSS/Si Hybrid heterojunction solar cells (HHSCs)

5.1.1.2 Hybrid heterojunction solar cell employing Si nanowires/Si nanotips

To further improve the property of hybrid heterojunction solar cells, nanostructures are often applied to the interface of PEDOT: PSS and c-Si substrates(Figure 5.2 (a)), for its excellent light absorption capability by light antireflective and scattering effects as well as the radial p–n junction architectures which provide a large junction area for charge separation.[4,5] Recently, hybrid solar cell of Organic/SiNWs with power conversion efficiency (PCE) of 16.1% has been achieved by embedding Ag/SiO_2 electrode between Si NW arrays underneath PEDOT:PSS [6], which still has a lot of room for improvement. During the fabricating process, PEDOT: PSS film is usually coated on to Si substrate by spin coating. Figure 5.2 (b) shows the interface of PEDOT: PSS solution and Si surface during spin coating. The large area surface of SiNWs leads to incomplete infiltration of PEDOT: PSS solution into nanostructures and form many voids at the interface, these places are un-passivated and will lead to carrier recombination. To further improve the conversion efficiency, optimization of surface morphology is necessary.

The main reasons that limit the further improvement of the efficiency of organic/SiNWs solar cells are:Incomplete infiltration of PEDOT:PSS solution into nanostructures, and the surface recombination centers due to large defects area. Studies have shown that PEDOT:PSS have better infiltration among sparsely distributed and tapered Si nanowires,thus contributes to better cell efficiency.[7,8] With surface morphology treatment like tapered Si nanowire, the combination between PEDOT:PSS and Si texture can be improved. As shown in Figure 5.3, by increasing the tilt of the top

of the SiNWs and expanding the gap in front of the SiNWs, the contact between the Si nanotexture and PEDOT:PSS can be improved while maintaining high light absorption, and the carrier recombination sites can be reduced. This provides a feasible solution to improve organic/Si nanostructured hybrid solar cells in an energy- and cost-effective manner.[9, 10]

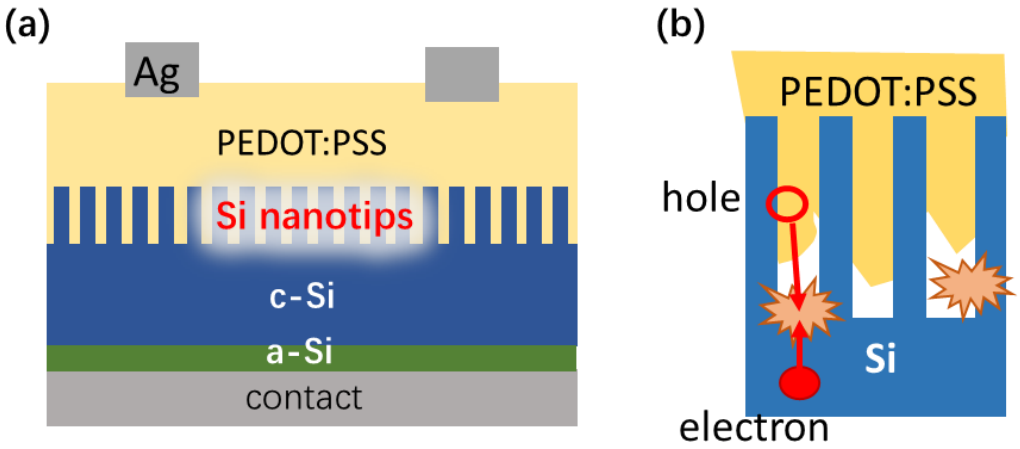

Figure 5.2. (a) Schematic diagram of SiNWs/PEDOT:PSS hybrid solar cells; (b) Carriers recombine in the gaps between PEDOT:PSS and SiNWs.

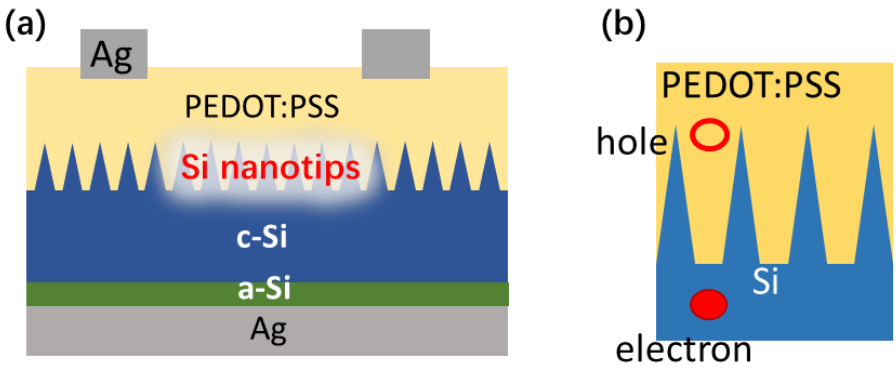

Figure 5.3. (a) Schematic diagram of Si nanotips/PEDOT:PSS hybrid solar cells; (b) Carriers recombine in the gaps between PEDOT:PSS and Si nanotips.

5.1.2 research purpose

As mentioned above, the MACE etching process is a simple and efficient method for fabricating Si nanowires. In this research, we attempt to explore the influence of different variables in the two steps of the MACE process on the surface morphology of the formed SiNWs, and investigate the impact of different SiNWs surface morphology on optical properties. On the basis of these studies, we hope to develop a facile solution process based on MACE method to fabricate Si nanotips, and optimizing the surface morphology of Si nanotips with better combination with PEDOT: PSS solution during coating process as well as good optical peroperty, for the application on organic/c-Si hybrid solar cells to further improve the conversion efficiency.

5.2 Experimental Details

5.2.1 Si nanotips fabrication

The fabrication process of Si nanotips was showed in figure 5.4. First, electroless Ag plating was done by immersing Si wafers into mixture solution of HF and $AgNO_3$ to form Ag particles on surface of Si wafers, then Si wafers were etched in an mixed silution of HF and H_2O_2 to form Si nanowire structures. Polishing treatment are employed at last to further modify the SiNWs into Si nanotips morphology. The detailed experimental process are as follows:

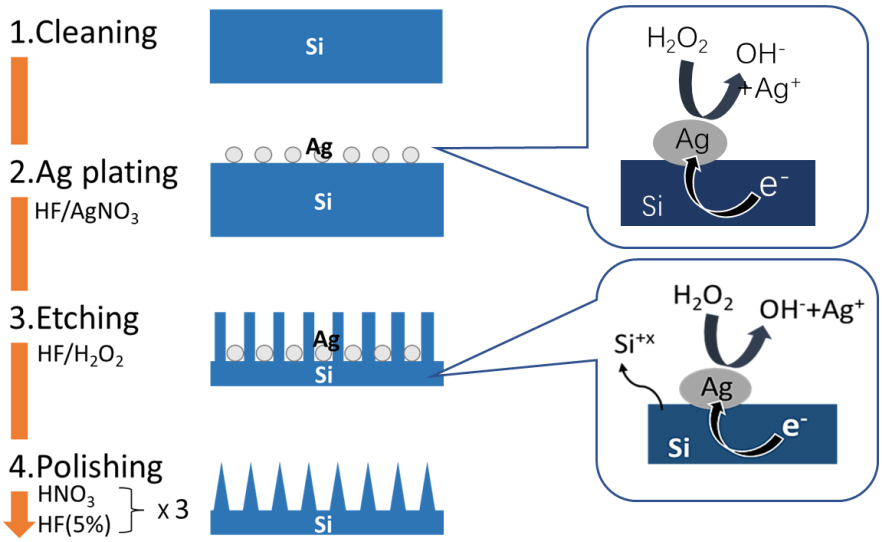

Figure 5.4. Metal-assisted electroless etching (MAE)

(i) Electroless Ag plating

N-type Si substrates with (100) orientation were used. The substrate was cut into a dimension size of o1.5cm 1.5cm, and cleaned to remove any organic and metallic contaminant in acetone by supersonic cleaning. All of the chemical experimental process were done in a chemical fume hood. Ag plating solution with Ag^+ concentration of 3mM, 6mM, 9mM, 12mM made by 10ml HF, 40ml deionized water and $AgNO_3$ in different qualities weighed by electronic balance, and then mixed together and stirring for five minutes by magnetic stirrer. Si substrates were immersed in 5% HF solution for 1min to remove the SiO_2, and then immersed in Ag plating solution with a stirrer at room temperature to make Ag particles attached on the Si surface. The plating time varied from 20s to 60s.

(ii) Etching

Etching solution is made by 10ml HF, 40ml deionized water and H_2O_2 with a varying amount of 700ul, 1050ul, 1400ul, respectively. The solution was stirred for 5mins. Si substrates with Ag particles attached then were immersed in the etching solution at room temperature to fabricate Si nanowire structures. The etching time was 37s and 75s.

(iii) Chemical polishing

Si substrates after etching were first immersed in HNO_3 solution for 5mins to remove the residual Ag, and then were immersed in 5% HF solution to remove SiO_2 due to oxidation of Si by HNO_3. This polishing process was repeated for 3 times to ensure all Ag has been removed, and the effect of chemical polishing also changes the morphology of the nanowires during this process.

5.2.3 PEDOT:PSS layer formation

PEDOT:PSS solution was made by an amount of 500μL solution of PEDOT:PSS (Heraeus Clevios PH 1000) mixed with Triton surfactant (Sigma Aldrich) and methanol (Fujifilm Wako Pure Chemical Co.) with different amount following volume ratio of 1:3. [11] The mixed solutions were standed under ultrasonic vibration for 24 hours at room temperature before usage. PEDOT:PSS was spun onto Si substrates with Si nanowires and Si nanotips texture (1.5×1.5 cm2) at speeds of 6000 rpm for 60 s, and then the Si substrates wew annealled in air at 170℃ for 20 min. The surface morphology of Si NWs and Si nanotips was observed using SEM.

5.3 Results and discussions

5.3.1 Previous research

5.3.1.1 Ag plating time

N-type Si substrates with a size of 1.5 X 1.5 cm were immersed in Ag plating solutions with Ag^+ concentrations of 4.6mM ($AgNO_3$: HF: H_2O = 120mg: 10ml: 40ml) for 20s, 40s, 50s, 60s respectively. After Ag removal, they were rinsed with deionized water and dried with a nitrogen gun.

Distribution of Ag particles formed on Si surface was observed by SEM (Figure 5.5). Diameter of Ag particles under different Ag plating time increased as the increased plating time, and surface coverage gradually increased with deposition time follows 68%, 69%, 70% and 71%, respectively. With the increase of the Ag plating time, it is worth

noting that when the diameter of Ag particles gradually increased to a certain size (The maximum diameter of ~230nm) with the deposition time, when the diameter of the Ag particle increased to a certain size (The maximum diameter of ~230nm), it changed from lateral growth to radial growth, and finally developed into Ag dendrites, like what is showed in figure 5.4 (d).

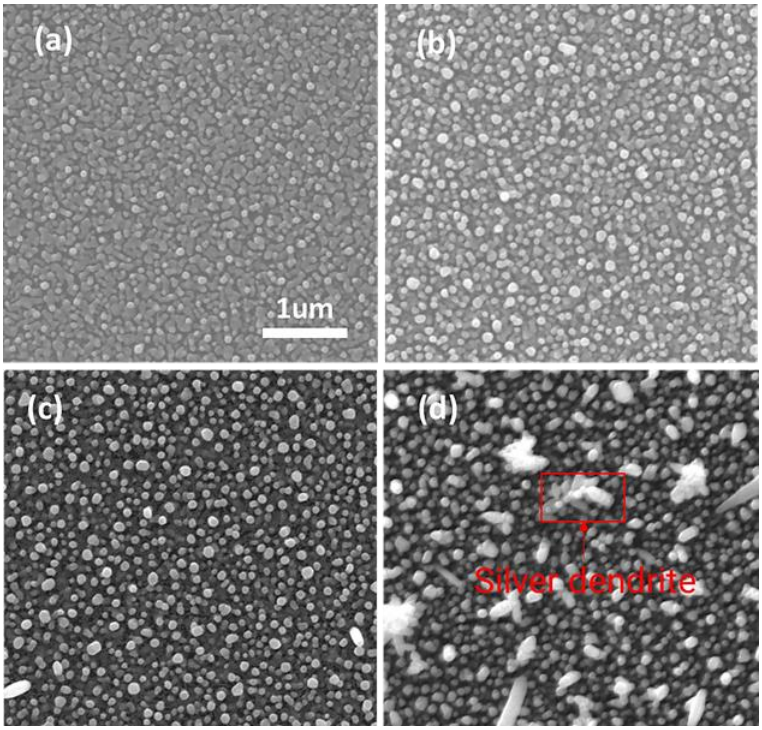

Figure 5.5. SEM images of Ag particles formed on Si at different Ag plating times of (a) 20s; (b) 40s; (c) 50s; (d) 60s.

The formation process of Ag particles is showen in Figure 5.6. Since Ag nucleation and growth is a highly dynamic process allowing Ag to dissolve, redeposit, and/or surface migrate to more energetically favored sites. [12] And the free energy of one big nanoparticle is less than the free energy of two smaller nanoparticles of equal volume. During the Ag plating process, first nano-sized Ag particles are randomly generated on the Si surface. After that, small Ag particles will merge into larger Ag particles to reduce the free energy and achieve a more stable thermodynamic state. In the process, newly generated Ag particles will also be added to the larger Ag particle clusters that have been

formed until the size of all Ag particles reaches a certain threshold. Then the Ag particle cluster began to grow upwards. At this stage, the diameter of the protruding Ag particles was about 100 nm, and eventually dendritic crystals of different sizes were formed.

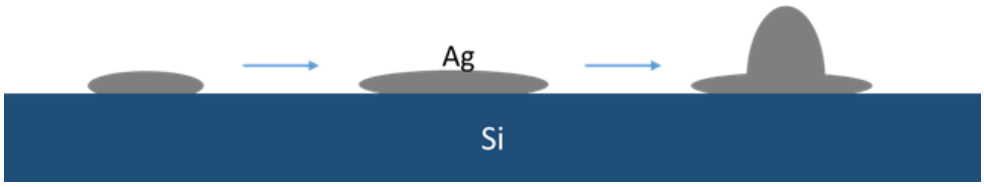

Figure 5.6. Schematic diagram of growth process of Ag particles.

5.3.1.2 Ag concentration

N-type Si substrates with a size of 1.5 X 1.5 cm^2 were immersed in Ag plating solutions with Ag^+ concentrations of 3 mM, 6 mM, 9 mM, and 12 mM respectively, and left for 30 seconds.

SEM images of Ag particles formed on Si at different Ag concentrations were showed in figure 5.7. Similar to the results with increasing the Ag plating time under fixed Ag concentration, the SEM results showed that under the same depositing time, as the Ag^+ concentration increased, the Ag particles formed on the Si surface first grew laterally from a size below 100 nm until ~230nm, and then grew radially and have a tendency to form dendrites. Because the growth rate of Ag particles was very fast before reaching the critical size of transition from horizontal to vertical growth, a lower Ag^+ concentration was beneficial to achieve even distributed Ag particles with smaller diameter below 100 nm.

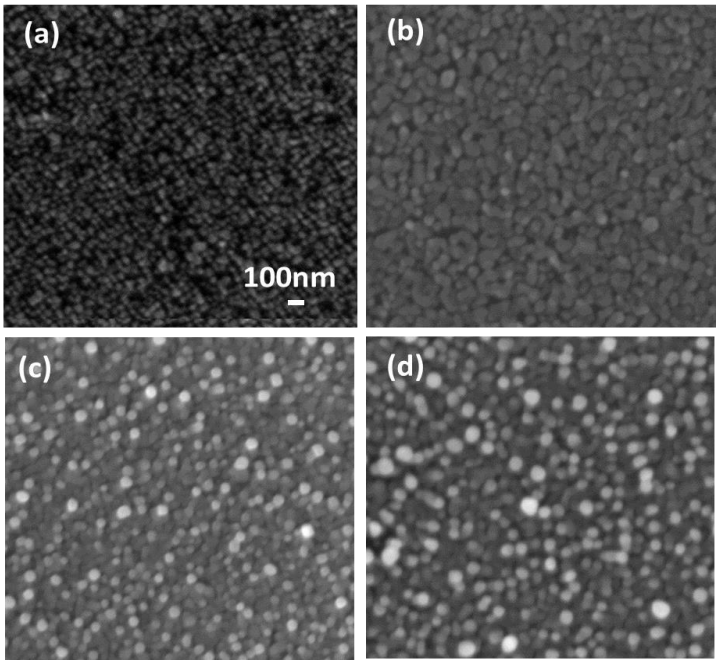

Figure 5.7. SEM images of Ag particles formed on Si at different Ag concentrations of (a) 3mM, (b) 6mM, (c) 9mM, (d) 12Mm.

5.3.1.3 Length/diameter control of Si nanowires

The etching process was implied after Ag plating with four different Ag concentrations and the cross-section SEM images of fabricated Si nanowires were showed in Figure 5.8. H_2O_2 concentration in the etching solution was 5.52M (840µl) and etching time was 40s. It can be seen from the figure and that the diameter of the Si nanowires was controlled by the Ag particles. As the diameter of Ag particles increased, the average diameter of Si nanowires decreased. The effect of Ag concentration on the length of Ag nanowires was slight. In addition, it could be learned from table 5.1 that with the increase of Ag^+ concentration, the distribution of etched Si nanowires is more uniform, the diameter is smaller, and the size distribution is narrower. As a result, Si nanowire within different diameters could be fabricated by control the size of Ag particles formed on Si surface.

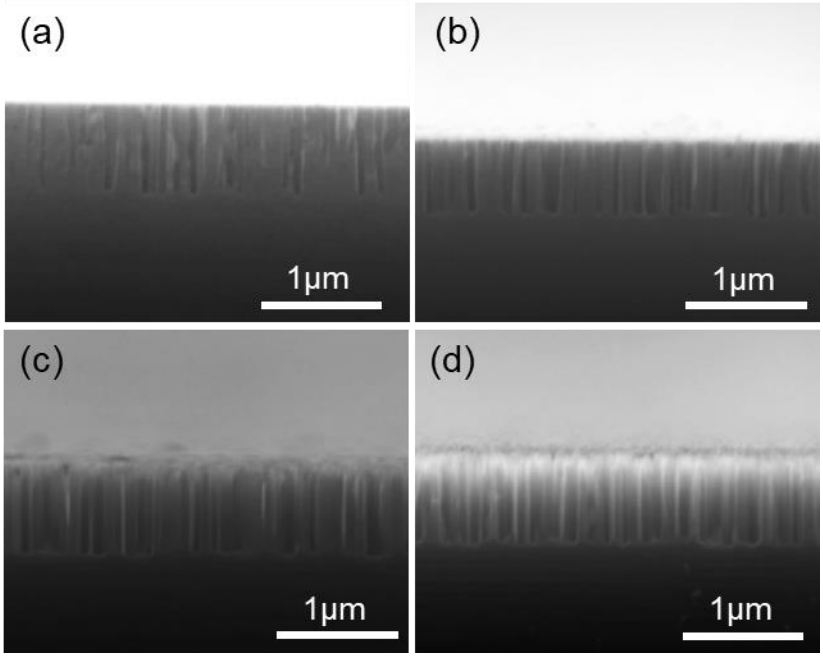

Figure 5.8. SEM images (cross-section) of Si nanowires fabricated at Ag concentrations of (a) 3mM, (b) 6mM, (c) 9mM, (d) 12Mm.

Table 5.1 diameter of Si nanowire formed at different Ag concentrations calculated by Image J.

Ag concentration	3mM	6mM	9mM	12mM
Diameter/nm	64~300	46~234	51~143	40~90
Length/nm	731	650	686	723

As shown in the figure 5.9, Si nanowires with different lengths of 0.5um, 1um, 5um, and 10um are fabricated by etching for 37s, 75s, 6min15s, and 12min30s respectively under the same Ag plating condition and etching solution.

On the basis of previours research, Si nanowires of different diameters(micropours, 200nm, 150nm, 100nm) was fabricated by adjusting the size and distribution of Ag particles in the Ag plating process; while different length of Si nanowires (0.5μm, 1μm, 5μm, 10μm) was fabricated by adjusting the etching time in HF/H_2O_2 solution. In order to evaluate the effect of changing the diameter and length of Si nanowires on optical

performance, the light absorption spectrum of Si nanowires with four different diameters and lengths were measured and shown in Figure 5.10 (a) and (b). We can see that light absorption enhanced significantly with Si nanowire structures comepare with flat Si, and in the full wavelength range(300nm-1200nm), the light absorption increases with the decrease of Si nanowire diameter. Si nanowires with a diameter of 100nm showed the best light absorption effect. It can be seen that the effect of the length of Si nanowires on the light absorption does not show an obvious trend, and the different lengths of Si nanowires show similar results below the wavelength of 1000nm, while in the long wavelength range above 1000nm, the light absorption is more significantly affected by the length of the Si nanowire. Considering the need to minimize the surface area of the Si texture, Si nanowires with a length of 0.5 μm are optimal.

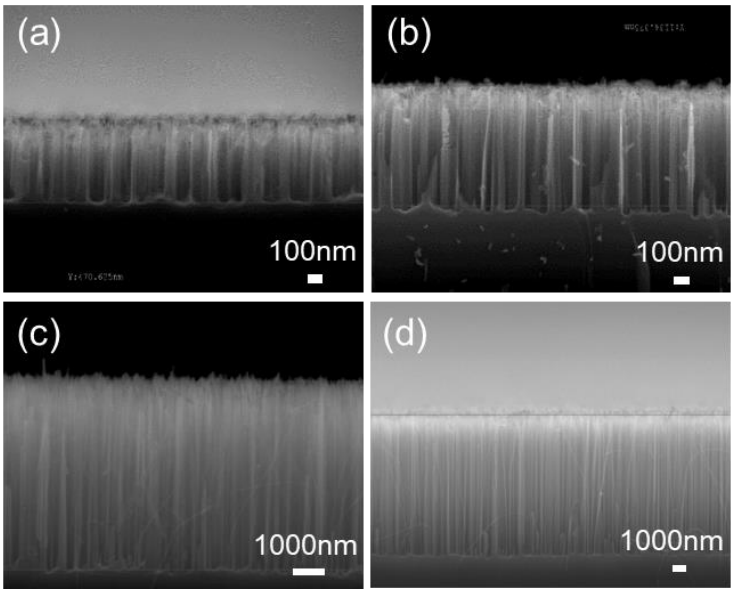

Figure 5.9. cross-sectional SEM images of Si nanowires with length of a) 0.5um, (b) 1um, (c) 5um, (d) 10um

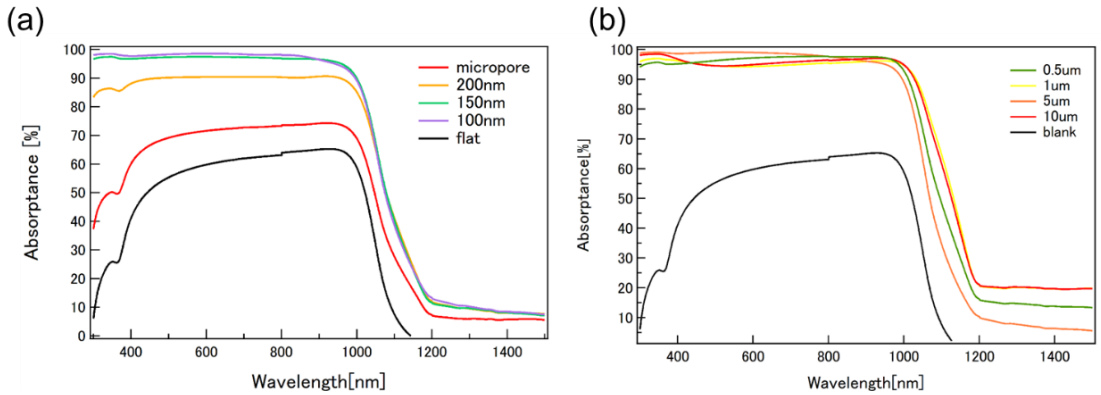

Figure 5.10. (a) Light absorptance of Si nanowire in different diameters of micropours, 200nm, 150nm, 100nm; (b) Light absorptance of Si nanowire in different lengths of 0.5µm, 1µm, 5µm, 10µm.

5.3.2 Fabrication of Si nanotips and application in PEDOT:PSS/Si solar cell

Figure 5.11 (a) and (b) showed the cross-sectional SEM images of Si nanowires etched at (a) high H_2O_2 concentration and (b) low H_2O_2 concentration respectively before and after $HN0_3$/ HF polishing treatment. It can be seen that the Si nanowires etched by high-concentration H_2O_2 showed a tapered shape with a sharp tip (Si nanotip) after being polished by HNO_3/HF. However, the shape of the Si nanowires etched by low concentration H_20_2 did not change significantly after polishing treatment. On the basis of this phenomenon, Si nanotips with different length were successfully fabricated by changing the etching time as 37s, 75s and 92s under high H_2O_2 concentration of 9.3M (1400ml), showed in Figure 5.12, the lengths of the obtained Si nanotips are 670mm, 930mm and 1300mm respectively. Further, to find out the optimal etching condition for light confinement structure, the light absorption of Si nanotips with different lengths was measured. The result in figure 5. 13 indicates that light absorption increases first and then decreases with the length of Si nanotips, when the etching time is 75s, the obtained Si nanotips with a length of about 930nm exhibits the best light absorption which exceeding that of a Si nanowire structure with the same length, especially in short-waveletgth range. This is because compared with Si nanowires, Si nanotips have a larger

gap at the top, allowing more incident light to enter the nanostructure and be captured, the axial localization feature of the

scattering light partly contributes to the better performance of SiNC than SiNW in light-absorption for

short wavebands. Besides, the random size distribution of height and diameters of Si nanotips is beneficial to the multiple cattering of incident light. [13-15]

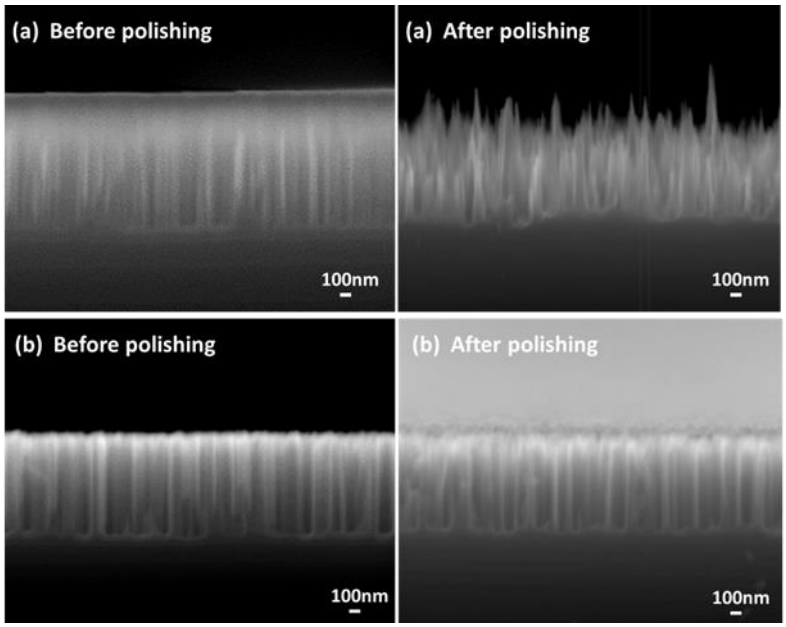

Figure 5.11. Cross-sectional SEM images of Si nanowires at (a) high H_2O_2 concentrations; (b) low H_2O_2 concentrations before&after polishing treatment fabricated.

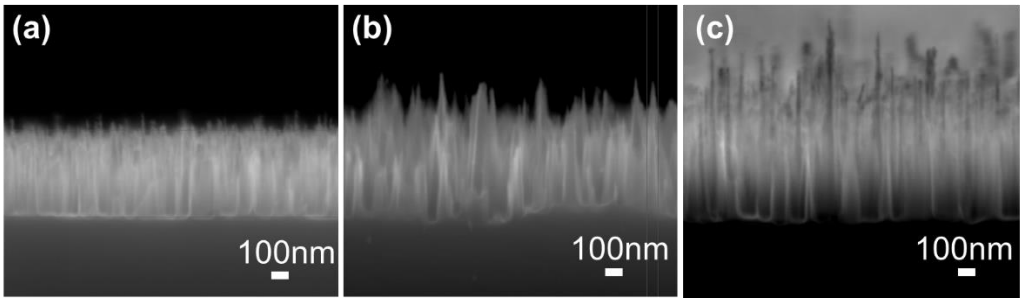

Figure 5.12. SEM images (cross-section) of tapered Si nanowires fabricated by different etching time of (a)37s, (b)75s, (c)92s.

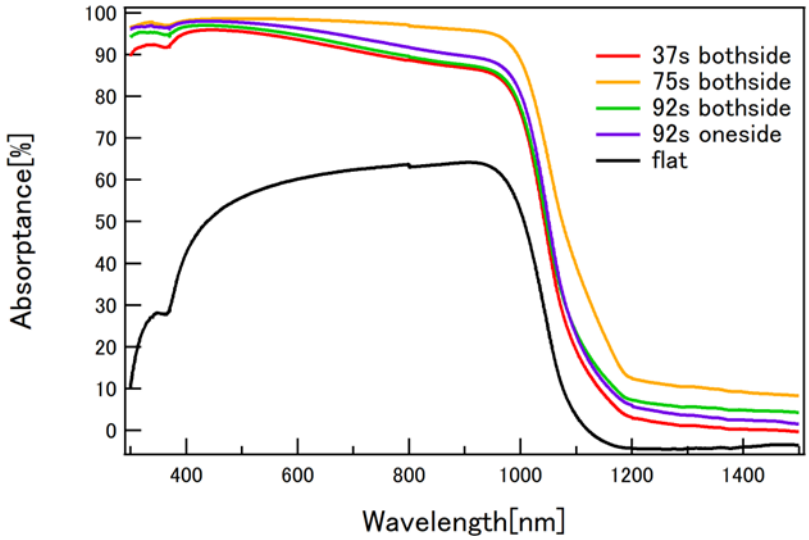

Figure 5.13. Light absorptance of Si nanotips with different etching time of 37s, 75s and 92s.

Subsequently, in order to explore the improvement of Si nanotips on the conformal layer formation of organic material at the interface of PEDOT: PSS /Si hybrid cells, PEDOT: SS layer was deposited onto the surface of the Si nanowires and Si nanotips by spin-coating, which are shown in figure 5.14. Compared with Si nanowires, contact area between the Si nanotips and the organic layer are increased due to the decreased surface area, and the increased spacing at the top of the Si nanotip helps the PEDOT: PSS penetrate better to the bottom of the nanostructure. Such modified nanotextures are expected to be applied on organic/Si hybrid solar cells. Therefore, Si nanotips are

expected to replace traditional Si nanowires in the antireflection structure of high-efficiency PEDOT:PSS/Si hybrid solar cells.

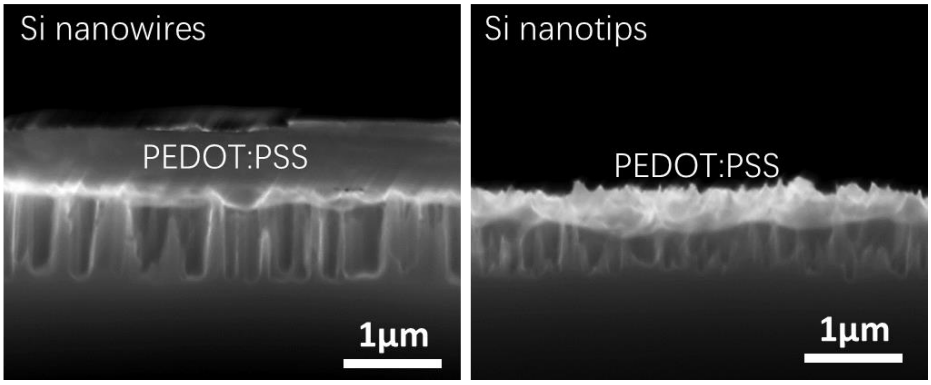

Figure 5.14. Cross-sectional SEM images of PEDOT:PSS/SiNWs interface and PEDOT:PSS/Si nanotips interface.

5.3.3 Mechanism

5.3.3.1 Impact of H_2O_2 concentration

The figure 5.15 showed the cross-section SEM images of Si nanowires etched with different concentrations of H_2O_2 in etching solution under fixed Ag plating conditions (Ag 15mM, plating time 50s) and etching time for 40s. It can be seen that with the increase of the concentration of H_2O_2 in the etching solution, the structure outline of the top part of Si nanowires gradually becomes blurred, and there is due the photoluminescence (PL) from porous nanowires during the SEM observation.[16] This suggests that the concentration of H_2O_2 has an effect on the formation of surface morphology of Si nanowires. Figure 5.16 showed the reflectance of Si nanowire structures fabricated at different H_2O_2 concentrations at wavelengths between 300nm and 1200nm. It can be seen from the figure that with the fixed length, the difference in light reflectance also confirmed the change of the Si nanowire structure under different H_2O_2 concentrations. Microporous Si structure formed at the top part of the Si nanowires under the high concentration H_2O_2 etching condition. During the MACE process, when the portion of Si that is in contact with the Ag particles being dissolved to form a

downward hole, the radially developed porous Si around the walls of the holes formed during the Ag-assisted etching process.

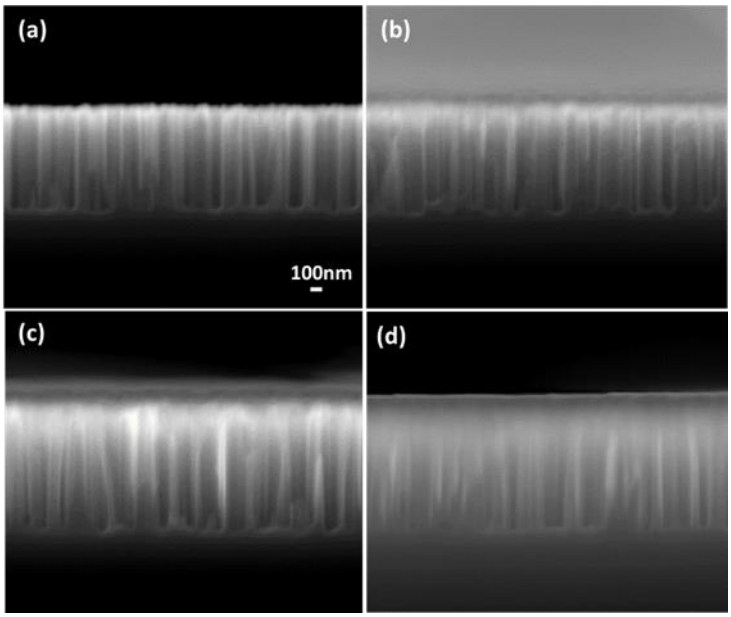

Figure 5.15. SEM images (cross-section) of Si nanowires fabricated at H_2O_2 concentrations of (a) 0.5M, (b) 0.7M, (c) 0.9M, (d) 1.1M.

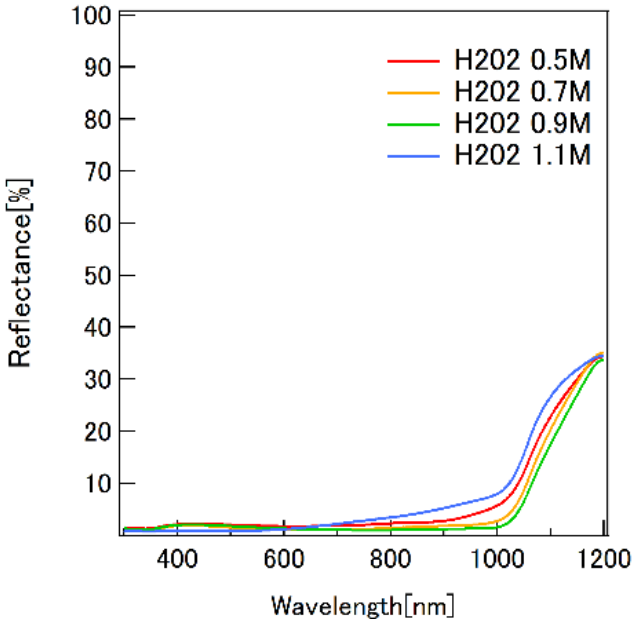

Figure 5.16. Reflectance of the Si nanowire in different lengths.

5.3.3.2 Formation of microporous Si

Porous Si has been frequently reported during formation of nanowires in peroxide systems.[17] The highly substituted n-type nanowires from Ag-assisted etching reported by Schadeet et al. [18] are porous. Recently, Hochbaumet et al. [19] also reported single-crystal mesoporous Si nanowires obtained from the degenerate MacEtch chip using $HN0_3$ and HF.

Ag-assisted etching of Si with HF and H_20_2 can be described as countless tiny electrochemical process. The reduction of H_20_2 at Ag particles is cathode reaction while the Si oxidation is the anodic reaction. Electrochemical etching of medium-doped Si below the critical current density J_{ps} is known to form microporous Si.[20] At the cathode sites, oxidant H_20_2 extract electrons from Si through Ag particles. The delivery of electrons from the Si valence band is equivalent to the injection of electronic holes h^+. These injected holes could spread away from the Ag/Si interface into the surrounding Si which is not in contact with the Ag particles and generate a spread current $J_h{}^+$, which is lower than J_{ps} , so that microporous Si formed around the Ag particles. Since the electronic holes density is the highest at the interfave between Ag and Si than the surroundings, the current density here is high enough to cause electro-polishing ($J_{Ag/Si}$> J_{ps}). Therefore, only the microporous Si where the Si is in direct contact with the Ag particles will be continuously etched, Ag particles sink into the Si substrate and leave a layer of microporous Si structure around the hole walls. When the concentration of H_2O_2 increases, there are more injected holes move from the hole tops to the pore boundaries and generate the spread current $J_h{}^+$ continuously, which will further generate the microporous layer that has been formed around the hole walls, thereby forming a conical microporous layer with a diameter range that increases from bottom to top of the hole. Similar results have been reported by Winston Chern el. that porous nanowire structures form because of hole (h^+) diffusion beyond the metal-semiconductor interface.[21] The essential change is the amount of carriers (h^+) injected.

The figure 5.17 (a) shows the formation of Si nanotips during Ag-assisted etching at

high H_2O_2 concentrations. Along with the contact part of Si with Ag particles being dissolved and the Ag particles sink into the Si bulk, a cone-shaped microporous layer is formed around the hole walls, and the range of microporous layer extends from bottom to top. During the etching process, because the microporous Si has a certain etching efficiency in the HF-H_20_2 solution [22], a part of the microporous Si at the top of the Si nanowire is etched, thereby forming Si nanowires with a crystalline core and a thin microporous outer layer with a decreasing diameter from bottom to top.[23] The figure 5.16 (a) and (b) showed the morphology changes during the polishing process of Si nanowires formed at low H_2O_2 concentration and high H_2O_2 concentration, respectively. Under the etching conditions of low H_2O_2 concentration, the thickness of the microporous Si structure in the outer layer of the Si nanowires is very thin. After the polishing treatment of HNO_3 and HF, there is undetectable morphology changment of the Si nanowires, showing a vertical columnar shape, which is SiNW. While under the high H_2O_2 concentration etching conditions, the microporous structures formed around the outer surface of Si nanowires are thick. Microporous structures are more easily to be oxidized into SiO_2 by HNO_3 than crystalline Si, and then oxidized and dissolved by HF to form a Si nanotips structure with a gradually decreasing diameter from bottom to top.

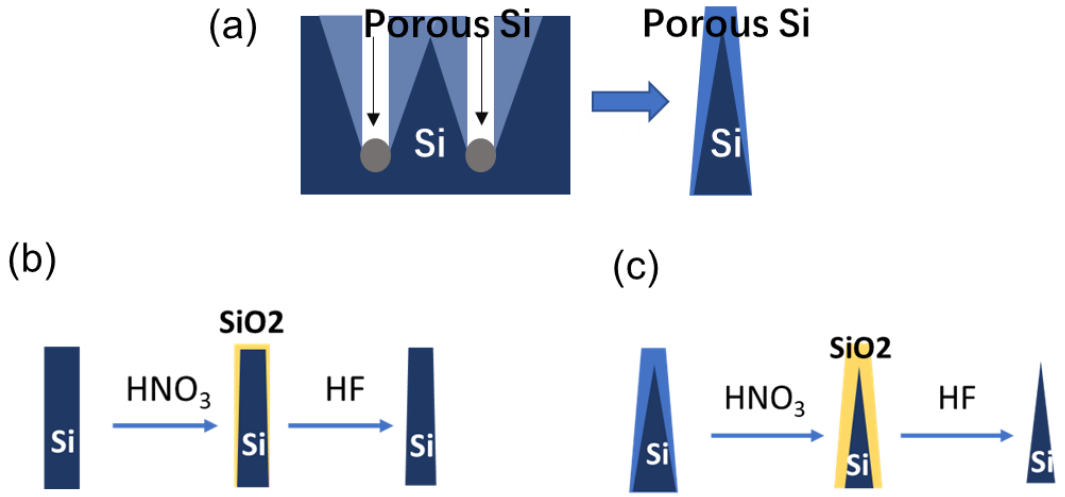

Figure 5.17. (a) Schematic diagram of microoporous Si formation during Ag-assisted etching at high H_2O_2 concentration; (b) Schematic diagram of polishing treatment process of Si nanowire formed at low H_2O_2 concentration; (c) Schematic diagram of polishing treatment process of Si nanowire formed at high H_2O_2 concentration.

5.4 Conclusion and Prospect

As a prior study, the main parameters in Ag plating step and etching step of MACE method during fabricating process of Si nanowires were figured out. For Ag plating step, the concentration of Ag^+ in the solution and the deposition time jointly affect the size and distribution of Ag nanoparticles formed on the Si surface. With the increase of Ag^+ concentration or the deposition time, Ag nanoparticles form on Si surface randomly and then grow or combine into larger size. When the diameter of the Ag particles increased to a certain size (The maximum diameter of ~230nm), it changed from lateral growth to radial growth, and finally developed into Ag dendrites. For etching step, the diameter of the Si nanowire is inversely proportional to the size of the Ag particles on the Si surface, and the length is proportional to the etching time. Si nanowires with different length of 0.5μm, 1μm, 5μm, 10μm and different diameters from 90nm to 200nm were successfully fabricated. Optical performance test showed that Si nanowire with a diameter of 100nm and a length of 0.5μm showed the best light absorptance property.

Si nanotips with adjustable length and distribution were successfully fabricated by combining the formation of microporous Si structures at high H_20_2 concentrations and the specific etching of porous Si structures by HNO_3/HF. The formation of microporous Si structure accompanied with the Si nanowire under the etching conditions of high H_2O_2 concentration was observed and the mechanism was discussed based on the principle of electrochemistry. Si nanotips improved the conformal film-forming properties of PEDOT:PSS and exhibit better light absorption than conventional Si nanowires, which is expected to be applied to hybrid heterojunction solar cells and further improve the performance with low fabrication cost.

This study is helpful for a more systematic and in-depth understanding of the effects of different variables on the morphology of nanostructures in the MACE method. It lays the foundation for further editing the different morphologies of nanowires and the application of Ag-assisted solution methods in other nanostructures.

References

[1] He J, Gao PQ, Yang ZH, Yu J, Yu W, Zhang Y et al (2017) Advanced materials 29:7.

[2] Ouyang J, Chu C W, Chen F C, et al. High-conductivity poly (3, 4-ethylenedioxythiophene): poly (styrene sulfonate) film and its application in polymer optoelectronic devices[J]. Advanced Functional Materials, 2005, 15(2): 203-208.

[3] Khang D Y. Recent progress in Si-PEDOT: PSS inorganic–organic hybrid solar cells[J]. Journal of Physics D: Applied Physics, 2019, 52(50): 503002.

[4] Naffeti M, Postigo P A, Chtourou R, et al. Elucidating the effect of etching time key-parameter toward optically and electrically-active silicon nanowires[J]. Nanomaterials, 2020, 10(3): 404.

[5] Raj V, Vora K, Fu L, et al. High-Efficiency Solar Cells from Extremely Low Minority Carrier Lifetime Substrates Using Radial Junction Nanowire Architecture, ACS Nano, 2019 13 (10) 12015-12023[J].

[6] Um H D, Choi D, Choi A, et al. Embedded metal electrode for organic–inorganic hybrid nanowire solar cells[J]. ACS nano, 2017, 11(6): 6218-6224.

[7] Bai F, Li M, Huang R, et al. A one-step template-free approach to achieve tapered silicon nanowire arrays with controllable filling ratios for solar cell applications[J]. RSC Advances, 2014, 4(4): 1794-1798.

[8] Moiz S A, Alahmadi A N M, Aljohani A J. Design of silicon nanowire array for PEDOT: PSS-silicon nanowire-based hybrid solar cell[J]. Energies, 2020, 13(15): 3797.

[9] Huang C Y, Wang D Y, Wang C H, et al. Efficient light harvesting by photon downconversion and light trapping in hybrid ZnS nanoparticles/Si nanotips solar cells[J]. Acs Nano, 2010, 4(10): 5849-5854.

[10] Subramani T, Syu H J, Liu C T, et al. Low-pressure-assisted coating method to improve interface between PEDOT: PSS and silicon nanotips for high-efficiency organic/inorganic hybrid solar cells via solution process[J]. ACS applied materials & interfaces, 2016, 8(3): 2406-2415.

[11] Van Hoang Nguyen S K, Gotoh K, Kurokawa Y, et al. Evidence of solute PEDOT: PSS as an efficient passivation material for fabrication of hybrid c-Si solar cells[J]. Sustainable Energy & Fuels, 2019, 3(6): 1448-1454.

[12] [12] Smith Z R, Smith R L, Collins S D. Mechanism of nanowire formation in metal assisted chemical etching[J]. Electrochimica Acta, 2013, 92: 139-147.

[13] Solar Cell Using Hourglass-Shaped Silicon Nanowires for Increased Light-Trapping Path.

[14] Zhang Q, Uchaker E, Candelaria S L, et al. Nanomaterials for energy conversion and storage[J]. Chemical Society Reviews, 2013, 42(7): 3127-3171.

[15] Li Y, Li M, Fu P, et al. A comparison of light-harvesting performance of silicon nanocones and nanowires for radial-junction solar cells[J]. Scientific reports, 2015, 5(1): 11532.

[16] Bai F, Li M, Song D, et al. One-step synthesis of lightly doped porous silicon nanowires in HF/$AgNO_3$/ H_2O_2 solution at room temperature[J]. Journal of Solid State Chemistry, 2012, 196: 596-600.

[17] Balasundaram K, Sadhu J S, Shin J C, et al. Porosity control in metal-assisted chemical etching of degenerately doped silicon nanowires[J]. Nanotechnology, 2012, 23(30): 305304.

[18] Schade M, Geyer N, Fuhrmann B, et al. High-resolution analytical electron microscopy of catalytically etched silicon nanowires[J]. Applied Physics A, 2009, 95: 325-327.

[19] Hochbaum A I, Gargas D, Hwang Y J, et al. Single crystalline mesoporous silicon nanowires[J]. Nano letters, 2009, 9(10): 3550-3554.

[20] Smith Z R, Smith R L, Collins S D. Mechanism of nanowire formation in metal assisted chemical etching[J]. Electrochimica Acta, 2013, 92: 139-147.

[21] Chern W, Hsu K, Chun I S, et al. Nonlithographic patterning and metal-assisted chemical etching for manufacturing of tunable light-emitting silicon nanowire arrays[J]. Nano letters, 2010, 10(5): 1582-1588.

[22] Chartier C, Bastide S, Lévy-Clément C. Metal-assisted chemical etching of silicon in HF–H_2O_2 [J]. Electrochimica Acta, 2008, 53(17): 5509-5516.

[23] Geyer N, Fuhrmann B, Huang Z, et al. Model for the mass transport during metal-assisted chemical etching with contiguous metal films as catalysts[J]. The journal of physical chemistry C, 2012, 116(24): 13446-13451.

6 Conclusion

This study aimed to fabricate light confinement structures in nano scale on the surface of c- Si by Ag-assisted all-solution process, and the etching mechanism is discussed in depth so as to realize the controlment the size, distribution, and surface morphology of the Si nanotextures. In this paper, an original Ag-assisted anisotropic alkaline etching method was developed, and Si nano-pyramid textures with an average size varying between 390nm and 950nm was successfully fabricated; A method based on MACE etching and fabricated was developed and Si nanotips texture with adjustable height, diameter and distribution was successfully fabricated. The two nanostructures have been applied to monocrystalline Si solar cells with different structures, and have shown good anti-reflection effects and interface properties for passivation and conformal layer formation. Compared with traditional micron-scale Si light-trapping structures, the efficiency of solar cells have been efficiently improved by utilizing Si nanotextures.

In chapter 1, the basic background of this study is briefly introduced, including: decarbonized society and solar energy, crystalline Si solar cells with thin substrates, anti-reflection design in Si solar cells, conventional Si texture fabrication method and Si nanostructures and application in crystalline Si solar cells. On this basis, the purpose of this study is to develop a low-cost and high-efficiency method for fabricating Si nanotextures, and to explore the practical application of Si nanotextures in monocrystalline Si solar cells.

In chapter 2, the main preparation instruments used in the fabrication of c-Si Si heterojunction cells, perovskite/Si tandem cells and organic/Si hybrid solar cells in this study, as well as the measurement methods used to evaluate the morphology of Si nanotextures and cell performance are introduced, including: Radio frequency (RF) magnetron sputtering, Plasma-Enhanced Chemical Vapor Deposition (PECVD), vacuum evaporation, spin-coating methods for solar cell fabrication and Scanning Electron Microscope (SEM), Energy-Dispersive X-ray spectroscopy (EDX), Spectrophotometer

Transmission electron microscopy (TEM), Current-voltage (J-V) measurement, External Quantum Efficiency (EQE) for evaluation.

In chapter 3, a simple one-step chemical etching methodology using Ag-containing alkaline solution for controlling the size of Si pyramids is proposed. The effect of different conditions during the etching process on the formation of Si pyramids was investigated in detail. Nanopyramid textures with an average size of ~500 nm have been successfully formed on the Si surface with a narrow size distribution. SHJ solar cells with Si nanopyramids fabricated by this method showed higher cell performance than those with the conventional micropyramids, exhibiting an enhanced J_{SC} and conversion efficiency. The nanopyramids obtained by our method feature regularly shaped tetrahedral structures with a narrow size distribution, which results in an enhanced light in-coupling and light trapping capabilities compared with Si micropyramids fabricated by the conventional alkaline etching. The etching margin of Si nanopyramids is also reduced by half. The mechanism of the etching process can be explained by the equilibrium reaction of $AgNO_3$ and KOH in the solution. Under proper conditions, Ag NPs are continuously generated on the Si surface during the etching process, acting as efficient etching masks as well as promoting the detachment of fine H2 bubbles from the Si surface. As a result, dense nucleation sites and uniform chemical reaction over the Si surface are realized, and nanoscale Si pyramid textures with a narrow size distribution can be formed with a minimal etching margin. These features of Si nanopyramids are promising for applications such as thin Si solar cells, advanced screen-printed metallization and perovskite/Si tandem solar cells.

In chapter 4, the effect of size variation of Si nanopyramid textures of the bottom cell on the overall perovskite/Si tandem cell performance is explored. Double-sided Si nanopyramid textures with an average size of 400-900 nm and an improved size distribution were fabricated using an original Ag-assisted alkaline etching method and applied in the bottom cell of perovskite/Si tandem cells. As the size of the Si pyramid increases, the light absorption of the bottom cell gradually increases, while excessive pyramid size (>600 nm) causes severe shunting and thickness inhomogeneity in the perovskite absorber layer, resulting in the degradation in the performance of tandem

cells, particularly in the V_{OC}. We find that the optimum Si texture size is around 400-500 nm, by which the perovskite top cell can be processed entirely by the conventional spin-coating method without creating an electrical shunting path in the top cell. Compared to the front-planar rear-textured reference Si bottom cell, the double-sided textured Si bottom cell with an average size of 530 nm provides a J_{SC} improvement by ~1.0 mA cm-2 and a higher PCE as a result of the increased spectral response in the Si bottom cell due to the suppressed interfacial reflection between the top and bottom cells. The results obtained in this study show the great potential for cost-effective tandem cell manufacturing using the solution-based top cell process without needing the costly multilayer optical coating at the top/bottom interface.

In chapter 5, the main parameters in Ag plating step and etching step of MACE method during fabricating process of Si nanowires were figured out. The concentration of Ag+ in the solution mainly determines the density of Ag particles formed on the Si surface, and the Ag plating time controls the Ag article size. For etching, the diameter of the Si nanowire is inversely proportional to the size of the Ag particles on the Si surface, and the length is proportional to the etching time. Si nanowires with different length of 0.5μm, 1μm, 5μm, 10μm and different diameters from 90nm to 200nm were successfully fabricated. Optical performance test showed that Si nanowire with a diameter of 100nm and a length of 0.5μm showed the best light absorptance property. Si nanotips with adjustable length/distribution and conical shape were successfully fabricated. The formation of microporous Si structure accompanied with the Si nanowire under the etching conditions of high H_2O_2 concentration was observed and the mechanism was discussed based on the principle of electrochemistry. Si nanotips improved the conformal film-forming properties of PEDOT:PSS and exhibit better light absorption than conventional Si nanowires, which is expected to be applied to hybrid heterojunction solar cells and further improve the performance with low fabrication cost.

In summary, the Si nanostructures fabricated in this research are expected to be applied to high-efficiency monocrystalline Si-based solar cells to achieve low-cost and high-efficiency industrial production. In addition, this study is helpful for a more systematic and in-depth understanding of the effects of different variables on the

morphology of nanostructures in the Ag-assisted solution etching method, on the basis of which more ideal Si nanostructures are expected to be developed.

Appendix

Si surface decoration of DNA-modified Au/Ag nanoparticles

1 Background

1.1 localized surface plasmon resonance (LSPR)

Localized Surface Plasmon Resonance (LSPR) emerges from the confinement of a light wave within conductive nanoparticles (NPs) that are smaller than the wavelength of light. This optical phenomenon results from the interaction between incident light and surface electrons in a conduction band, shown in Figure A1.1.[1] Coherent localized plasmon oscillations with a resonant frequency are generated through this interaction, and the resonant frequency strongly relies on the composition, size, geometry, dielectric environment, and particle-particle separation distance of NPs.[2] Commonly used materials for NP production include noble metals like Ag and Au. Due to the energy levels associated with d-d transitions, these metals exhibit LSPR in the visible spectrum.[3] Due to this phenomenon, metal nanoparticles are often used in various sensors to enhance the signal response.Hot spots refer to extremely localized areas with intense field enhancement, thought to result from local surface plasmon resonances. The technique that capitalizes on these hot spots to amplify Raman scattering is known as Surface-Enhanced Raman Spectroscopy (SERS). This optical technology is widely recognized for its role as a foundation in the advancement of highly sensitive biosensing.NPs undergoing LSPR show high molar extinction coefficients for absorption because of the “hot pot” enhancement (Figure A1.2) [4] and larger rayleigh scattering.[5] Therefore, metal nanoparticles can also play a role in enhancing light absorption.

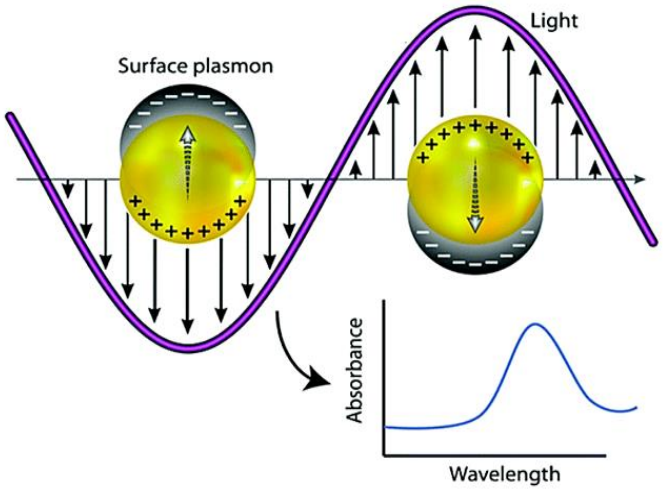

Fig. A1.1. localized surface plasmon resonance of metal nanoparticles.

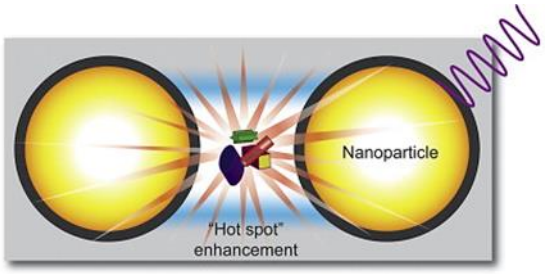

Fig. A1.2. SERS generates an enhanced Raman signal for molecules adsorbed to the surface of NPs or in the vicinity of “hot-spots “.

1.2 LSPR applied on PV devices

LSPR produces a strong resonance absorbance peak in the visible range of light, with its position being highly sensitive to the local refractive index surrounding the particle.

There are a large number of free electrons on the metal surface. When light is irradiated on the metal surface, the electrons undergo collective resonance under the action of light waves, which is called surface plasmon resonance (SPR). When this phenomenon occurs on the surface of nano-sized metal structures, it is also called local surface plasmon resonance. If the frequency of the incident photon matches the overall vibration frequency of the Noble metal nanoparticles or metal conduction electrons, the

nanoparticle c will have a strong absorption effect on the photon energy, and a strong resonant absorption peak will appear on the spectrum.

Thus LSPR can also be applied on PV devices to enhance the light absorption by scattering the incident light (Figure A1.3). Researches have improved that external quantum efficiency and photocurrent enhancement can be realized by introduce metal NPS on surface of Si PV devices. It is known that the scattering from a subwavelength metallic particle placed at a Si−air interface is preferentially directed toward the high dielectric material (Si).[6] This interesting optical phenomenon has been explored to enhance the photocurrent conversion efficiency of Si PV devices by using Ag, Au, or Cu nanoparticles (NPs), large photocurrent enhancement (as large as ~20-fold) has been reported in the literature around the LSPR for Si PVs modified with Cu, Ag, and Au NPs.[7] Besides, EQE(λ) enhancement of solar cells was strongly dependent on the forward scattering efficiency, and these coincided with the LSPR.[8]

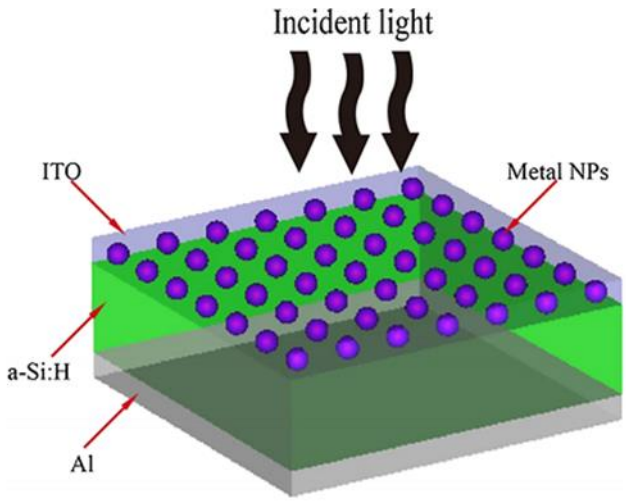

Fig. A1.3. Schematic illustration of Au nanoparticles utilized in thin-film solar cells to enhance light absorption. [9]

1.3 DNA-modified Au nanoparticles

The DNA molecule is generally viewed as a long polymer chain formed by two single strands in the shape of twisted ladder structure. Each rung of the ladder,

called a base pair, is following a special pairing rule, (i.e. adenine (A) with thymine (T) and cytosine (C) with guanine (G), which can be seen in Figure A1.4. These remarkable abilities in molecular recognition and structural configurations allow for DNA to self-assemble into a variety of geometries. DNA can self-assemble into a variety of geometries ranging from simple 2-D smiley faces to many exotic 3-D shapes. DNA-based scaffolding has emerged a powerful nanofabrication tool, directed self-assembly and metallization of DNA for its potential applications in nanoelectronic architecture and photonics.

An important applications is DNA nanostructure templates being used to assemble other inorganic components and functional groups. By adsorbing complementary DNA single strands on the surface of gold(Au) nanoparticles, we can Arrange the nanoparticles regularly, or form some patterns (Fig. A1.5).[10] Noble metal nanoparticles like silver (Ag) and Au support localized surface plasmons, where light can be resonantly absorbed or scattered depending on the metal nanoparticles' size, shape and the distances between them, and the surrounding environment. Using DNA to combine the two in an orderly manner is expected to enhance this effect, like Au-Ag core-shell (Au/Ag) structure and Core-satellite structure ,which have been reported to have strong LSPR. The presence of both Ag and Au NPs on the same PV device further enables the optimization of the LSPR conditions for enhanced photocurrent generation. Futher, Ag nanoparticles have also received more and more attention due to their higher scattering efficiency than Au.

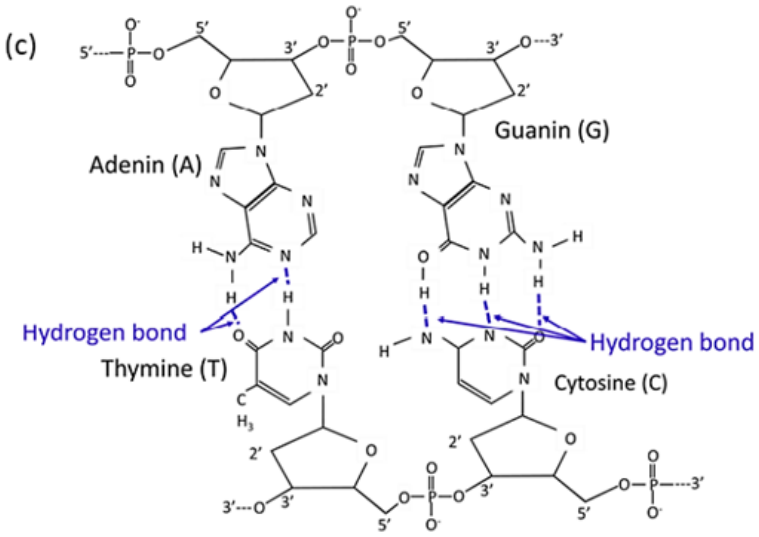

Fig. A1.4. DNA molecular structure diagram.

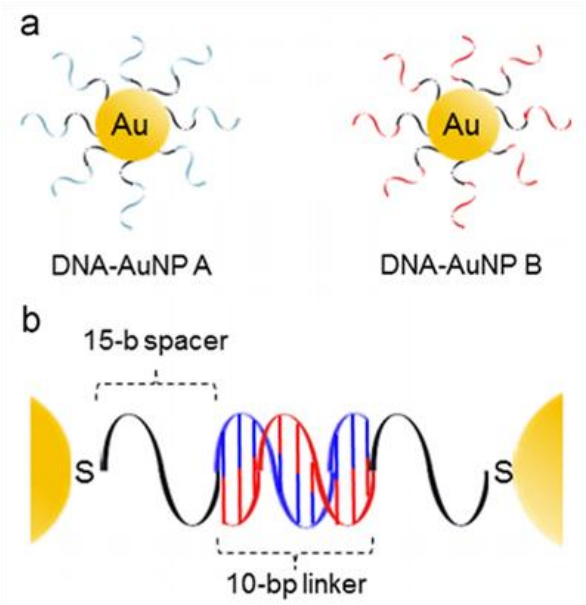

Fig. A1.5. Au nanoparticles are linked together through the self-assembly of two different DNA single strands.

1.4 Core–satellite structure assembled by ssDNA-embedded Au–Ag core–shell nanoparticles

As we know， Nanostructures can interact with incident light and Causes multiple optical effects. First is the light trapping effect. nanostructures exhibit an

excellent light absorption capability by light antireflective and scattering effects. Si nanowires and Si pyramid textures are widely used for Light confinement structures on the surface of c- Si solar cell. The second is light enhancement effect by metal nanoparticles. Localized surface plasmon resonance (LSPR) is an optical phenomena generated by a light wave trapped within conductive nanoparticles (NPs) smaller than the wavelength of light. NPs undergoing LSPR could have high molar extinction coefficients for absorption and larger rayleigh scattering. Common materials used for NP production are noble metals such as Ag and Au, NPs undergoing LSPR: High molar extinction coefficients for absorption. Larger Rayleigh scattering. Ag nanoparticles have higher scattering efficiency than Au.The presence of both Ag and Au NPs on the same PV device further enables the optimization of the LSPR conditions for enhanced photocurrent generation.[11] In recent years, a novel structure has attracted great interest, which is Au–Ag core–shell NPs on the Si surface to form a SERS-active core–satellite structure, seeing in Figure A1.6.[12] The presence of Ag enhances the SERS effect. This structure makes the distance between nanoparticles smaller. This structure can be used as a reliable SERS substrate, with high enhancement and high reproducibility.

Fig. A1.6. Core–satellite structure assembled by ssDNA-embedded Au–Ag core–shell NPs.

1.5 Purpose

In this study, we aim to use single-strand(ss)DNA as a tool to decorate Au-Ag core shell nanoparticles on the Si surface and control their arrangement at the two-dimensional and three-dimensional levels. In this way, Au/Ag nanoparticles with specific structural combinations can be modified on the surface of Si devices with different

surface morphologies, and further explore the impact of metal nanoparticles with different arrangements on the light absorption and cell efficiency of photovoltaic devices.

2. Experimental Details

2.1 Gold (Au) nanoparticles

Au nanoparticles with a diameter of 10 nm (E2726 7511) and 30nm was used. Au nanoparticles are dispersed in pure water with their surfaces not chemically modified. This solution was stored refrigerated at 4°C.

2.2 Single-strand DNA

The single-stranded DNA was synthesized and purchased from the Japan Gene Research Institute. Four types of DNA with different base sequences were used in the self-assembly of metal nanoparticles. Two types of ssDNA(~33nm) modified with thiol groups and different base sequences were used as single-stranded DNA to modify Au nanoparticles, which are link#1 AAAAAAAAAAATCCTTATCAATATT and link#2 AAAAAAAAAAAATATTGATAAGGAT. The Au nanoparticles modified with link#1 are called DNA-AuNP A, and the Au nanoparticles modified with link#2 are called DNA-AuNP B. DNA AuNP A and DNA AuNP B can be linked together through the base pairing rules of ssDNA.

2.3 Buffer

Borate buffer was used when synthesizing DNA-modified Au nanoparticles. Borate buffer is a buffer solution with a borate concentration of 50 mM and pH=8.5. In this document, this concentration of Borate buffer is referred to as 1 × Borate buffer. Phosphate buffer was used to fabricate the DNA-modified Au nanoparticle multiple structure. Phosphate buffer is a buffer solution with Na_2HPO_4 concentration of 46.5 mM, KH_2PO_4 concentration of 19.8 mM, and pH=7.2. Phosphate buffer at this concentration is expressed as 1 × Phosphate buffer.

2.4 Preparation procedure for DNA-modified Au nanoparticles

In this step, Au particles with a diameter of 30 nm and Au particles with a diameter of 10 nm are modified by two different single-stranded DNA link#1 and link#2 respectively, the operating instructions are shown in Figure A2.1.

(1) DNA is stored frozen in tubes. 500 μl of 1× Borate buffer was added to the tube containing DNA before utilization. The concentration of DNA was measured using a spectrophotometer (Model V 630BIO, manufactured by JASCO Corporation.

(2) Au nanoparticle solution and DNA solution were added to a 1.0 ml PCR tube in order by pipette, the ratio fllows (moles of Au nanoparticles): (moles of DNA) = 400, at which point the Au nanoparticles will be modify as much DNA as possible. Then add 20× Borate buffer with a pipette so that the final concentration in the tube is 1× Borate buffer. The mixed solution was rotated in a rotary stirrer (Labquake Tube Rotator #4002110, Thermo Scientific) for 20 minutes.

(3) 5 M NaCl was added in Au NPs/ssDNA solution to a final concentration of 0.05 M, perform ultrasonic shaking (BRANSONIC Ultrasonic Cleaner 1510J DTH, BR ANSON ULTRASONICS CORPORATION) for 10 seconds, fllowing rotation by the rotary stirrer or 15 minutes. Next, repeat this step and add NaCl in batches so that the NaCl concentration in the solution increases step by step according to 0.05 M, 0.1 M, 0.15 M, 0.2 M, 0.3 M, 0.4M, and 0.5 M. After each addition of NaCl, ultrasonic vibration was performed for 10 s and rotation was performed for 15 min. During this step, a thiol bond (coordination bond between Au and sulfur) between the Au nanoparticles and the single-stranded DNA was formed. In DNA-AuNPs, DNA acts as a steric hindrance to prevent aggregation, NaCl can neutralize the same electrical charge of DNA and Au nanoparticles, making it easier for them to combine. Negatively charged Au nanoparticles tend to aggregate when cations are added, herefore, the salt concentration was gradually increased to prevent agglomeration of Au nanoparticles.

(4) Centrifuge (centrifuge 5424, Eppendorf) at 9300 rpm for 100 minutes. After removing the supernatant, add 1 ml of 1× phosphate buffer and shake well. This

operation is performed four times. This removes excess unmodified DNA. The supernatant was stored in Falcon tubes (Eppendorf) until use.

(5) Use a spectrophotometer to measure the concentration of the prepared DNA-modified Au nanoparticles.

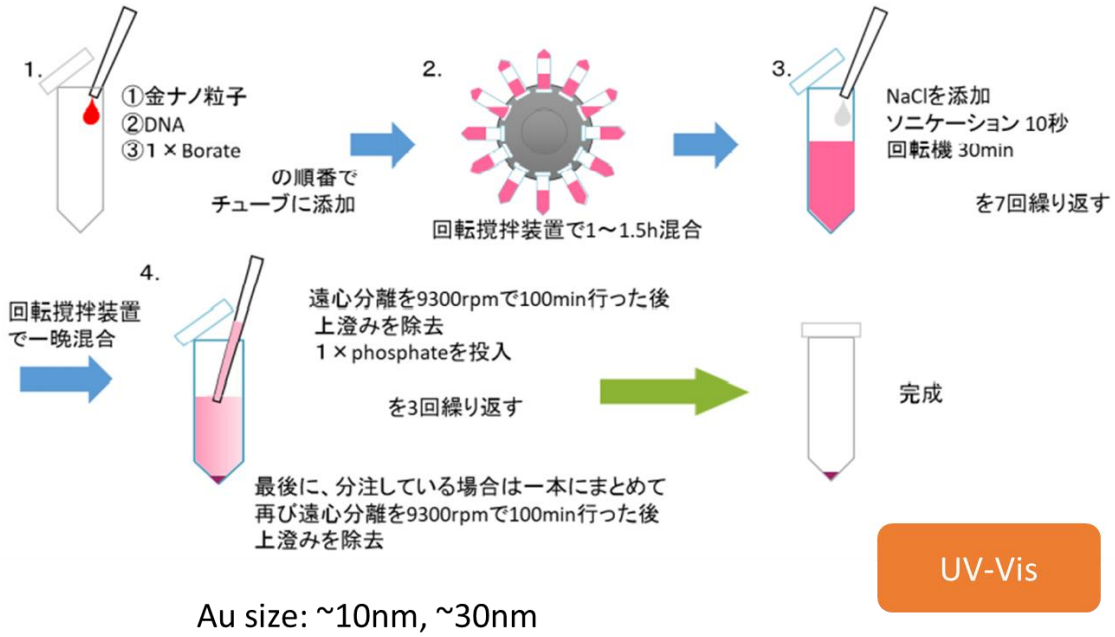

Au size: ~10nm, ~30nm

DNA: link#1 AAAAAAAAAAATCCTTATCAATATT(~33nm)

link#2 AAAAAAAAAAAATATTGATAAGGAT

Fig. A2.1. DNA AuNP preparation procedure.

2.5 Ag deposition on DNA-Au NPs

900ul of 30nm diameter Au-DNA solution with a concentration of 5nM was prepared in the PCR tube, then 100µl 1x phosphate buffer, 100µl NaCl solution with a concentration of 2.5 M, and 150µl Ascorbic acid solution with a concentration of 0.1 M were added into the tube in order. After thoroughly mixing, 150 µl of $AgNO_3$ solution with a concentration of 1.06 mM was added and shaking incubate at 45°C for 60 min under dark environment. During this process, silver nitrate($AgNO_3$) is reduced by ascorbic acid, and it can be observed that the solution changes from pink to orange, indicating that the surface of the Au nanoparticles is covered with Ag, and an Au/Ag

core-shell nanoparticle solution is prepared(Fig A2.2).

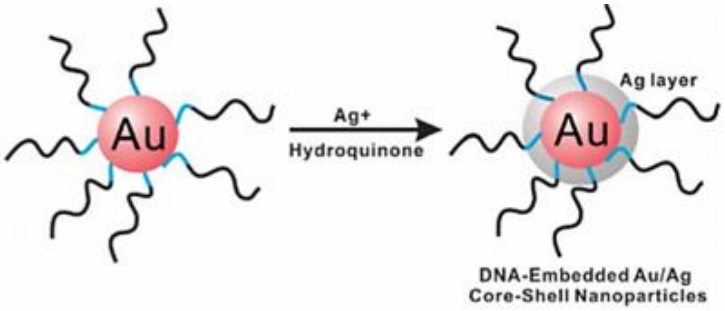

Fig. A2.2. Structure of DNA-embedded Au/Ag core-shell nanoparticles.

2.6 DNA-Ag-Au NPs Immobilization on Si surface

In this step, the 30nm-diameter Au-DNA, which is the core of the core-satellite structure, is fixed on the surface of the Si substrate. A layer of APTES was employed to functionalize the Si surface, facilitating the adsorption of negatively charged ssDNA-coated Au NPs via the positive amino group of APTES. Consequently, an Au–DNA NPs monolayer was affixed to the Si surface through this electrostatic interaction. In this investigation, we employed a technique to deposit Au nanoparticles onto a Si substrate through the electrostatic attraction between the Si surface and the Au-DNA nanoparticles. The phosphate group ($-PO_3^{2-}$) at the DNA terminus carries a negative charge, and the Si substrate surface is tailored with amino groups to impart a positive charge to the substrate surface ($-NH_3^+$) (Fig A2.3). The initial step involves using a 5% HF solution to eliminate the oxide film from the Si surface, followed by thorough rinsing with pure water and air-drying at room temperature. The Si surface modification was executed by immersing the Si substrate in a mixture of (3-aminopropyl) triethoxysilane (APTES), water, and ethanol (3:3:94) and exposing it to UV light with a wavelength of 302 nm for 1 hour at N_2 atmosphere. Subsequent to the modification, the Si slides were rinsed extensively with water and baked at 105°C for 30 minutes.

30nm Au-DNA solution, suf-Buffer, and NaCl solution were mixed together in

proportion, then the functionalized Si substrates are immersed in it , and then let it stand in the dark at room temperature for 12 hours. Subsequently, a monolayer of 30 nm Au NPs was established on the Si surface via the electrostatic interaction between Au and NH_2 groups. The Si wafer was rinsed three times with DI water to eliminate loosely attached NPs, followed by an incubation step in a phosphate buffer solution (10 mM, pH 7.45) and 2 mM sulfosuccinimidyl 4-(N-maleimidemethane) (Sulfo-SMCC) for 2 hours at 45°C. This process aimed to block excess NH_2 groups on the Si surface.

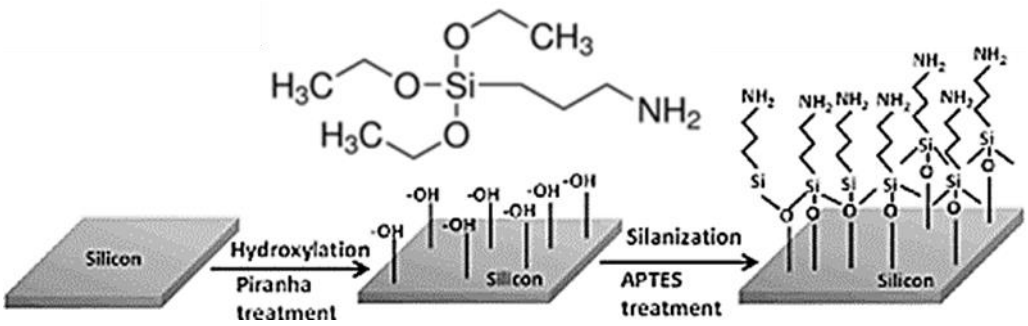

Fig. A2.3. Silanization treatment of Si surface.

2.7 Assembly of core-satellite structure by Au–Ag core–shell nanoparticles

This step assembles 10nm Au-DNA around 30nm Au-DNA to form a core-satellite structure, shown in Figure A2.4. Following the DI water rinse, the Si substrate was submerged in an EP tube filled with 2μl of 10nm Au-DNA nanoparticles. The EP tube was subsequently placed in a 65°C water bath for 5 minutes and allowed to remain at room temperature for 12h to facilitate DNA hybridization. Ultimately, the Si substrates underwent three rounds of rinsing with pure water and was air-dried at room temperature.

Fig. A2.4. Shcematic diagram of core-satellite structure by Au–Ag core–shell nanoparticles on Si surface.

3. Results

3.1 Au-Ag core-shell structure

By adjusting the concentration and proportion of each component in the Ag plating solution, uniform Ag shells were successfully deposited on the surfaces of Au nanoparticles of different sizes. SEM top view in Figure A3.1 shows Au nanoparticles of different sizes wrapped with Ag shells of varying thicknesses. Figure A3.2 shows the UV/Vis Spectrophotometers of the solution before and after Ag plating. From the spectral results, it can be seen in that after Ag plating, there is an obvious peak representing Ag, which suggests the formation of Ag shells outside the Au nanoparticles.[13] The EDS results also confirmed this in Figure A3.3.By controlling the concentration of $AgNO_3$ in the solution and the time of Ag plating, the thickness of the Ag shell can be controlled. After adding sodium chloride and phosphate buffer to the mixed solution and increasing the incubation temperature, an orange solution is obtained, which means better uniformity of Ag shell, which can be seen in Figure 3.4, what`s more, high temperature is conducive to the stretch of DNA molecular chain, preventing the aggregation of Au nanoparticles during the Ag plating process, thereby making the generated Ag shell more uniform.

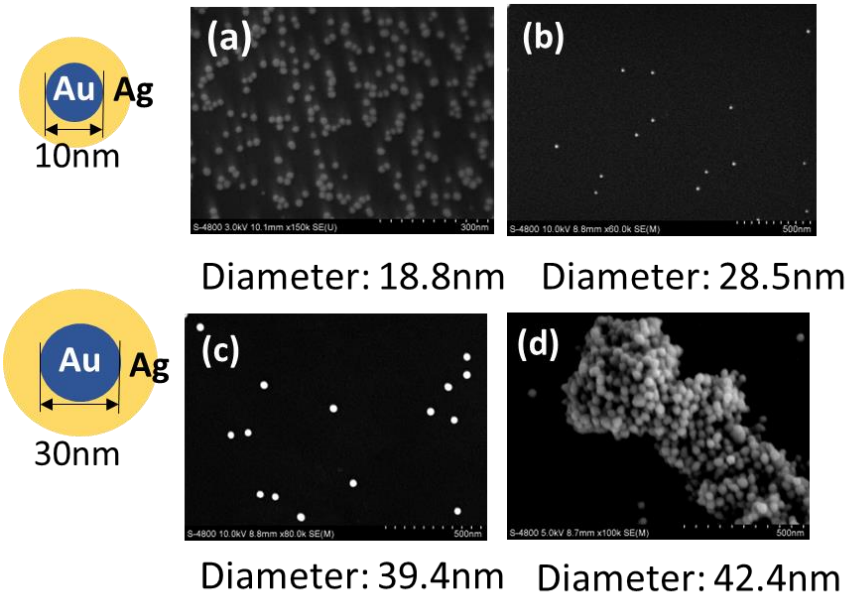

Fig. A3.1. SEM images of Au nanoparticles with a diameter of 10 nm are coated with Ag shells of two different thicknesses (a) and (b); Au nanoparticles with a diameter of 30 nm are coated with Ag shells of two different thicknesses (c) and (d).

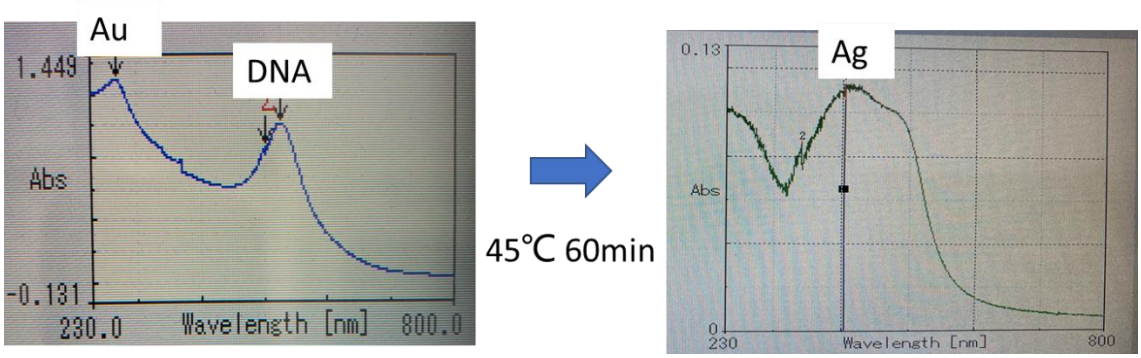

Fig. A3.2. UV/Vis Spectrophotometers of the Au NPs solution before and after Ag plating.

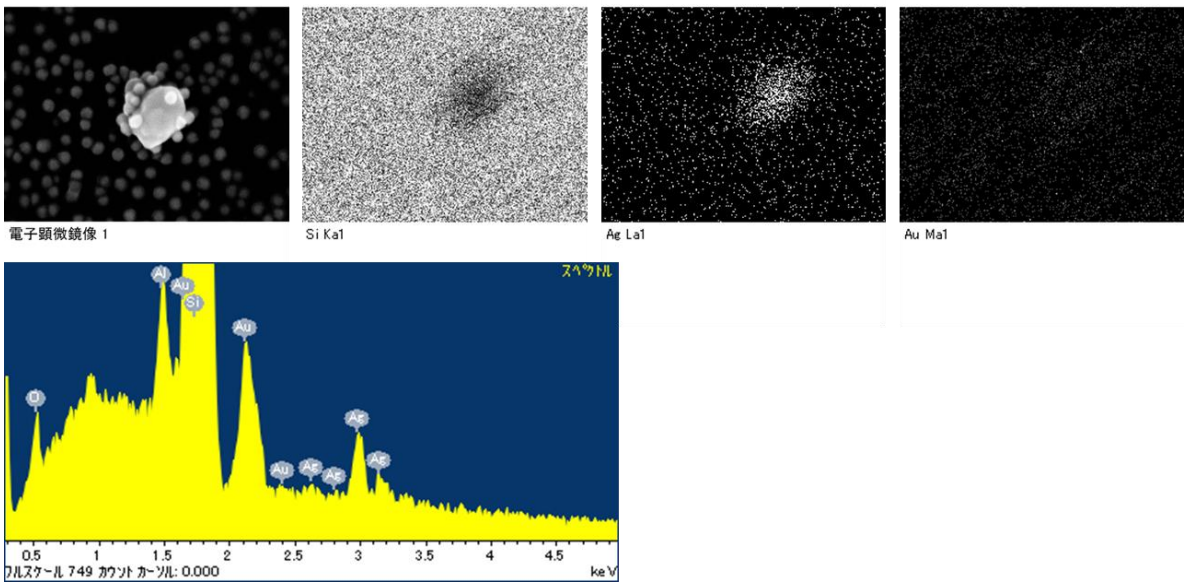

Fig. A3.3. EDS results of the Au-Ag core shell NPs on Si surface.

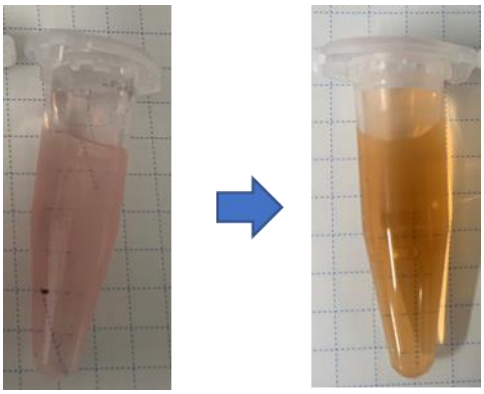

Fig. A3.4. Diagram phtots of Au NPs solution in Eppendorf tube before and after Ag plating process under 45℃ for 60min.

3.2 DNA-Ag-Au NPs Immobilization on bare Si

This set of SEM images in Figure A3.5 shows the immobilization results of Au-Ag nanoparticles on the Si surface treated with APTES under five differect concentration of NaCl and Au nanoparticles a, b, c, d, e and f. Detailed solution concentration ratios during DNA-Ag-Au NPs Immobilization on Si surfaceprocess are listed in the table A3.1.

The ordinate is the concentration of NaCl in the solution, and the abscissa is the concentration of Au-DNA nanoparticles in the solution. It can be seen that as the concentration of NaCl increases, the density of the Au nanoparticles fixed on the Si surface gradually increases due to the stretching of the DNA single strand modified on the surface of the Au nanoparticles. By increasing the concentration of NaCl and Au-Ag nanoparticles in the solution, the density distribution of nanoparticles attached to the surface of the Si substrate can be increased.

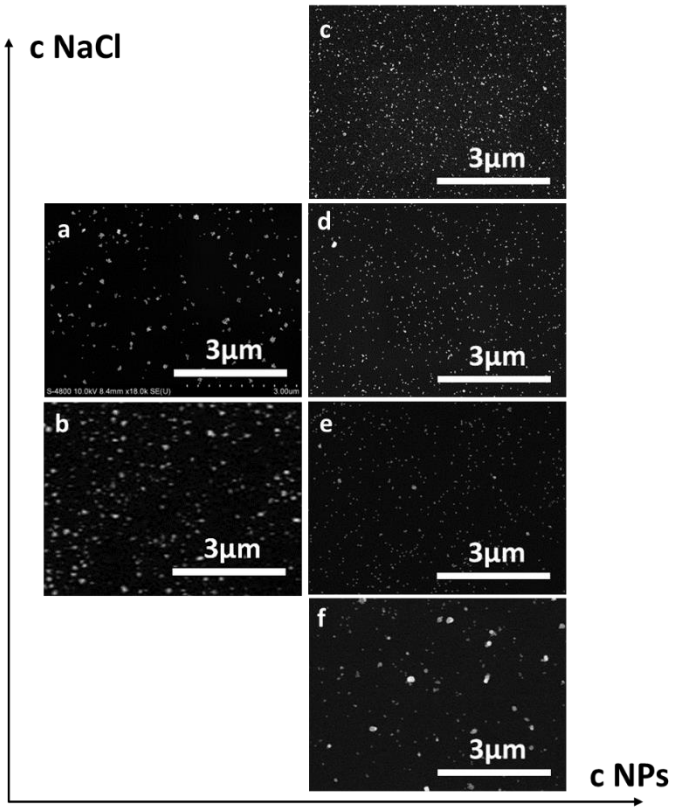

Fig. A3.5. SEM top view of Au nanoparticles modified on the Si surface under five differect concentration of NaCl and Au nanoparticles a, b, c, d, e and f. The abscissa is the concentration of NaCl and the ordinate is the concentration of Au nanoparticles.

Table A3.1. Five differect concentration ration of NaCl and Au nanoparticles a, b, c, d, e and f during DNA-Ag-Au NPs Immobilization on Si surface.

	Solution/µl	Total amount/µl
a	NPs: Buff: NaCl= 10: 142: 48	200
b	NPs: Buff: NaCl= 10: 158: 32	200
c	NPs: Buff: NaCl= 10: 42: 48	100
d	NPs: Buff: NaCl= 10: 58: 32	100
e	NPs: Buff: NaCl= 10: 74: 16	100
f	NPs: Buff: = 10: 90	100

3.3 Formation of Core–satellite structure

The figure A3.2 shows a top view of Au/Ag core-shell core-satellite structure fixed on the surface of a Si substrate. Through the combination of two complementary DNA single strands, the Au/Ag core-shell core-satellite structure was successfully realized on Si surface.

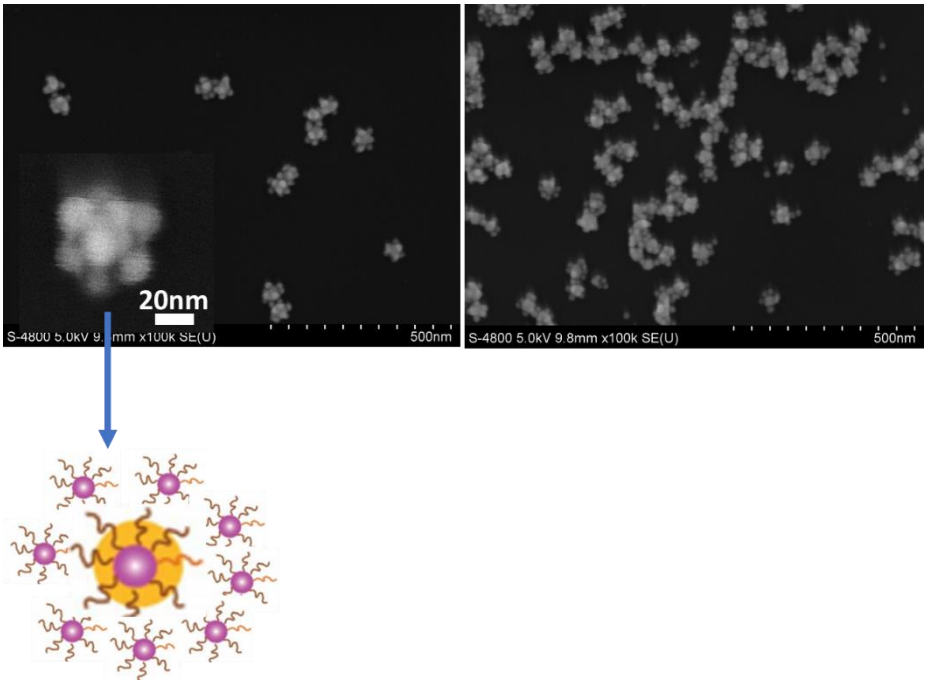

Fig. A3.6. Top view SEM images of Au-Ag core-shell core-satellite structure fixed on the surface of a Si substrate.

3.4 Optical effects of Au/Ag nanoparticles

In order to explore the impact of the LSPR phenomenon of nanoparticles on light scattering, Si nanowire and Si nanotip structures were fabricated according to the methods described in Chapters 5 of the text respectively. Si nanowires and nanotips are treated by APTES and the decorated with Au-Ag core-shell nanoparticles. It can be seen from SEM images in Figure A3.7 (a) and (c) that nanoparticles are adsorbed on the bottom flat surface of the Si nanostructure as well as on the sidewalls, but the number is much smaller than that of a flat Si surface. However, The light absorption of the Si nanowire structure and the Si nanotip structure were enhanced with the modification of Ag/Au NPs compared with bare Si nanotips and Si nanowires in the full wavelength range from 300nm to 1200nm (Fig. A3.7 (b)(d)).[14]

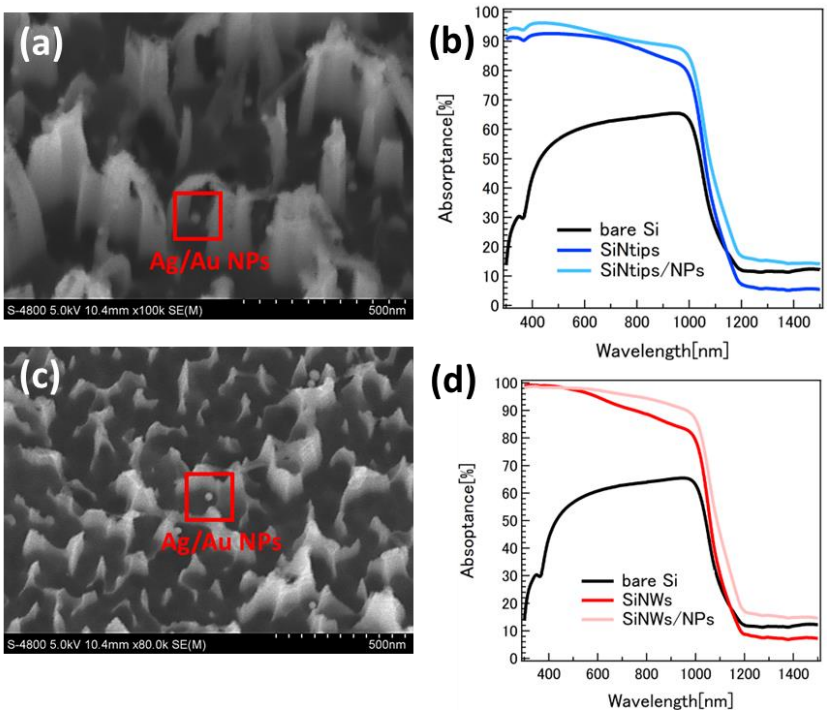

Fig. A3.7. (a) 30° -tilt SEM image of Si nanowires decorated with Au-Ag core-shell nanoparticles; (b) Lighit absorbtance of Si nanowires decorated with Au-Ag core-shell nanoparticles; (c) 30° -tilt SEM image of Si nanotips decorated with Au-Ag core-shell nanoparticles; (b) Lighit absorbtance of Si nanotips decorated with Au-Ag core-shell nanoparticles.

3.5 Raman signal enhancement effect of Au/Ag nanoparticles

As shown in Figure A3.8 (a), in order to test the raman signal enhancement effect of the Au-Ag core-shell nanoparticles, 100nm titanium dioxide(TiO_2) film is deposited on the Si substrate and annealed for the crystallization. Then the substrate was treated with APTES and modified with Au nanoparticles of 10nm and 30nm with Ag shell. From the raman intensity diagram in Figure A3.8 (b), it can be seen that raman signals of NPs-modified TiO_2 are significantly enhanced (TiO_2 in anatase and rutile phases for 153nm and 638nm repectivily) [15], which is because LSPR produces a strong resonance absorbance peak in the visible range of light, with its position being highly sensitive to the local refractive index surrounding the particle. This result proved that the existence

of Ag shell can effectively enhance the LSPR effect of Au nanoparticles, and LSPR effect caused by Au/Ag nanoparticles can also effect the layer under NPs.

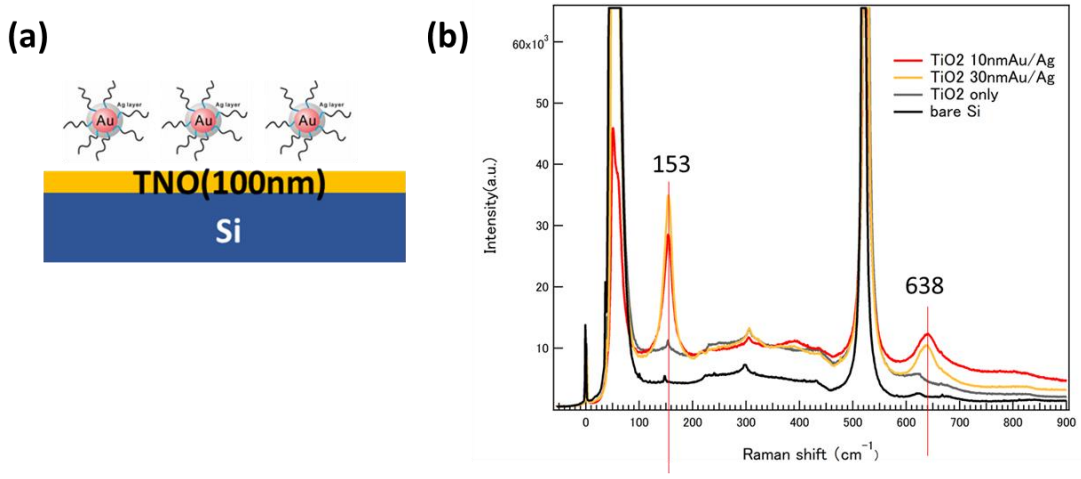

Fig. A3.8. (a) Shematic diagram of structure of Raman signal test sample; (b) Raman signal intensity diagram of TiO_2 surface-modified Au/Ag nanoparticles with Au particle diameters of 10nm and 30nm, and TiO_2 without metal particle modification.

3.6 Application in perovskite solar cell

In order to verify the impact of LSPR effect on the photovaltic devices, Au nanoparticles were used to decorate the bottom of the ETL layer of n-i-p perovskite solar cell. The cell structure is as shown in the figure A3.9.

The J-V curve of the cell was measured and the cell parameters are extracted from the J-V curve and listed in table A3.2. The specific experimental steps of cell fabricating are as follows:

Glass/ITO substrate of 1.5cm x1.5cm was cleaned by surfactant, H_2O, Acetone, IPA, Ethanol/N_2 in order, followed by the surface silanization by APTES. Then 1onm diameter-DNA-Au NPs are decorated on the surface of TiO_2 layer, SnO_2 layer(HTL), perovskite layer, PTAA(HTL) layer are then fabricated by spincoating method in order. At last, Au electrodes were fabricated by evaporation. It can be seen from the table that the efficiency of the perovskite cell modified with Au NPs increased from 12.94% to 13.48%,

indicating that Au nanoparticles have a positive effect on improving cell efficiency through the enhanced raman reflection effect and SERS effect.

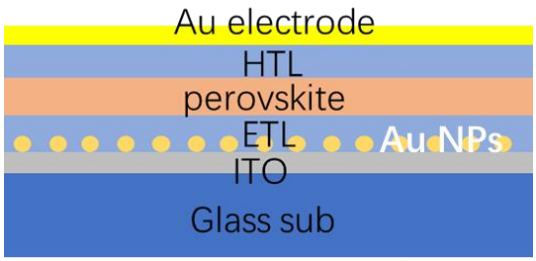

Fig. A3.9. Stucture schematic diagram of Au NPs decorated n-i-p perovskite solar cell.

Table A3.2. Cell parameters of Au NPs decorated n-i-p perovskite solar cell.

		J_{sc} (mA/cm^2)	V_{oc} (V)	FF	R_{sheet} (Ω·cm^2)	PCE (%)
With Au NPs	Max	20.45	0.99	0.63	1.19E+03	13.48
	Ave	20.69	0.97	0.57	0.55E+03	11.96
Without Au NPs	Max	21.30	1.0	0.61	1.06E+03	12.94
	Ave	20.69	0.98	0.58	0.56E+03	11.84

4. conclusion

In this study, Au-Ag core shell nanoparticles were successfully formed by depositing Ag shells on the surface of Au nanoparticles, and three-dimensional nanoparticles' structure of Au-Ag core- shell core-satellite structure are fabricated by self-assemblement of single-stranded DNA, and were decorated on the surface of flat Si/ TiO_2 and three-dimensional structures such as Si pyramids and nanowires.

The results of reflectivity and raman measurement showed that the Au-Ag nanoparticles

modified on the Si surface have the effect of improving the light absorption of the bottom device and can improve the raman signal response of the bottom device due to the enhanced SERS effect and light scattering. Furthermore, by decorating the bottom of n-i-p perovskite cell with Au nanoparticles, the efficiency of the perovskite cell was increased by 0.54%.

The self-assembly method of DNA-modified Au / Ag nanoparticles on Si surfaces is accurate, versatile, and reproducible. This approach creatively combines the fields of biology and materials, which can fix metal nanoparticles with controllable arrangements on surfaces of flat Si as well as Si nanostructures, and is expected to be applied to Si/ perovskite photovoltaic devices to further improve the efficiency.

References

[1] T.R. Jensen, M.D. Malinsky, C.L. Haynes, R.P. Vn DuyneJ. Phys. Chem. B, 104 (2000), p. 10549

[2] Chen R, Zhang W, Guan X, et al. Rear electrode materials for perovskite solar cells[J]. Advanced Functional Materials, 2022, 32(26): 2200651.

[3] J. Jeong, M. Kim, J. Seo, H. Lu, P. Ahlawat, A. Mishra, Y. Yang, M. A. Hope, F. T. Eickemeyer, M. Kim, Nature 2021, 592, 381.

[4] Liu J, Wang Z, Chen C, et al. Increasing hotspots density for high-sensitivity SERS detection by assembling array of Ag nanocubes[J]. Talanta, 2023, 258: 124408.

[5] J. Yguerabide, E.E. Yguerabide Anal. Biochem., 262 (1998), p. 137

[6] Ho W J, Feng S K, Liu J J, et al. Improving photovoltaic performance of silicon solar cells using a combination of plasmonic and luminescent downshifting effects[J]. Applied Surface Science, 2018, 439: 868-875.

[7] H. A. Atwater and A. Polman, “Plasmonics for improved photovoltaic devices,” Nat. Mater. 9(3), 205–213 (2010).

[8] Wang P H, Millard M, Brolo A G. Optimizing plasmonic silicon photovoltaics with Ag and Au nanoparticle mixtures[J]. The Journal of Physical Chemistry C, 2014, 118(11): 5889-5895.

[9] Akimov Y A, Koh W S, Ostrikov K. Enhancement of optical absorption in thin-film solar cells through the excitation of higher-order nanoparticle plasmon modes[J]. Optics express, 2009, 17(12): 10195-10205.

[10] Bujold K E, Lacroix A, Sleiman H F. DNA nanostructures at the interface with biology[J]. Chem, 2018, 4(3): 495-521.

[11] J.-H. Lee, J.-M. Nam, K.-S. Jeon, D.-K. Lim, H. Kim, S. Kwon, H. Lee and Y. D. Suh, ACS Nano, 2012, 6, 9574–9584.

[12] Zhang Z, Zhang S, Lin M. DNA-embedded Au–Ag core–shell nanoparticles assembled on silicon slides as a reliable SERS substrate[J]. Analyst, 2014, 139(9): 2207-2213.

[13] Lim D K, Kim I J, Nam J M. DNA-embedded Au/Ag core–shell nanoparticles[J]. Chemical communications, 2008 (42): 5312-5314.

[14] Mulazimoglu E, Nogay G, Turan R, et al. Enhanced localized surface plasmon resonance obtained in two step etched silicon nanowires decorated with silver nanoparticles[J]. Applied Physics Letters, 2013, 103(14).

[15] Scrimieri L, Velardi L, Serra A, et al. Enhanced adsorption capacity of porous titanium dioxide nanoparticles synthetized in alkaline sol[J]. Applied Physics A, 2020, 126: 1-8.

Acknowledgments

First of all, I would like to express my gratitude to my supervisor, Professor Usami Noritaka, for providing me with financial and spiritual support for my research throughout my doctoral period, for being tolerant of my many shortcomings and mistakes, and for always guiding me in key areas at the crucial moments. Secondly, I would like to thank Associate Professor Kurokawa for always answering and helping me when I had questions. Thanks to Professor Tagawa Miho for being willing to accept my immature ideas during my first year of Ph.D. and providing me with opportunities to engage in biologically related research that interests me. Finally, I would like to thank Professor Matsui and Professor Sai from the National Institute of Advanced Industrial Science and Technology in Tsukuba. Without their careful guidance, I would not have been able to publish the two papers during my doctoral period. I benefited a lot during the exchange experience in AIST.

I would like to express my gratitude to all the classmates, colleagues and staff who helped me during my time at the Nagoya University and AIST, including but not limited to all the senior students and junior students in the Usami lab, My junior classmate Haitao Wang and Fukaya Shohei, the secretary Meiyan Lai and Yoshiko Iseki, and Zhihao Xv from AIST. You have given me a lot of help and support in my daily study and life.

I would like to thank the DII program and the research program for the financial support, as well as the short-term and long-term exchange opportunities provided by the DII program, which are of great help in advancing my doctoral research.

Thanks to my friends both in Japan and China who have been by my side for the past four years. Every contact you had with me has saved me from anxiety and frustrated, given me the courage to continue, and brought so much happiness to my life. I won't name names, but if you read this, the person I'm talking about is you my friend.

Thanks so much to my family, especially my mom, you are everything to me. Thousands of words make me speechless.

Thanks to my little golden hamster Pipi, you brought so much comfort and happiness to me in the first and second year of my Ph.D. when I was unable to return to China during the epidemic.

Finally, I would like to thank myself. These four years have not been easy. In addition to academic difficulties, I experienced the left of loved ones and I hope they could be proud of me now. I experienced severe anxiety and self-doubt, and there are too many shortcomings that made me unsuitable for being a PhD, but I believed that success belongs to the persevering. Now I can finally draw an end to these four years with this doctoral thesis and give myself an account. I'm proud of myself for getting back up every time I fall and finding happiness again. The PhD career was a very magical experience which changed me a lot. This is a wonderful ending, but also a new starting point, and I'm ready to embark on a new journey now.

Lists of pubulications

Journal Paper

1. **Yuqing Li**, Hitoshi Sai, Takuya Matsui, Zhihao Xu, Van Hoang Nguyen, Yasuyoshi Kurokawa and Noritaka Usami,

“Nanopyramid texture formation by one-step Ag-assisted solution process for high-efficiency monocrystalline Si solar cells”, Solar RRL, (2022)6(11), 2200707,

2. **Yuqing Li**, Hitoshi Sai, Calum McDonald, Zhihao Xu, Yasuyoshi Kurokawa, Noritaka Usami, and Takuya Matsui

“Nanoscale size control of Si pyramid texture for perovskite/Si tandem solar cells enabling solution-based perovskite top-cell fabrication and improved Si bottom-cell response”, Advanced Materials Interfaces, 2023: 2300504.

Conference

1. NU-MUS conference

[Poster] PEDOT: PSS/Crystalline Si Hybrid Solar Cells Employing Tapered Nanostructures, ***Yuqing Li**, Nguyen Van Hoang and Usami Noritaka

2. The 67th JSAP spring meeting

[Oral] Fabrication of Si Textures with Low Etching Margin Using $AgNO_3$-assisted Alkaline Solution, ***Yuqing Li**, Nguyen Van Hoang and Usami Noritaka

3. PVSEC-30-GPVC2020

[Poster] Fabrication of si textures with low etching margin using Ag-assisted alkaline solution, ***Yuqing Li**, Van Hoang Nguyen and Noritaka Usami

4. The 69th JSAP spring meeting

[Oral] Silicon nanopyramid texture fabricated by one-step solution process and its application to silicon heterojunction solar cells ***Yuqing Li**, Hitoshi Sai, Takuya Matsui and Noritaka Usami ,0ral, 2022.3

5. PVSEC-33 (The 33rd International Photovoltaic Science and Engineering Conference)

[Oral] A novel one-step solution method to fabricate silicon nanopyramid texture and its application to crystalline silicon heterojunction solar cells *__Yuqing Li__, Hitoshi Sai, Takuya Matsui, Noritaka Usami, oral,2022,11

6. TandemPV Workshop 2023

[Poster] Impact of Silicon Pyramid Texture Size on Perovskite/Silicon Tandem Solar Cell Performance

* __Yuqing Li__, Hitoshi Sai, Calum McDonald, Noritaka Usami, Takuya Matsui, 2023,6

7. The 84th JSAP spring meeting

[Oral] Improved bottom cell current in perovskite/silicon tandem solar cells by double-sided nanopyramid Si texture, *__Yuqing Li__, Hitoshi Sai, Calum McDonald, Zhihao Xu, Yasuyoshi Kurokawa, Noritaka Usami, Takuya Matsui, 2023,9